

WL-TR-95-4088



**ROTATING BEAM FATIGUE TESTING
AND HYBRID CERAMIC BEARINGS**

Y. H. PAO

**THE TORRINGTON COMPANY
P.O. BOX 1008
TORRINGTON CT 06790-1008**

JULY 1994

FINAL REPORT 03/01/92--03/01/94

Approved for public release; distribution unlimited

19960701 096

**MATERIALS DIRECTORATE
WRIGHT LABORATORY
AIR FORCE MATERIEL COMMAND
WRIGHT-PATTERSON AIR FORCE BASE, OH 45433-7734**

DTIC QUALITY INSPECTED 1

SUPPLEMENTARY

INFORMATION

ERRATA

AD-A310912

WL-TR-95-4088



**ROTATING BEAM FATIGUE TESTING
AND HYBRID CERAMIC BEARINGS**

DR. Y. P. CHIU

**THE TORRINGTON COMPANY
P.O. BOX 1008
TORRINGTON CT 06790-1008**

JULY 1994

FINAL REPORT 03/01/92-03/01/94

Approved for public release; distribution unlimited

**MATERIALS DIRECTORATE
WRIGHT LABORATORY
AIR FORCE MATERIEL COMMAND
WRIGHT-PATTERSON AIR FORCE BASE, OH 45433-7734**

ERRATA

AD-A310912



DEPARTMENT OF THE AIR FORCE

WRIGHT LABORATORY (AFMC)
WRIGHT-PATTERSON AIR FORCE BASE, OHIO

AD-A310911

30 SEP 96

MEMORANDUM FOR REPORT RECIPIENT

FROM: WL/MLBT
2941 P Street Suite 1
Wright-Patterson AFB OH 45433-7750

SUBJECT: Report Correction, WL-TR-95-4088, "Rotating Beam Fatigue
Testing and Hybrid Ceramic Bearings", The Torrington Company

1. The author for the subject report was Dr. Y. P. Chiu, as shown on the attached title page. Please correct your copy of the report on the title page and report documentation page.
2. Any questions can be directed to the undersigned at (937)-255-2465.

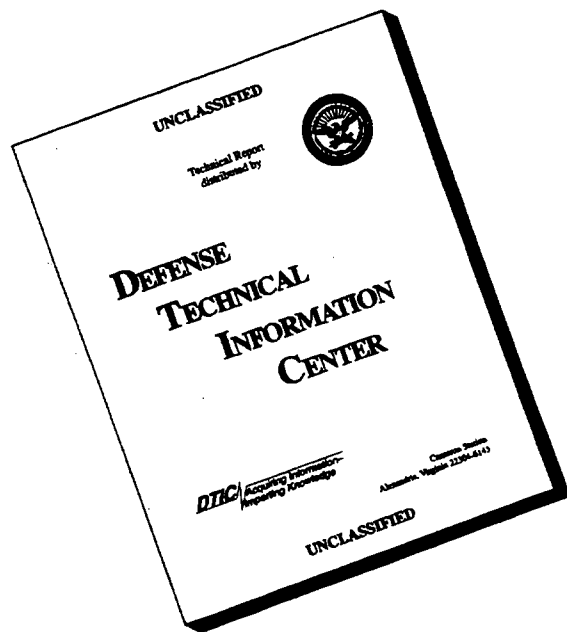
Karl R. Mecklenburg

KARL R. MECKLENBURG
Nonstructural Materials Branch
Nonmetallic Materials Division
Materials Directorate

AD-A310911

ERRATA

DISCLAIMER NOTICE



**THIS DOCUMENT IS BEST
QUALITY AVAILABLE. THE
COPY FURNISHED TO DTIC
CONTAINED A SIGNIFICANT
NUMBER OF PAGES WHICH DO
NOT REPRODUCE LEGIBLY.**

NOTICE

When government drawings, specifications, or other data are used for any purpose other than in connection with a definitely related government procurement operation, the United States Government thereby incurs no responsibility nor any obligation whatsoever; and the fact that the government may have formulated, furnished, or in any way supplied the said drawings, specifications, or other data, is not to be regarded by implication or otherwise as in any manner licensing the holder or any other person or corporation, or conveying any rights or permission to manufacture, use, or sell any patented invention that may in any way be related thereto.

This report is releasable to the National Technical Information Service (NTIS). At NTIS, it will be available to the general public, including foreign nations.

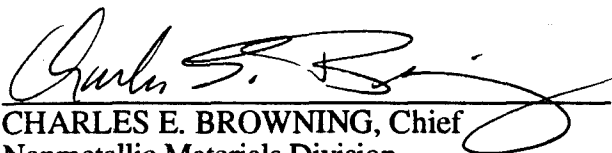
This technical report has been reviewed and is approved for publication.



KARL R. MECKLENBURG, Project Engineer
Nonstructural Materials Branch
Nonmetallic Materials Division



KENT J. EISENTRAUT, Chief
Nonstructural Materials Branch
Nonmetallic Materials Division



CHARLES E. BROWNING, Chief
Nonmetallic Materials Division
Materials Directorate

If your address has changed, if you wish to be removed from our mailing list, or if the addressee is no longer employed by your organization, please notify WL/MLBT, Bldg 654, 2941 P Street, Suite 1, Wright-Patterson AFB OH 45433-7750 to help maintain a current mailing list.

Copies of this report should not be returned unless return is required by security considerations, contractual obligations, or notice on a specific document.

REPORT DOCUMENTATION PAGE			Form Approved OMB No. 0704-0188	
Public reporting burden for this collection of information is estimated to average 1 hour per response, including the time for reviewing instructions, searching existing data sources, gathering and maintaining the data needed, and completing and reviewing the collection of information. Send comments regarding this burden estimate or any other aspect of this collection of information, including suggestions for reducing this burden, to Washington Headquarters Services, Directorate for Information Operations and Reports, 1215 Jefferson Davis Highway, Suite 1204, Arlington, VA 22202-4302, and to the Office of Management and Budget, Paperwork Reduction Project (0704-0188), Washington, DC 20503.				
1. AGENCY USE ONLY (Leave blank)	2. REPORT DATE JUL 1994	3. REPORT TYPE AND DATES COVERED FINAL 03/01/92--03/01/94		
4. TITLE AND SUBTITLE ROTATING BEAM FATIGUE TESTING AND HYBRID CERAMIC BEARINGS		5. FUNDING NUMBERS C F33615-92-C-5910 PE 62712 PR 8355 TA 00 WU 06		
6. AUTHOR: DR Y.H.PAO				
7. PERFORMING ORGANIZATION NAME(S) AND ADDRESS(ES) THE TORRINGTON COMPANY P.O. BOX 1008 TORRINGTON CT 06790-1008		8. PERFORMING ORGANIZATION REPORT NUMBER		
9. SPONSORING/MONITORING AGENCY NAME(S) AND ADDRESS(ES) MATERIALS DIRECTORATE WRIGHT LABORATORY AIR FORCE MATERIEL COMMAND WRIGHT PATTERSON AFB OH 45433-7734		10. SPONSORING/MONITORING AGENCY REPORT NUMBER WL-TR-95-4088		
11. SUPPLEMENTARY NOTES				
12a. DISTRIBUTION / AVAILABILITY STATEMENT APPROVED FOR PUBLIC RELEASE; DISTRIBUTION IS UNLIMITED.		12b. DISTRIBUTION CODE		
13. ABSTRACT (Maximum 200 words) Silicon nitride is the material of choice for ceramic rolling bearings. The issue of low operational reliability in certain rolling contact applications in DoD systems may be related to its limited room temperature bending strength as compared with modern bearing steels. To explore the cyclic fatigue strength of silicon nitride, rotating beam fatigue tests have been performed for two types of high quality bearing-grade HPSN. A total of 122 rotating beam specimens have been tested, mostly in the maximum stress range 600 - 850 MPA. Statistical method has been applied to the test data to obtain the fatigue exponent, Weibull slope and crack growth parameter for the two baseline materials. Theory of ceramic reliability has been applied to predict the failure probability of ceramic rod (in RCF test) and ceramic balls (in thrust loaded hybrid ball bearings) in terms of fatigue cycles and friction coefficient. Forty-eight (48) hybrid ceramic 6206 size ball bearings have been endurance tested using sudden-death method and ceramic balls of the same materials used in the rotating beam tests.				
14. SUBJECT TERMS Silicon nitride ceramics Rotating beam fatigue test Rolling contact stress		Weibull statistics Sliding Friction Reliability prediction		15. NUMBER OF PAGES 153
16. PRICE CODE				
17. SECURITY CLASSIFICATION OF REPORT UNCLASSIFIED	18. SECURITY CLASSIFICATION OF THIS PAGE UNCLASSIFIED	19. SECURITY CLASSIFICATION OF ABSTRACT UNCLASSIFIED	20. LIMITATION OF ABSTRACT SAR	

TABLE OF CONTENTS

SECTION	PAGE
LIST OF FIGURES	vii
LIST OF TABLES	xii
ABBREVIATION, ACRONYMS, AND SYMBOLS	xiv
SUMMARY	1
FOREWORD	5
1.0 INTRODUCTION AND BACKGROUND	6
1.1 Objectives and Approaches	6
1.2 Background of the Problems	8
1.3 Material Selection and Properties	10
2.0 ROTATING BEAM FATIGUE EXPERIMENT	13
2.1 Rotating Beam Specimen Fabrication	13
2.2 Rotating Beam Fatigue (RBF) Testing	16
2.2.1 Test Rig and Preliminary Tests	16
2.2.2 Test Completion Modes	18
2.3 Test Results	19
2.3.1 Stepwise Load Test	24
2.4 RBF Specimen Failure Analysis	24
2.4.1 Fractography of TSN-03H Specimens	24
2.4.2 Fractography of NBD-200 Specimens	33

2.4.3	Further Fractography Study at University of Florida	36
2.5	Assessment of Specimen Surface Finish	36
2.6	Comparison of RBF Test Results of HPSN, Steels and Sintered Si_3N_4	40
3.0	DATA ANALYSIS AND RELIABILITY THEORY	44
3.1	Weibull Plots for Lives at Constant Load	44
3.2	Median Life Calculation	44
3.3	Maximum Likelihood Analysis for Multiple Stepwise Load Test	49
3.3.1	Weibull Distribution Plots of Equivalent Life	49
3.4	Effect of Surface Finish on the Fatigue Performance of the RBF Specimens	51
3.5	Reliability Formulation with Volume Flaw Assumption	55
3.5.1	Fast Fracture	55
3.5.2	Cyclic Fatigue	57
3.6	Rolling Element under Contact Load of Multiple Stress Levels	58
3.6.1	Theory of Subcritical Crack Growth under Multiple Loadings	58
4.0	HYBRID BALL BEARING TESTING AND ANALYSIS	61
4.1	Hybrid Bearing Test Preparation	61
4.2	Analysis of Test Bearing	61
4.3	Endurance Test of Hybrid Ball Bearings	64
4.4	Hybrid Ball Bearing Failure Analysis	65
4.4.1	Norton/Cerbec Balls	65

4.4.2	Toshiba Balls	71
4.4.3	Bearing Rings	76
4.5	Maximum Likelihood Estimate of L_{10} Life for the Hybrid Bearings	80
4.6	Theory	81
4.7	Result of ML Calculations	81
5.0	TENSILE STRESS IN HERTZIAN BEARING CONTACTS	86
5.1	Tensile Stress on the Perimeter of a Hertzian Contact	86
5.2	The Subsurface Principal Tensile Stress Field in Hertzian Elliptical Contact	89
5.3	Tensile Stress Distribution in Frictional Hertzian Contact	89
6.0	FAILURE PROBABILITY PREDICTION FOR ROLLING CONTACTS	95
6.1	Assumptions	95
6.1.1	The Relationship Between Ball Rotational Cycles and Bearing Revolutions	96
6.2	Example 1 - Ceramic Rod in RCF Tester	98
6.2.1	Maximum Tensile Stress and Effective Volume in RCF Contacts	104
6.3	Example 2 - Angular Contact Hybrid Ball Bearings	104
6.3.1	Hybrid Ball Bearing with Non-track Forming Ball	109
6.5	Discussion of Results	111
7.0	CONCLUSIONS	113
8.0	RECOMMENDATIONS	115

9.0	REFERENCES	117
APPENDIX A	Tabulation of Rotating Beam Test Data	121
APPENDIX B	Maximum Likelihood Analysis for Multiple Load Test	133
APPENDIX C	Effective Stress Volume of RBF Specimens	136
APPENDIX D	Fafnir Bearing Test Laboratory: Hybrid Bearing Test Report	139
APPENDIX E	The Equivalent Bearing Cycles and Bearing Revolution for the Non-track Forming Case	152

LIST OF FIGURES

NUMBER		PAGE
FIG.1	Flow Chart for Approach for Bearing Life Prediction Based on Material Flaw Failure Model	7
FIG.2	Weibull Plots of Failure Stress Based on MOR Data	12
FIG.3	Design Drawing of the Rotating Beam Specimen	14
FIG.4a	Photograph of Rotating Beam Specimen, Rod Blank and Fractured Specimen	15
FIG.4b	Photograph of 70 Finished Rotating Beam Specimens	15
FIG.5	Relation Between Maximum Bending Stress and Bending Moment in the RBF Tester	17
FIG.6	Histogram of the Rotating Beam Fatigue Tests With Three Completion Modes: Fatigue, Runout and Fast Fracture	20
FIG.7	Stress-life Plots of Rotating Beam Fatigue Testing	23
FIG.8	Fractograph of Rotating Beam Specimen No.A37 (50x,150x)	25
FIG.9	Fractograph of Rotating Beam Specimen No.A37 (1000x,5000x)	26
FIG.10	Fractograph of Rotating Beam Specimen No.A37 (10000x,15000x)	27
FIG.11	EDX Result of Specimen A37	29
FIG.12	Fractography of Rotating Beam Specimen A43 (20x,1000x)	30
FIG.13	Fractography of Rotating Beam Specimen A43 (3000x)	31
FIG.14	EDX Result of Rotating Beam Specimen A43	32
FIG.15	Fractography of Rotating Beam Specimen B14 (45x)	34
FIG.16	EDX Result of Rotating Beam Specimen B14	35

LIST OF FIGURES (Cont'd)

NUMBER		PAGE
FIG.17	Fractography of Rotating Beam Specimen B3 (35x)	37
FIG.18	Fractography of Rotating Beam Specimen B4 (830x)	37
FIG.19	EDX Result of Rotating Beam Specimen B4	38
FIG.20	S-N Plots for Rotating Beam Tests of Two P/M Steels	42
FIG.21	RBF Test Results for HPSN and S-N Curves for Sintered Si_3N_4 and Two Hardened P/M Steels	43
FIG.22	Weibull Plot for Fatigue Life at Maximum Stress 850 MPa With TSN-03H Rotating Beam Specimens	45
FIG.23	Weibull Plot for Fatigue Life at Maximum Stress 800 MPa With TSN-03H Rotating Beam Specimens	45
FIG.24	Weibull Plot for Fatigue Life at Maximum Stress 750 MPa With TSN-03H Rotating Beam Specimens	46
FIG.25	Weibull Plot for Fatigue Life at Maximum Stress 850 MPa With NBD-200 Rotating Beam Specimens	46
FIG.26	Weibull Plot for Fatigue Life at Maximum Stress 800 MPa With NBD-200 Rotating Beam Specimens	47
FIG.27	Variation of Median Life with Failure Stress	48
FIG.28	Weibull Plots of Equivalent Cycles for NBD-200 and TSN-03H Rotating Beam Specimens	50
FIG.29	Weibull Plot of Equivalent Cycles for NBD-200 Rotating Beam Specimen With 'Very Smooth Surface'	52
FIG.30	Weibull Plot of Equivalent Cycles for NBD-200 Rotating Beam Specimen With 'Smooth' Surface	52
FIG.31	Weibull Plot of Equivalent Cycles for NBD-200 Rotating Beam Specimen With 'Marginal' Finish	53
FIG.32	Components of Hybrid Test Ball Bearing	62

LIST OF FIGURES (Cont'd)

NUMBER		PAGE
FIG.33	Photomicrograph of Spall on Failed NBD-200 Ball (Bearing No. 535-92)	67
FIG.34	Photomicrograph of Spalls on Failed NBD-200 Ball (Bearing No.535-92)	67
FIG.35	SEM Photograph of Large Spall on a Failed NBD-200 Ball	68
FIG.36	EDX Spectrum on the Large Spalls on a NBD-200 Ball (Bearing No.535-92)	69
FIG.37a	SEM Photograph of a Small Spall (45x) (Bearing No.535-92)	70
FIG.37b	SEM Photograph of a Small Spall (330x) Around a Mg Rich Feature (Bearing No.535-92)	70
FIG.38	EDX Spectrum of the Mg Rich Feature ('3')	72
FIG.39	EDX Spectrum of the Mg Rich Feature ('4')	73
FIG.40	Photomicrograph of Spalled TSN-03H Ball (80x) (Bearing No.259-93)	74
FIG.41	Photomicrograph of Spalled TSN-03H Ball (Bearing No.266-93)	74
FIG.42	Photomicrograph of Spalled TSN-03H Ball (Bearing No.274-93)	75
FIG.43	Photomicrograph of Spalled TSN-03H Ball (Bearing No.276-93)	75
FIG.44	SEM Photograph of Spalled TSN-03H Ball (Bearing No.259-93)	76
FIG.45	EDX Result for Spalled TSN-03H Ball (Bearing No.259-93)	77

LIST OF FIGURES (Cont'd)

NUMBER		PAGE
FIG.46	SEM Photograph of Spalled TSN-03H Ball (Bearing No.266-93)	78
FIG.47	EDX Result of Spalled TSN-03H Ball, Mg Rich Area (Bearing No. 266-93)	78
FIG.48	EDX Result of Spalled TSN-03H Ball, Fe Rich Area (Bearing No. 266-93)	79
FIG.49	Maximum Likelihood Estimate of TSN-03H and NBD-200 Ball Failure Probability Based on Endurance Test Data	85
FIG.50	Variation of Ratio of Tensile Stress to Maximum Contact Pressure at End of Major and Minor Axes	87
FIG.51	Contours of Equal Principal Tensile Stress for $a/b=8.774$, $\nu=0.26$ and $\mu=0$	90
FIG.52	Contours of Equal Principal Tensile Stress for $a/b=1.765$, $\nu=0.26$ and $\mu=0$	90
FIG.53	Contours of Equal Principal Tensile Stress for $a/b=8.774$, $\nu=0.26$ and $\mu=0.05$	92
FIG.54	Contours of Equal Principal Tensile Stress for $a/b=8.774$, $\nu=0.26$ and $\mu=0.10$	92
FIG.55a	Federal Mogul RCF Test Configuration	99
FIG.55b	Rolling Tracks on Ball Bearing Balls	99
FIG.56	Failure Probability of RCF Rod of Two Ceramic Baseline Materials at $p_{max} = 6.0$ GPa	101
FIG.57	Failure Probability of RCF Rod of Two Ceramics With Different Poisson Ratios at $p_{max} = 6.0$ GPa	102
FIG.58	Variation of Failure Probability of TSN-03H RCF Rod With Poisson Ratio at $p_{max} = 6$ GPa	102

LIST OF FIGURES (Cont'd)

NUMBER		PAGE
FIG.59	Variation of Failure Probability of TSN-03H RCF Rod With Friction Coefficient at $p_{\max} = 6.0$ GPa	103
FIG.60	Variation of Maximum Tensile Stress in NBD-200 RCF Rod With Friction Coefficient, at $p_{\max} = 4.0$ GPa	103
FIG.61	Failure Probability of Track-Forming TSN-03H (28) Ball Set With Cycles and Friction Coefficient, $p_{\max} = 2.4$ GPa	108
FIG.62	Failure Probability of Track-Forming NBD-200 (28) Ball Set With Cycles and Friction Coefficients	108
FIG.63	Failure Probability of Non Track-Forming TSN-03H (28) Ball Set With Cycles and Friction Coefficient, at $p_{\max} = 2.4$ GPa	110
FIG.64	Failure Probability of Non Track-Forming NBD-200 (28) Ball Set With Cycles and Friction Coefficients	110
FIG.65	Weibull Plot of Failure Probability of Hybrid Bearings with TSN-03H Balls Tested in Four Groups	141
FIG.66	Hybrid Bearing Test Layout	148
FIG.67	Photographs of Standard Endurance Test Machines	149

LIST OF TABLES

NUMBER		PAGE
1	Material Property Data of the Two Baseline Si_3N_4	11
1.2	Material Impurity Specification.	11
2	Summary of RBF Test Data for TSN-03H	21
3	Summary of RBF Test Result for NBD-200	22
4	Distribution of Fast Fracture Specimen Number/Total Number as a Function of Material and Finish Type	39
5	Fatigue Property Data of the Two Test Materials Based on Rotating Beam Fatigue (RBF) Testing	51
6	Tabulation of Median Value of $\Sigma\sigma^mN$ and slope β , RBF Test Material NBD-200	54
7	Summary of Material Properties for the Two Test Materials	56
8	Input Data and Result of 206 Bearing Analysis	63
9	Summary of Hybrid Bearing Test Results	66
10	NBD-200 Ball Endurance Test Data and Failure Probability Calculation Using Maximum Likelihood	83
11	TSN-03H Ball Endurance Test Data and Failure Probability Calculation Using Maximum Likelihood	84
12	Contact Ellipse Axes	86
13	Calculation of Maximum Tensile Stresses for Hybrid Hertzian Contacts	88
14	Values of Tensile Stress/Maximum Hertzian Stress at the Edge of Sliding Contact	93
15	Input Constants for Reliability Prediction	97
16	Variation of Maximum Tensile Stress, Effective Volume in RCF Contact at Maximum Pressure 6.0 GPa	105

17	Comparison of Effective Volume in Various Tests	105
18	Test Conditions and Dimensions of a Pure Thrust Loaded Hybrid Ball Bearing	106
19	Test Lives of Hybrid Bearing With NBD-200 Balls	143
20	Test Lives of Hybrid Bearings With TSN-03H Balls	144
21	Dimensional Inspection Data of Hybrid Bearings With NBD-200 Balls	145
22	Dimensional Inspection Data of Hybrid Bearings With TSN-03H Balls	146

ABBREVIATIONS, ACRONYMS AND SYMBOLS

a	crack size, semi-major axis
b	semi-contact width, semi-minor axis
B	crack growth constant
D	ball radius
E	Young's modulus
FF	fast fracture mode
f	friction coefficient
HP	hot pressed
HPSN	hot pressed silicon nitride
G	shear modulus
K_I	mode I stress intensity factor
K_{Ic}	fracture toughness, Mode I
L	likelihood function
M	bending moment
m	Weibull modulus
m'	$= m/(n-2)$
N_f	life cycles
$N_{.50}$	median life (cycles)
n	fatigue exponent, stress-life exponent
P_f	failure probability
p_{max}	maximum contact pressure

ABBREVIATIONS, ACRONYMS AND SYMBOLS (Cont'd)

RCF	rolling contact fatigue
RBF	rotating beam fatigue
S	surface area
S_{eff}	effective stress area
V	stress volume
V_{eff}	effective stress volume
Y	crack shape function
Z	number of balls in a bearing
z	axis coordinate
β	Weibull slope
ν	Poisson ratio
σ	stress
σ_0	Weibull scale parameter

SUMMARY

The ARPA funded ceramic bearing technology projects address the issues of reliability prediction of ceramic bearings and bearing components. This particular project is aimed at developing reliability prediction techniques for silicon nitride ceramic bearings by using the basic approach of material testing of current state-of-the-art bearing grade silicon nitride ceramics.

Introduction and Background (Sect. 1)

Two types of commercially available hot pressed silicon nitrides (HPSN) were selected for testing and evaluation. These two baseline Si_3N_4 were Toshiba TSN-03H and Cerbec NBD-200.

Two kinds of testing were performed in this project using the above mentioned ceramic materials. One was the rotating beam fatigue test and the other was the hybrid ceramic ball bearing endurance test. The development of improved reliability prediction techniques started with the material characterization of the fatigue properties which were achieved by applying statistical methods and reliability theory (of ceramics) to the rotating beam test data of the two baseline materials. The volume flaw assumption was used, which permitted the failure probability to be expressed in terms of a volume integral of a function of tensile principal stress, the stress cycles and the material constants evaluated.

Rotating Beam Fatigue Tests (Section 2)

The rotating beam specimens were finished from the rod blanks by Chand-Kare Engineering Ceramics, Worcester, MA. Diamond wheels of 600 grits were used with longitudinal grinding applied for the final finishing of the specimens. The average rms surface roughness was $0.4 \mu\text{m}$. Rotating beam fatigue tests were performed at room temperature using four testing machines. 122 specimens were tested, which consisted of 62 Toshiba specimens and 60 Cerbec specimens. Most of the tests were performed with maximum bending stress in the range of 600-850 MPa. Three test completion modes were encountered, i.e. fast fracture at setup, fatigue fracture and runout (no failure). The total number of fast fractures was 14. Also, about 50 specimens were subject to multiple load or step-up load tests, most of which eventually failed.

Rotating Beam Data Analysis and Material Characterization

(Section 3)

Statistical methods were applied to the rotating beam data in two ways, both using the maximum likelihood technique. The first was to apply the maximum likelihood method to test data at constant load or maximum stress (σ) using available Weibull analysis software. This was followed by a regression analysis applied to the median life versus stress relationship to obtain the fatigue exponent. The second method treated, for each material, all the test data at different loads at once, including those with multiple load. In this analysis, a Weibull distribution was assumed apriori to exist between the failure probability and the quantity 'effective fatigue cycles' i.e. $\sum \sigma_j^n N_j$, where the index j is for different load steps. The median value of the effective cycles was then used to calculate the crack growth constant (B) in the failure probability formulation for a stressed volume.

Hybrid Ball Bearing Endurance Test (Section 4)

Endurance testing was performed with 206 size hybrid ball bearings using sudden-death method for a total of 48 bearings, 24 for each ball material. The bearings were liquid lubricated with full EHL film separation between ball and races. The bearings with Cerbec balls suffered one early failure, while the rest were suspended at a maximum of about 1500 hours. For the bearings with Toshiba balls, there was one ball failure in each of the four groups. The failure lives were in the range of 70-170 hours. In all the failed bearings, no failures were found to be initiated from the steel raceways. Failure analysis of the spalled balls showed that three balls contained fragments of metallic inclusions. No large inclusions were found.

The maximum likelihood method was used to analyze the ball failure data. The Weibull slope of the test bearings with Cerbec balls was very low (0.23), which is in qualitative agreement with the rotating beam test results. The low variability of failure lives (or Weibull slope = 3.1) in the Toshiba balls was not consistent with the rotating beam test data.

Contact Stress and Failure Probability Prediction for Ceramic Rolling Body (Sections 5 and 6)

For elliptical Hertzian contact stress field, with or without sliding friction, the subsurface tensile stress distribution was analytically determined and used as input to the volume integration of the stressed volume around the rolling track of a ceramic rod or ball. Numerical examples were used to obtain the failure probability of the ceramic rod in the RCF rig and a ceramic ball was used in the thrust loaded ball bearing.

Conclusions (Section 7)

The work performed led to a number of conclusions. The highlights are listed below:

- Most rotating beam tests of these two baseline materials were performed in the maximum bending stress range from 600-850 MPa, within which three completion modes occurred, i.e., fatigue, runout, and fast fracture.
- Many of the failures can be traced to material flaws in the silicon nitride specimens.
- The fatigue data of the rotating beam tests have wide scatter.
- The statistically determined fatigue exponents were higher than steel; the values of fatigue exponents for the two materials were drastically different.
- Failure probability was determined for the RCF ceramic rod and hybrid bearing ball sets, which shows strong dependence on maximum contact pressure and sliding friction coefficient.

Technology Transfer Issues

1. Four spalled TSN-03H balls and one spalled NBD-200 ball were sent to Mechanical Technology, Inc. These failed balls, together with several new balls of the two materials and unfailed balls from the failed bearings, also were tested using laser scattering technique by Dr. Bill Ellingson of the Argonne National Laboratory.
2. Several new and survived rotating beam specimens were sent to the Argonne National Laboratory for laser scattering measurement.
3. A total of 28 failed rotating beam specimens (14 for each material) were sent to Professor Jack Mecholsky of the University of Florida's Department of Material Science (an AFOSR contractor) for fractography, fracture toughness and other fatigue studies.

4. One failed rotating beam specimen (B14) of NBD-200 material was sent to Cerbec Inc. and Norton Research Center for evaluation.
5. Rotating beam fatigue life data have been made available to Enceratec, Inc. and NASA Lewis Center's Structural Integrity Group.
6. Technical presentations were made in the International Rolling Element Bearing Symposium at San Diego, CA (April 12-14, 1994), Saint-Gobain (Norton) Research Center, Northboro, MA (November, 1993) and the Army Material Technology Laboratory at Watertown, MA (March, 1993).

Appendices -

The five appendices contain the detailed rotating beam test data, the detailed formulations for stress volume, and the maximum likelihood analysis, as well as the hybrid bearing test report from the bearing test laboratory.

FOREWORD

The work documented in this report was performed at the Advanced Technology Center of The Torrington Company for the Advanced Research Project Agency (ARPA) and Wright Laboratory (AFSC) with the support of Dr. Bill Coblenz, ARPA Ceramic Program Manager, with Mr. Karl Mecklenburg as project engineer. The author gratefully acknowledges Dr. Coblenz and Mr. Mecklenburg for their keen interest and suggestions to this research work.

Acknowledgment is also due to the following personnel:

Jill Folkert, Randy Harding, and Douglas Bush of the Central Material Service Laboratory, Ingersoll-Rand Co., who performed the rotating beam fatigue testing of the silicon nitride specimens. Henry Daverio (Manager of Test Lab.) and Ken Galitello of the Fafnir Bearing Test Laboratory, The Torrington Co., who performed the endurance testing of the 48 hybrid ceramic bearings. Henry Skonieczny and Scott Crossman, who assisted in the selection of test bearing ring sets. Jim Koncki, Joe Braza, Steve Reder and Don Church, who assisted in fractography of the ceramic specimens.

On the technology transfer issues, we would also like to acknowledge the interest and investigation on failed ceramic specimens or test data by Dr. Bill Ellingson (Argonne Laboratory), Dr. J. Dill (MTI), Dr. J. J. Mecholsky (University of Florida), and Dr. N.R. Katz (Army Research Laboratory, Watertown, MA).

1.0 INTRODUCTION AND BACKGROUND

Future DoD systems require enhanced performance and durability for precision moving mechanical assemblies and actuator designs. Ceramic materials and advanced technologies applied to bearings and bearing components can meet these requirements by offering lighter weight, lower wear, better corrosion resistance, higher preloads, and improved geometric/dimensional stability. The principal barriers that have prevented the exploitation and wide acceptance of ceramic bearings are low operational reliability and high cost.

The ARPA funded ceramic bearing technology projects address the issues of reliability prediction of ceramic bearings and bearing components. This particular project was aimed at developing reliability prediction techniques for silicon nitride ceramic hybrid bearings by using the basic approach of material testing of current state-of-the-art bearing grade silicon nitride ceramics.

1.1 Objectives and Approaches

The objectives of this project were two-fold. The first was to establish a database for the effect of silicon nitride microstructure (flaw defects) on cyclic fatigue life using rotating beam fatigue (RBF) and hybrid bearing tests. Such microstructure includes "defects," such as voids, inclusions, second-phase particles as well as surface defects. The second was to develop improved reliability prediction methodology for hybrid silicon nitride rolling elements.

The approaches of the project were as follows:

1. Perform rotating beam fatigue (RBF) testing of two high quality Si_3N_4 materials.
2. Apply contact stress and statistical theory to predict bearing life using RBF test results.
3. Conduct confirmatory endurance tests with hybrid bearings using ceramic balls of the same two materials.

Figure 1 shows a flow chart of this research for Bearing Life Prediction based on the material flaw failure model. It has shown that material selection, testing and characterization, as well

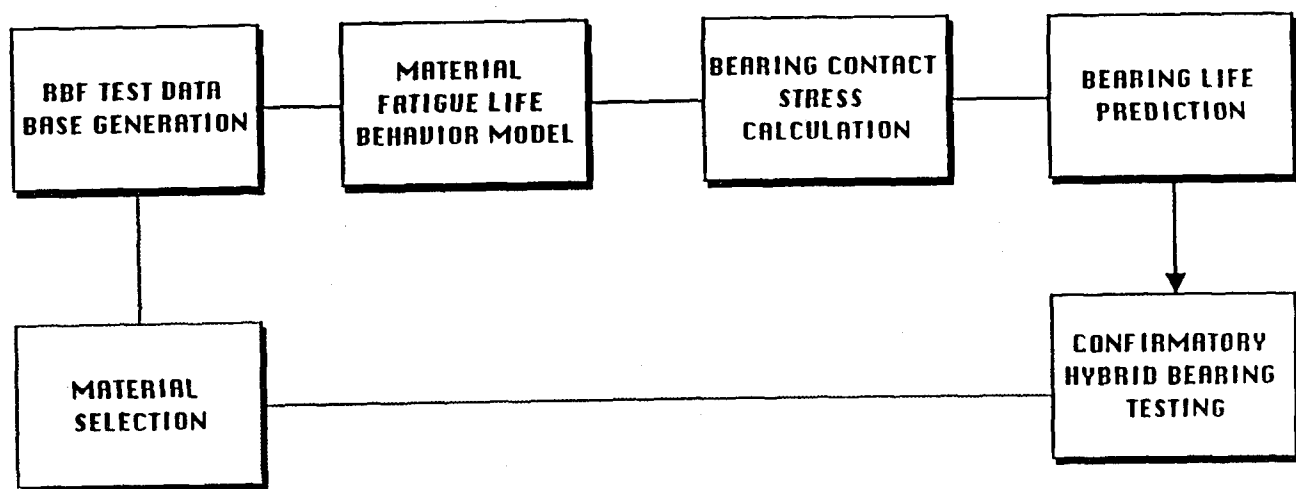


FIG.1 Flow Chart for Approach for Bearing Life Prediction
Based on Material Flaw Failure Model

as the application of reliability prediction techniques and contact stress theory, were needed in this research.

1.2 Background of the Problems

The great majority of rolling bearings used in applications today are made of alloyed steels of hardness around Rc 60. The use of ball and roller bearings in machines and vehicles is more than one century old. The reliability of rolling bearings (or service life) has been greatly improved with the improvement of steel quality, especially the cleanliness of steels, by the development of the vacuum melting process and special alloyed steels. These improvements in steel quality (i.e., microstructure and strength) have greatly reduced the likelihood of the so-called subsurface failures and lengthened the service lives of bearings.

Modern rolling bearing materials are expected to stand extreme high contact stresses. Therefore, among many available advanced ceramics, only the so-called bearing grade hot pressed silicon nitrides (HPSN) are currently being considered as the material of choice for ceramic rolling element bearing components.

In [1]^{*1}, Ebert gave an extensive review of silicon nitride material for ceramic bearings. In comparing silicon nitride and steels for aerospace bearing applications, he pointed out that silicon nitride is superior in its low density, high temperature hardness and strength. However, at low (or room) temperature, silicon nitride has bending strength lower than bearing steel. Ebert also stated that the life of modern hybrid bearings approaches that of steel bearings at the same maximum stress level. Katz et al. [2], in a review and assessment of ceramics for high performance bearings, pointed out that the current problem areas consist of brittleness, different design practices, reliability, reproducibility of product, and cost. Zaretsky [3], in 1989, reviewed the rolling contact fatigue data of silicon nitride in tests performed in the 70's and concluded low reliability in silicon nitride rolling element when compared with modern bearing steels used in the aerospace applications. However, during the past 15 years, material

^{1*} Numbers in brackets indicate references listed beginning on page 117.

improvement has significantly changed this assessment.

Much test data of hybrid silicon nitride rolling element bearings are now available, indicating spalling as a major failure mode as in steel material. While the origin of spalling in ceramic balls cannot be easily identified in many failed hybrid ball bearings [4], tests with RCF tested at very high contact stress (> 6 GPa or 900 ksi) clearly show cracking at the edge of the rolling track. Lucek [5], Baumgartner, et al. [6] and Katz [7] have attributed this failure to the high tensile stress at the edge of a Hertzian contact. A similar finding has been reported [8] for the track edge cracking on silicon nitride rings in full ceramic ball bearings.

It is generally believed that because of the recent rapid progress in the development of new bearing grade silicon nitrides, rolling contact endurance test data of silicon nitride materials over five years old may be considered to be obsolete.

As new silicon nitride materials have been developed to achieve improved performance in hybrid bearings, one of the major difficulties is the lack of an established understanding of the dependence of fatigue performance on microstructure and mechanical properties. For advanced ceramic materials, there are no standard materials, no standard processing techniques, no standard fatigue test procedures, no NDE method for evaluating material integrity.

There are very little fatigue data published on hot pressed silicon nitride (HPSN) ceramics. In research of bearing steels, rotating beam fatigue tests have been used [9,10] to assess the effect of steel cleanliness (i.e., inclusions) on fatigue life. In Japan, Ko [11] conducted rotating beam tests, and Masuda et al. [12] performed resonant cyclic fatigue tests. Both used sintered silicon nitride material.

The classical Lundberg Palmgren theory [13] for rolling contact fatigue life considers that the critical stress which determines the fatigue life is the orthogonal shear stress in the Hertzian contact stress field. This theory also neglects the failure probability of the rolling elements in bearings. It is generally believed that this theory is not valid for ceramic rolling elements, in

which the failure is governed more by the tensile stress than by the shear stress.

1.3 Test Material Selection and Properties

Two types of commercially available silicon nitride ceramics have been selected, i.e., Toshiba TSN-03H and Norton/Cerbec NBD-200. These materials are the most advanced bearing-grade silicon nitride candidate materials for rolling contact components. Previously, under U.S. Air Force Contracts, these two materials were evaluated in rolling contact test rigs as well as in wear test rigs [14,15]. Table 1 shows the material property data from the suppliers. It is shown that TSN-03H have values of thermal expansion coefficient and fracture toughness higher than that of NBD-200. Table 1.2 shows the material impurity specification of the two silicon nitrides.

The suppliers, i.e., Norton/Cerbec and Toshiba Companies, have also performed Modulus of Rupture (MOR) tests using the MOR bars to obtain the statistical distribution of the bending strength. From these data, it is possible to obtain the Weibull modulus and the scale parameter for the two materials. Fig. 2 shows the Weibull plots of the bending strength of the two baseline materials based on the MOR test data obtained by the suppliers. The method of the bending test is different for the two suppliers, i.e., Toshiba Co. uses the three point bending test, while Norton/Cerbec uses the four point bending test, according to Mil. Std 1942B.

Table 1 MATERIAL PROPERTY DATA OF THE BASELINE S_3N_4

Material:		TSN-03H	NBD-200
Density	gm/cm ³	3.22-3.25	3.16
Elastic Modulus	GPa	290-300	320
Poisson Ratio		0.26-0.28	0.26
Coef. Thermal Expansion	10 ⁻⁶ /C	2.9-3.2	1.6
Hardness, Rc		NA	> 70
Hv	GPa	14-17	16.6
Flexure Strength	MPa	> 730	800
Tensile Strength	MPa	NA	400
Fracture Toughness	MPa. m ^{1/2}	6.4	4.1
Compressive Strength	MPa	> 4000	3000

Table 1.2 MATERIAL IMPURITY SPECIFICATIONS
(in percent by weight)

	Al	Y	Ti	O	C	Mg	Ca	Fe
TSN-03H	3.5-4.5	3.0-4.0	0.5-1.	5.0-7.0	0.5-1.0	≤0.1	≤0.1	≤0.1
NBD-200	≤0.5	NA	NA	NA	NA	≤1.0	≤0.05	≤0.5

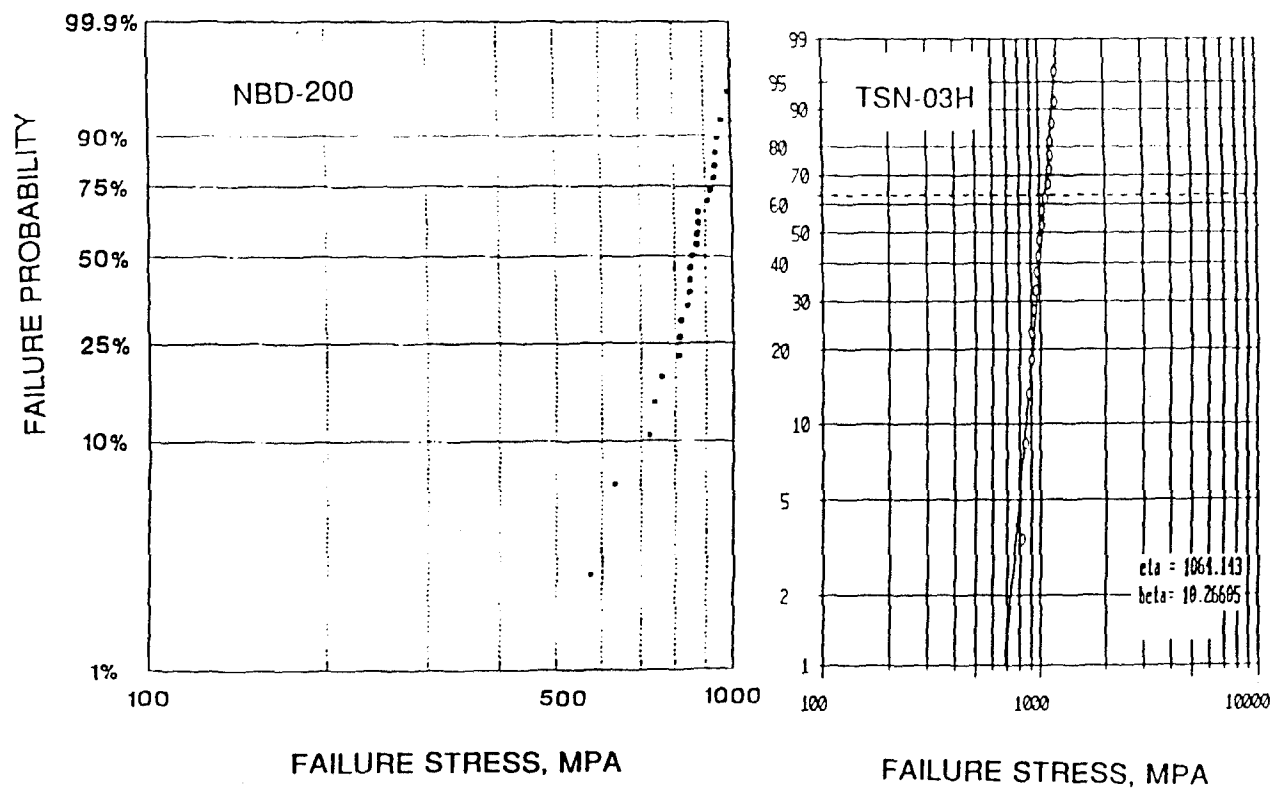


FIG.2 Weibull Plots of Failure Stress Based on MOR Data

2. ROTATING BEAM FATIGUE EXPERIMENT

2.1 Rotating Beam Specimen Fabrication

Figure 3 is a design drawing of the RBF specimen used for testing in the standard Moore rotating beam test machines. First, rod blanks of 76.2 mm (3 in.) long and 9.52 mm (3/8 in.) in diameter have been purchased from two suppliers, i.e., Enceratec, Inc. and Norton/Cerbec Co. Fig.4a shows the rod blank, finished and tested (fractured) specimens. Fig.4b is a photograph of 70 newly received finished specimens of TSN-03H material. It was required that all specimens be finished with longitudinal grinding using 600 grit diamond wheels.

All test specimens have been finished by Chand-Kare Engineering Ceramics, Worcester, MA over a period of 5 weeks. Prior to fabrication, samples were made by Chand-Kare and several other vendors. The circumferential rms roughness of the samples finished by Chand-Kare is about 0.4 μm .

All the finished specimens have a rms roughness Ra value less than 1 μm . Even though the specimens are finished by numerical controlled grinding machines, inspection of the specimen surface finish shows that the finish varies from specimen to specimen, based on the use of the diamond wheels. For identification purposes, the ends of the RBF specimens are marked with numbers, from A-1 to A-72 in which "A" denotes the TSN-03H and "B" denotes the NBD-200. The latter specimens are marked with numbers B-1 to B-71.

All the specimens are visually inspected using a low power microscope prior to testing. The surface quality of each specimen is rated and recorded. The rating consists of three categories, i.e., sample quality (class 2), better than sample quality (class 1) and marginal quality (class 3). The record of surface finish is given in Appendix A.

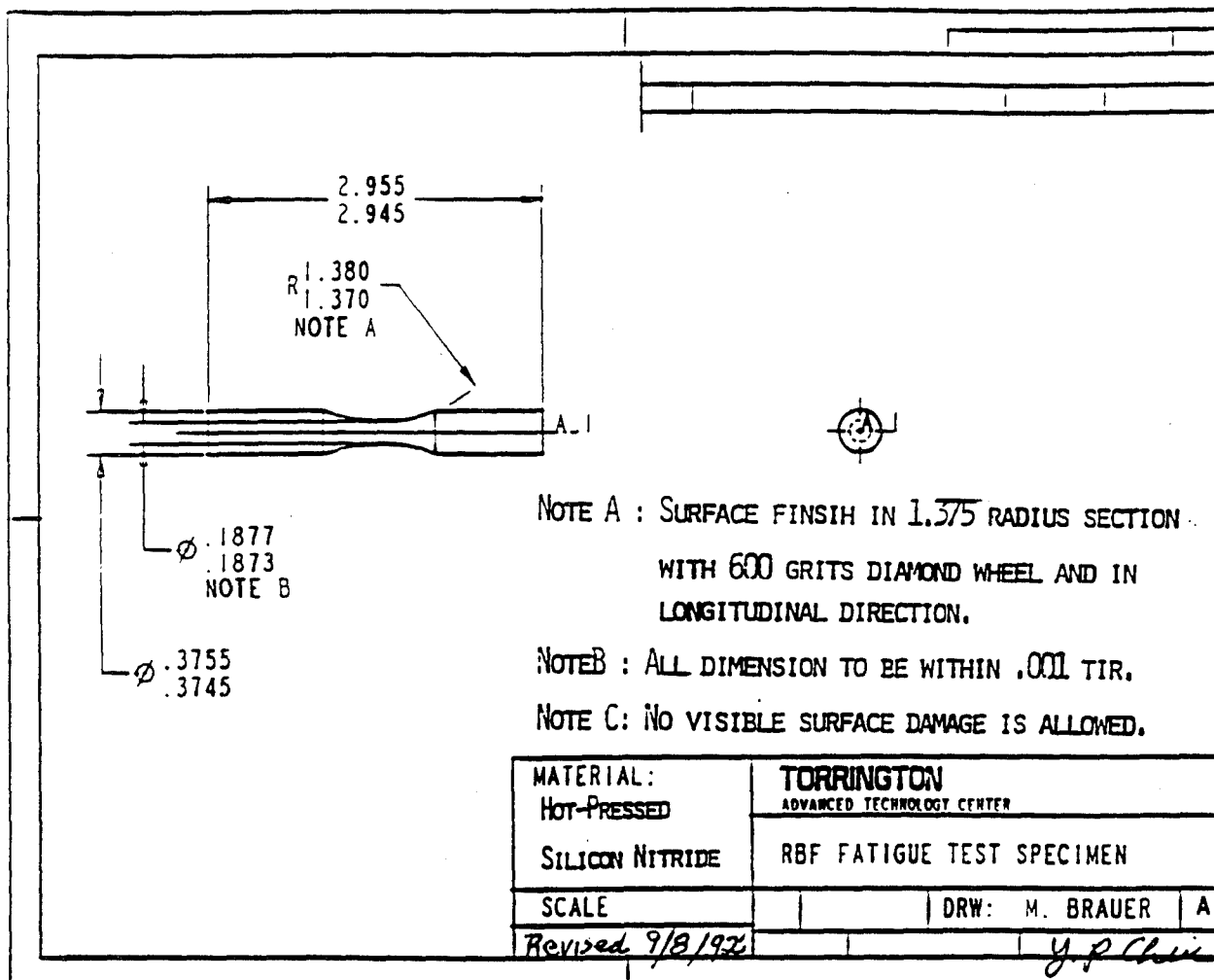


FIG.3 Design Drawing of the Rotating Beam Specimen

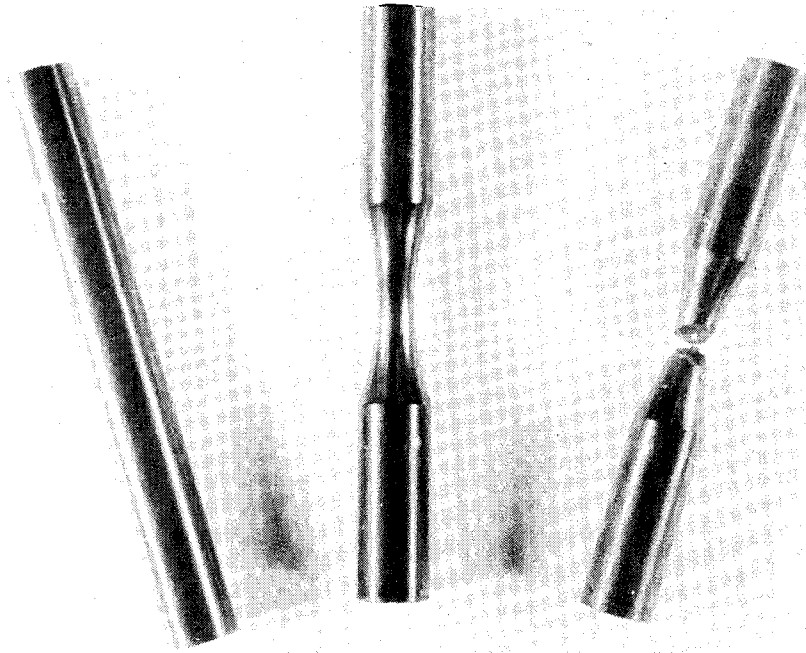


FIG. 4a Photograph of Rotating Beam Specimen, Rod Blank and Fractured Specimen

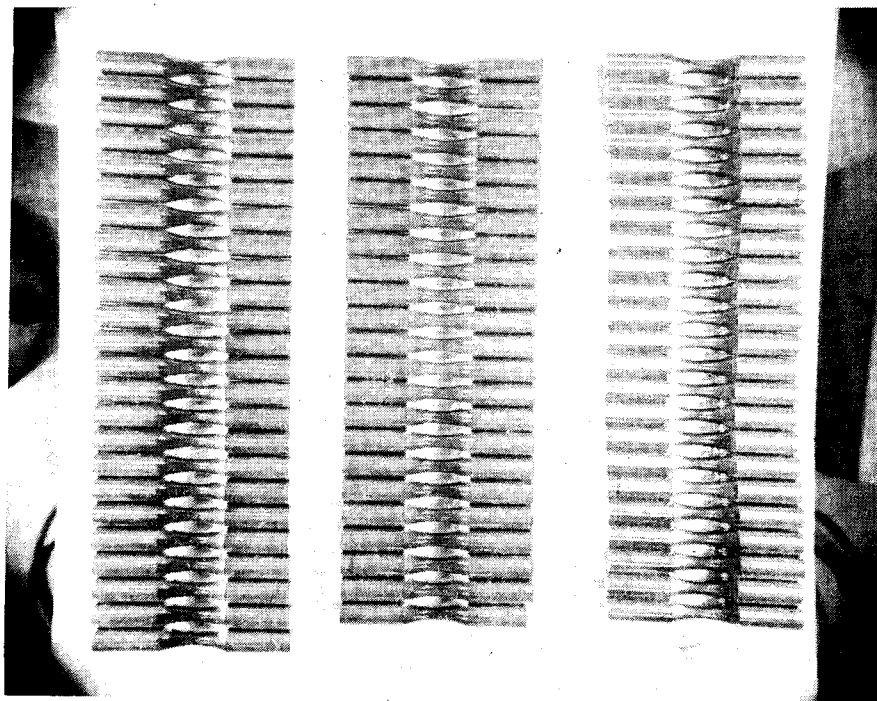


FIG. 4b Photograph of 70 Finished Rotating Beam Specimens

2.2 Rotating Beam Fatigue (RBF) Testing

2.2.1 Test Rig and Preliminary Tests

The rotating beam fatigue testing was conducted using four Moore rotating beam testers in the Ingersoll-Rand Central Material Service Laboratory in Phillipsburg, N.J. The test preparation and test conditions are as follows:

The rotational speed of the test machine was selected to be 6000 cycles per minute, or 360,000 cycles per hour. The test rig has a maximum speed of 10000 cycles per minute. This maximum speed was not used in order to avoid vibration at the top speed.

Figure 5 plots the relation between the maximum tensile stress in the RBF specimen and the applied bending moment of the rotating beam test rig. The relation between the tensile (fiber) stress and the bending moment is based on the formula: $\sigma_z = M r/I$, where M is the bending moment, I is the moment of inertia and r is the radius σ_z is the fiber stress (z-direction) on the specimen surface and σ_{z0} is the maximum value of σ_z at the gauge section of the specimen.

$$\sigma_{z0} = M R / I \quad (1)$$

where M is the bending moment, R and I are respectively the radius and moment of inertia at any section with z =constant, i.e.,

$$R = R(z) = R_0 + R_c + (R_c^2 - z^2)^{1/2} \quad (2)$$

$$I = I(z) = \pi R^4 / 4, R_0 = R(0)$$

R_c is the profile radius of the BRF specimen.

Prior to the test set up, an optical comparator was used to check the dimensions of the specimens to be tested. The diameter of the gauge section was measured and recorded. During the set-up process, the specimen was tightly fitted to the clamp which was connected to the spindle end of the machine. Using the dial indicator, the free end of the specimen was adjusted to have a radial runoff of less than 0.001 inch prior to applying the load. The runout of the specimen at the

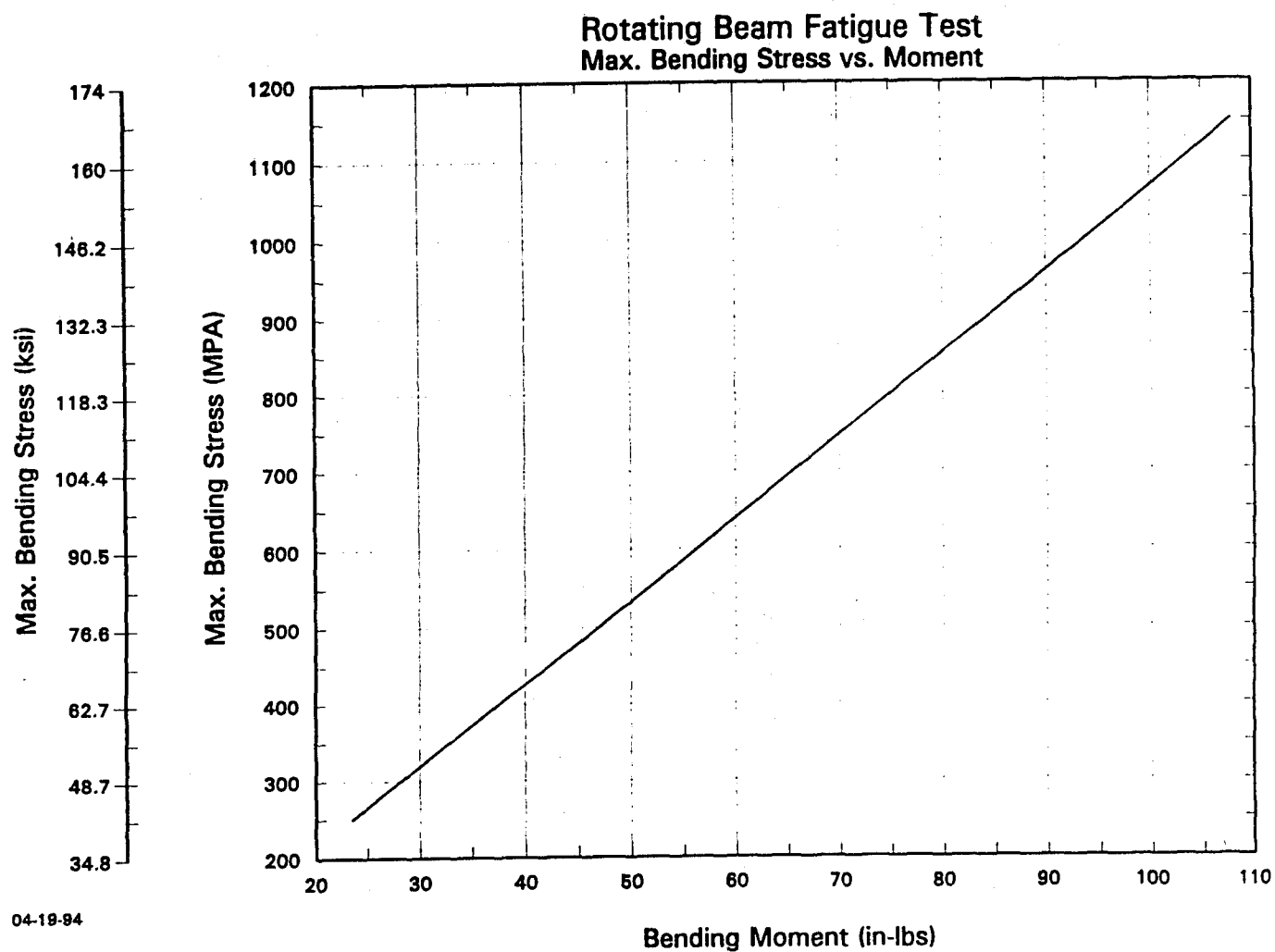


FIG.5

Relation Between Maximum Bending Stress and
Bending Moment in the RBF Tester

spindle end was also measured using the dial indicator and recorded for each of the tests. The load was applied by bending moment, which can be set by a scale below the spindle. The unit of the scale is inch-lbs.

Because of the lack of prior test data for this material in rotating beam tests, the initial test load (or bending moment) applied was first determined by an exploratory trial and error method. At the start of the test, a bending moment of 47 in-lbs was applied, which corresponded to a maximum bending stress of 500 MPa or 72.5 ksi. No failure occurred at the load and the test was suspended at 103 million cycles. In subsequent tests with other specimens, the test load was increased to 70 and 80 in-lbs. At the latter load, several fractures occurred after a number of stress cycles as well as during the set-up. Other test loads used were 75, 65, 60 and 55 inch lbs. At lower loads, there is increasing tendency of test suspension after over 100 hours of tests.

Each of the failed or suspended specimens was placed in an envelope marked with the specimen number, test conditions, and test life (at failure or suspension).

2.2.2 Test Completion Modes

The rotating beam fatigue (RBF) testing was completed in a period of about 5 months. A total of 122 RBF specimens were tested and consisted of 62 specimens of TSN-03H and 60 specimens of NBD-200. The total test hours with the four test machines was about 7200 hours.

The test load, failure mode, maximum stress and test life were tabulated in Appendix A. Based on this record, a computer database was completed, which was used as an input program to be read in as input in the statistical analysis given in the next section. There were three test completion modes, which consisted of:

- 1) **fatigue fracture (F)**, i.e. failure after a finite number of stress cycles.
- 2) **fast fracture (FF)**, i.e. failure occurred during the setup process. There were seven specimens each (for the two materials) fractured during the setup process. The causes for the fast fracture could have been due to human error in setup or flaws in specimens,

similar to that in the MOR bending test of bars.

- 3) **runout** (S) no failure at a large number of stress cycles, i.e., 30-100 million cycles. These runout cases were treated as 'suspensions' in the statistical analysis.

2.3 Test Results

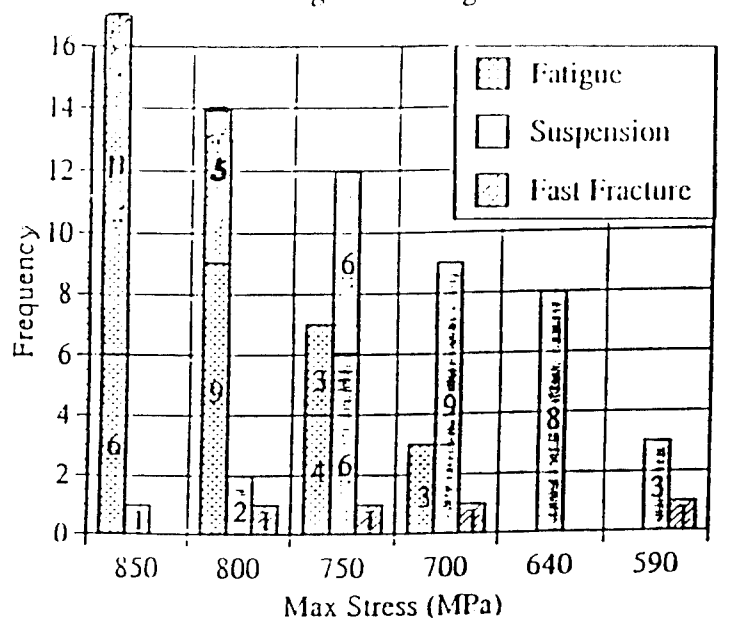
Figure 6 shows the histograms of the test completion modes of the two materials. The results show that for both ceramics, the number of fatigue failure occurrences dropped rapidly with decreasing maximum stress. The rate of decrease for the number of fatigue failures with decreasing maximum stress was more rapid in NBD-200 than in TSN-03H, even though in the former, one fast fracture occurred at very low maximum bending stress of 590 MPa. It was also shown that the rate of decrease for the fast fracture mode with stress was slower in NBD-200 than in TSN-03H.

Most of the tests were performed in the range of maximum tensile stress from 600-850 MPa. Below 600 MPa, very few specimens failed after many ($30-100 \times 10^6$) stress cycles, whereas above 850 MPa, an increased number of specimens fractured during setup. The maximum runout cycles was 108 million cycles.

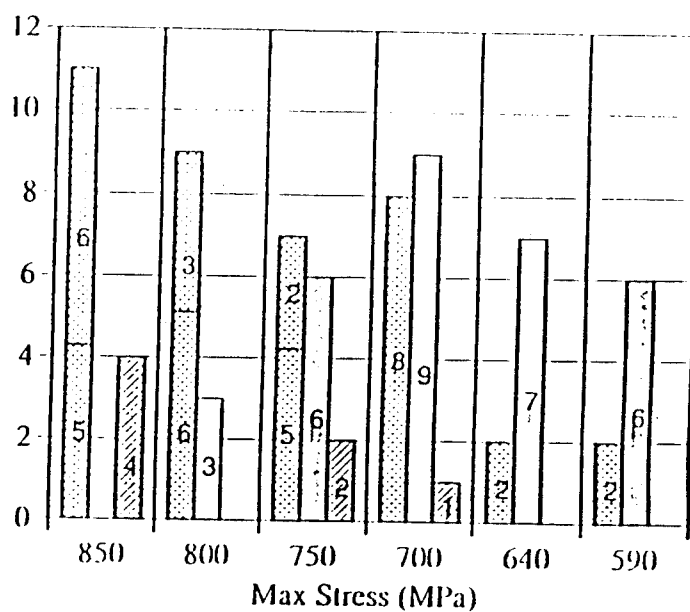
Tables 2 and 3 contain, for the two materials, the summary of the test results for the RBF tests performed at different levels of bending moments or maximum stress levels. The data show there was an increased number of suspensions (denoted by S) and a decreased number of fatigue failures (denoted by F) as the maximum stress decreased.

Figure 7 shows the stress versus cycles (S-N) plots for the RBF test of the two materials. The data points on the right side of the plot were the suspended tests while those on the left side show the fast fracture data. Figure 7 shows that the data points for the fatigue lives in this stress range were subject to wide (about 3 orders of magnitude) scatter. The calculated Weibull slopes were less than one.

Cerbec NBD-200
Rotating Beam Fatigue Test



Toshiba TSN-03II
Rotating Beam Fatigue Test



Note, the lower number in bars denotes number of tests with new specimens, the upper number denotes number of tests with survived specimens

FIG.6 Histogram of the Rotating Beam Fatigue Tests with Three Completion Modes, Fatigue, Runout and Fast Fracture

Table 2 Summary of Rotating Beam Fatigue Test Result for TSN-03H

Material: Silicon Nitride Ceramic
TSN-03H (Toshiba)

Speed : 6000 cpm
Date: MAR 28 , 1993

Moment (in-lb)	Smax		Cycles		
	(MPa)	(Ksi)			
80	850	124	31,900	42,300	207,300
			396,600	1,903,300	35,500*
			591,800*	2,708,000*	311,900*
			8,419,900*	614,500*	
			1 , 1 , 1 , 1	**	
75	800	116	190,200	514,800	2,914,700
			408,900	3,466,800	619,300*
			5,840,300	2,091,000*	9,102,300*
			(S) 33,373,500*		
			(S) 41,207,400	(S) 31,690,100*	
70	746	108.1	31,600	249,800	3,331,300
			9,800	460,100	975,600*
			(S) 68,964,800*	(S) 75,160,900	
			(S) 7,000,000	(S) 67,500,500	
			(S) 9,833,000*	(S) 36,881,000	
65	692	100.4	401,800	756,000	7,709,500
			221,000	1,410,400	1**
			639,800	349,200	365,600
			(S) 36,170,500	(S) 55,218,600	
			(S) 36,133,200	(S) 40,093,700	
			(S) 20,254,100	(S) 23,399,600	
			(S) 23,788,000	(S) 23,450,000	
60	639	86.1	(S) 20,030,200		
			3,964,200	6,092,500	
			(S) 36,163,700	(S) 36,239,000	
			(S) 36,318,500	(S) 20,780,200	
			(S) 19,674,100*	(S) 32,886,100*	
55	586	85.0	(S) 24,356,000*		
			1,634,900	7,354,800	
			(S) 47,317,200	(S) 39,562,700	
			(S) 103,928,500	(S) 20,488,100	
47	500	72	(S) 24,314,200	(S) 20,122,200	
			(S) 104,233,200		

* '(S)' denote suspended tests

** specimen broke in set-up

* Test life with specimens survived from low load tests

Table 3 Summary of Rotating Beam Fatigue Test Result for NBD-200

Speed : 6000 cpm Date: MAR. 28 , 1992			
Moment (in-lb)	Smax (MPa)	(Ksi)	Cycles
80	850	124	2,000 11,800 1,639,600 17,900 3,053,500* 1,057,400* 51,400* 30,900* 1,100* 2,890,000* 958,700* 16,100* 397,100* 74,400 152,200 (S) 30,318,000*
77	818	119	8,200 10,100 1,905,800 1, 1 **
75	800	116	38,000 9,100 314,800 3,225,100 10,262,400 1,406,500 270,100* 870,300 2,721,100* 60,700* 18,900* 8,560,300 28,987,600 1** (S) 58,840,000* (S) 21,483,900*
72		111	(S) 44,120,600 (S) 44,120,600
70	746	108	31,500 1,124,400* 1,086,300 1** 8,900 23,697,900* 8,300 3,996,500* (S) 36,094,200 (S) 40,784,500 (S) 20,962,000 (S) 26,532,800 (S) 20,564,200* (S) 46,488,700* (S) 19,802,100* (S) 19,975,000* (S) 21,369,000* (S) 34,179,000 (S) 19,456,000 (S) 40,680,000*
65	692	100.4	462,000 1,500 4,391,900 1** (S) 18,030,000 (S) 39,114,800 (S) 23,000,000 (S) 31,523,500 (S) 26,945,000 (S) 30,176,300 (S) 22,314,000 (S) 20,115,800 (S) 30,625,800
60	639	86	(S) 6,518,260 (S) 17,577,000 (S) 20,250,100 (S) 20,370,200 (S) 20,220,100 (S) 20,092,400* (S) 22,35,100* (S) 20,618,100
55	586	85	(S) 36,656,200 (S) 20,040,100 (S) 20,427,300 1**

* '(S)' denote suspended tests

** specimen broke in set-up

* Test life with specimens survived from low load tests

ROTATING BEAM FATIGUE TEST - STRESS LIFE PLOTS

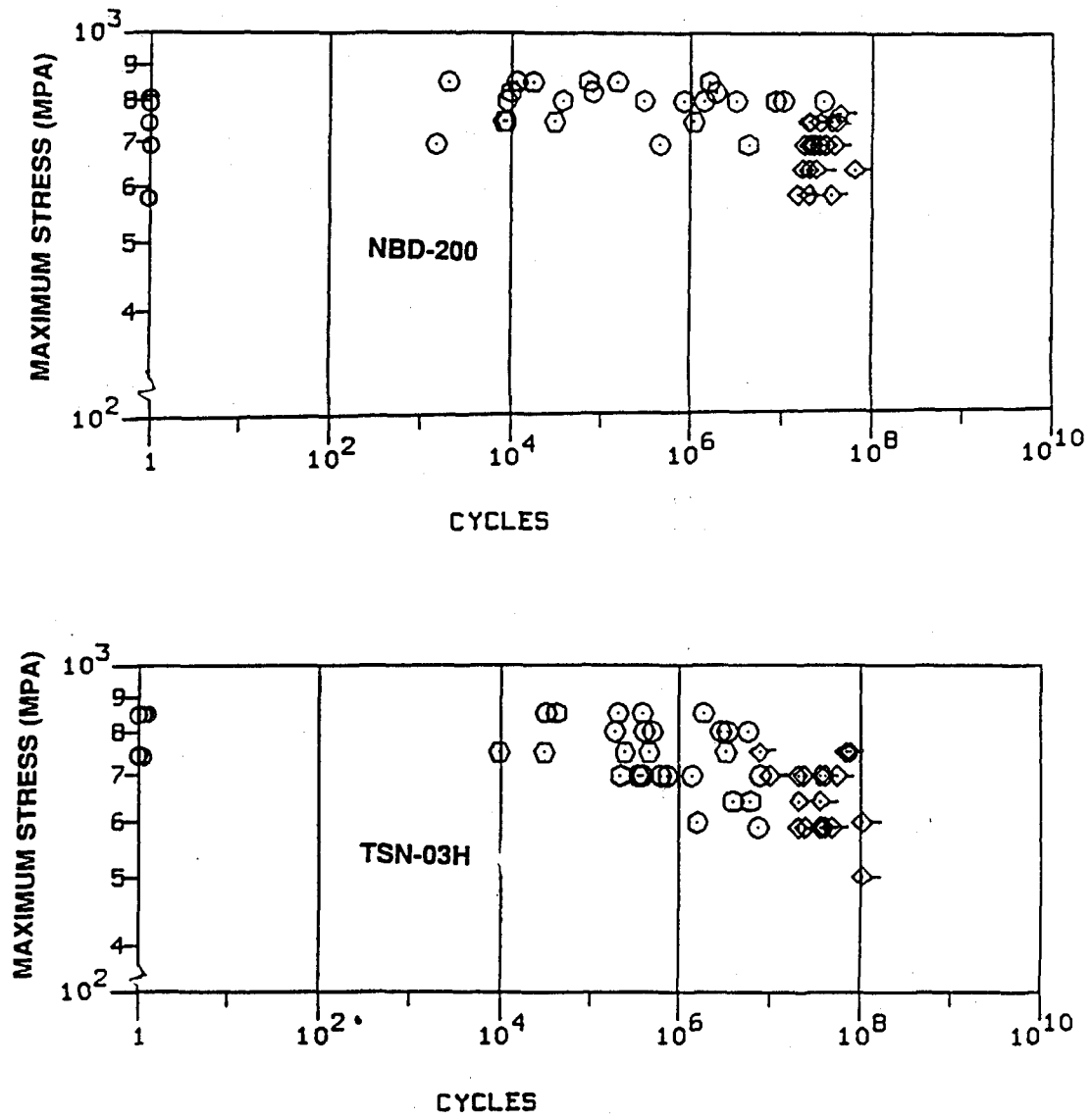


FIG.7 Stress-life Plots of Rotating Beam Fatigue Testing

2.3.1 Stepwise Load Test

Most of the rotating beam tests were conducted with new specimens. It was found that if the maximum stress was not high enough, runout or suspension would result. This was particularly true for tests at stress levels < 700 MPa, in which the runout modes became dominant. Since the number of available test specimens was limited, it was felt to be necessary to test some survived specimens, which had not failed in tests at low stress levels.

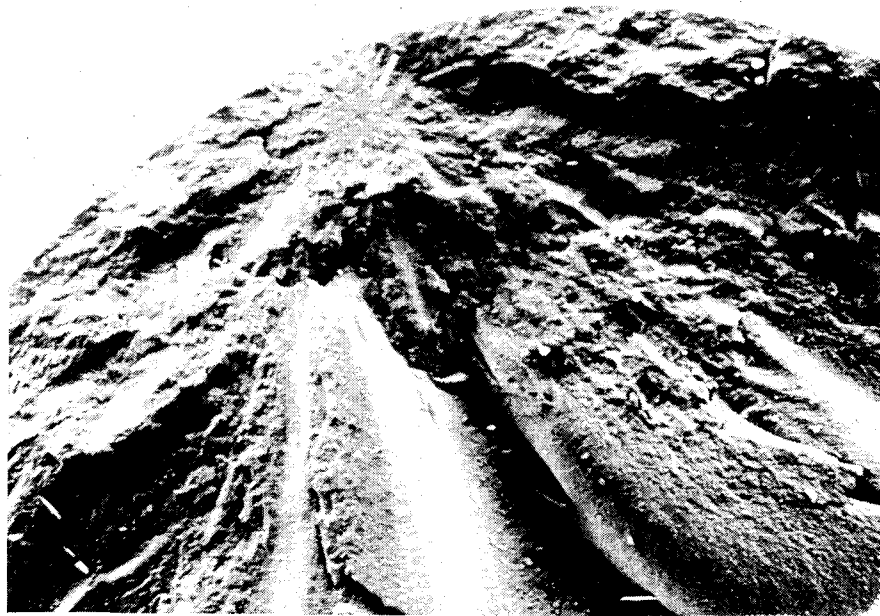
To remedy the above mentioned problems, some additional (50) RBF tests were performed at increased maximum stress levels with runout specimens which survived tests at a lower stress level (or levels) after 30-100 million stress cycles. More failures resulted at this step-up (multiple load) test procedure. The test data of this stepwise load test are also given in Appendix A.

Note that in published literature [16-18], several researchers have conducted cyclic tensile fatigue tests on ceramics using the stepwise loads, or 'saw-tooth loading waveform' approach, to ensure failure data for each specimen. In each of these tests, the number of cycles between each load increment varied from 10^4 to 10^5 , which is much smaller than in the present test.

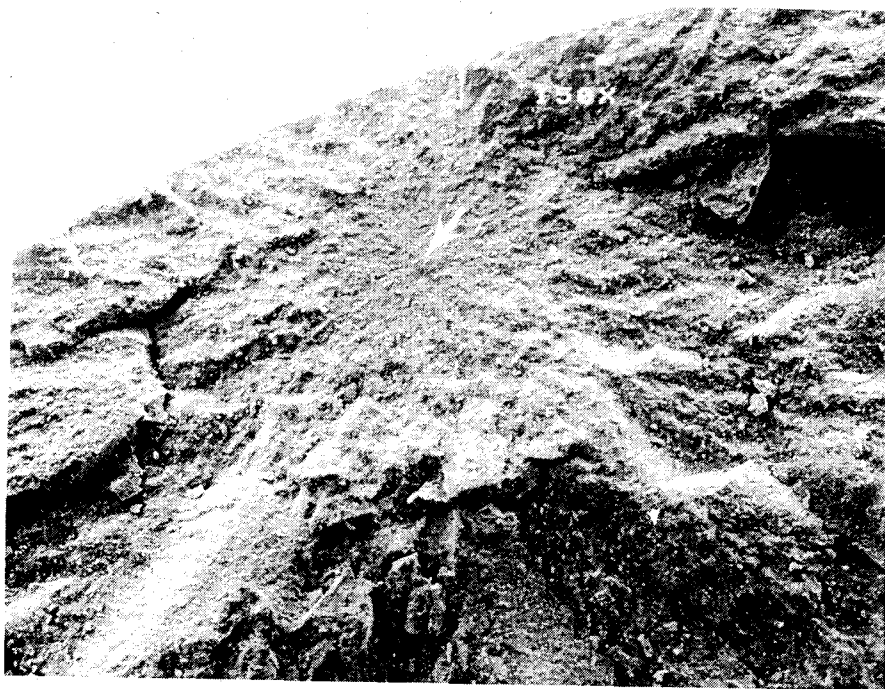
2.4 RBF Specimen Failure Analysis

2.4.1 Fractography of TSN-03H Specimens

Figures 8-10 contain the fractography at different magnifications of failed specimen No. A37 (Toshiba material), which was run under a maximum stress of 850 MPa (80 ksi) for 1,903,300 cycles prior to fracture. A series of photomicrographs were obtained using SEM with a multitude of magnifications, i.e., 50X, 150X, 1,000X, 5,000X, 10,000X and 15,000X. The stereo-microscope was first used to locate the fracture origin. The micrographs show the failure origin (by a white arrow), which appears to be a material defect. As explained in [19,20], the fracture origin is surrounded by radial ridges, commonly referred to as mist and hackle. Prior to the SEM examination, the fractured surface was first coated with a thin layer of gold. The high magnification micrographs ($> 10,000X$) in Fig.10 show the flaws are a cluster of inclusions of very small sizes (2-3 microns in diameter).



50x



150x

FIG. 8 Fractograph of Rotating Beam Specimen No. A37 (50x, 150x)
(Failure origin indicated by a white arrow)

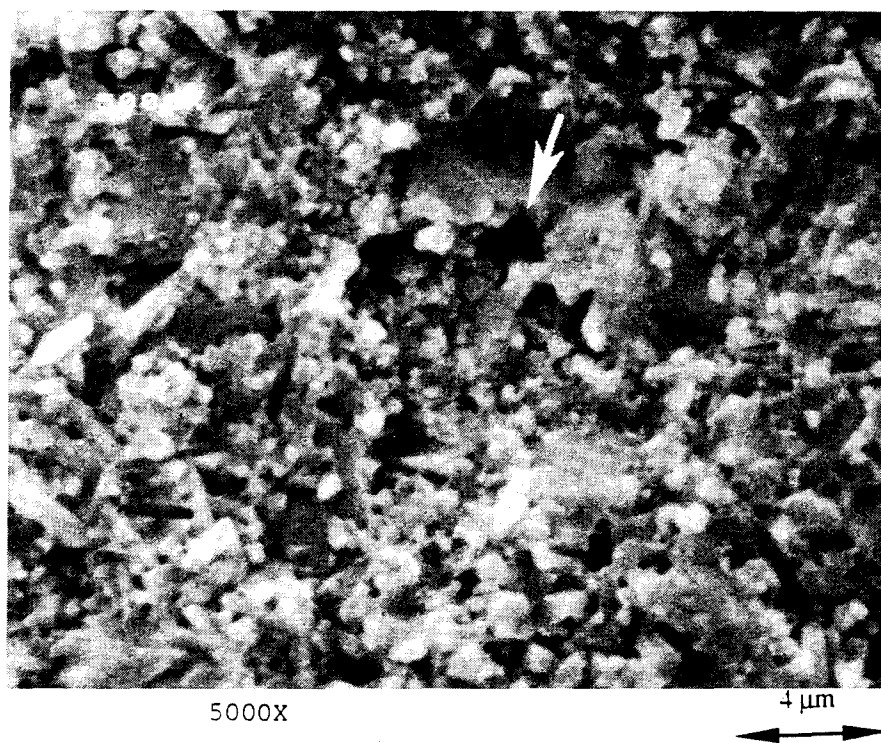
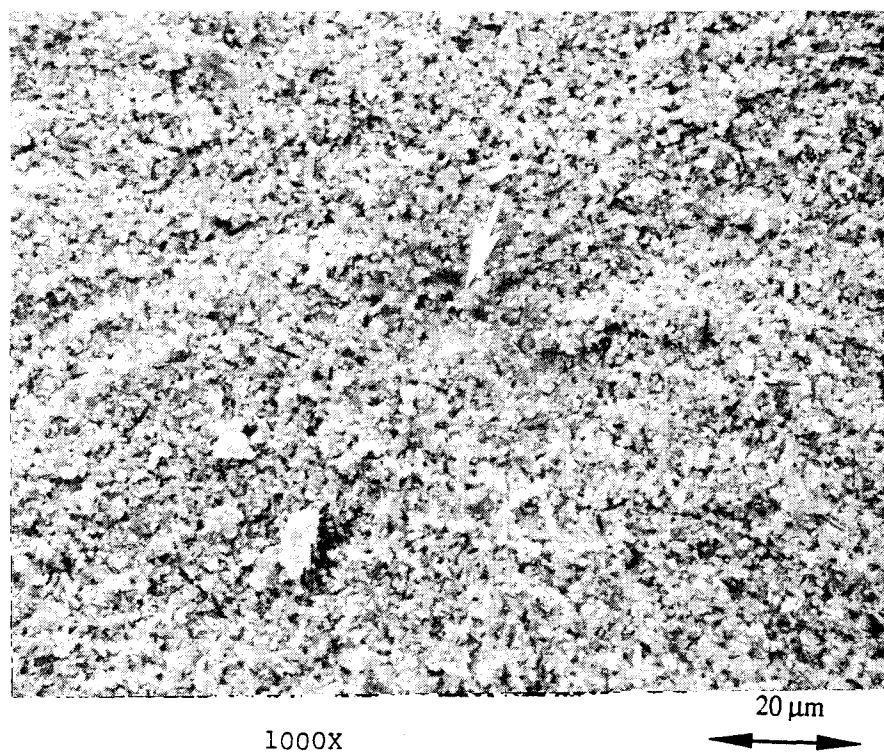


FIG. 9 Fractograph of Rotating Beam Specimen No. A37 (1000x, 5000x)
(Failure origin indicated by a white arrow)

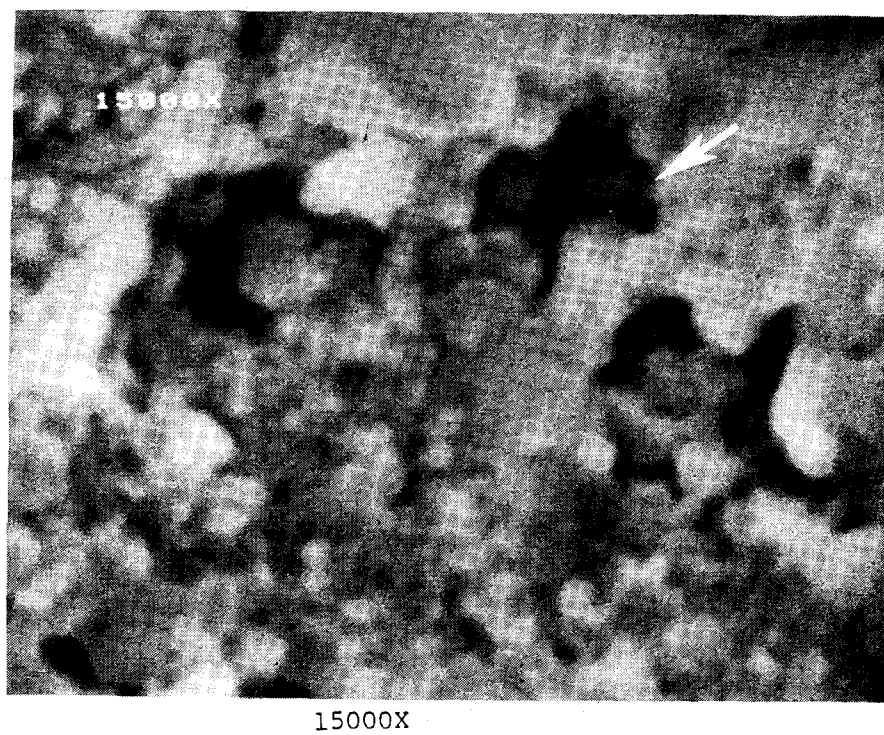
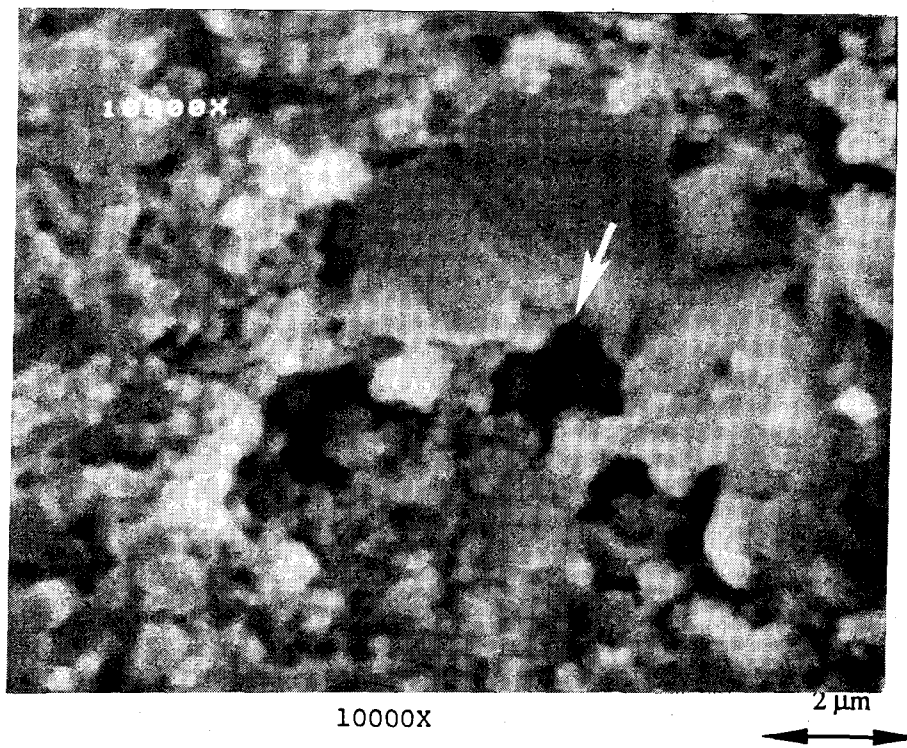


FIG. 10 Fractograph of rotating beam specimen No. A37 (1000x, 1500x).

The failed specimen (No A37) was further examined using the EDX analyzer. The EDX examination of the flaw region (see Fig.11) showed the presence of aluminum (Al) and silicon (Si), as well as gold (Au), which was the material for the coating used in the SEM examination. This examination showed that the failure origins contain aluminum, even though they have the appearance of pores.

The SEM fractograph shows the failure origin covering an area of diameter of about 20 microns, while the surrounding mirror region has an approximate diameter of 85 microns. The applied stress at the defect was about 800 MPa. Using the well known Mode I stress intensity formula for a penny shaped crack, i.e.,

$$K_I = 2 \sigma \sqrt{a/\pi} \text{ and}$$

- 1) by considering the defect region as a penny shaped crack, the fracture toughness for crack initiation is about $2.7 \text{ MPa(m)}^{1/2}$
- (2) by considering the mirror region as a penny shaped crack, the fracture toughness for fast fracture is about $6 \text{ MPa(m)}^{1/2}$.

Figures 12 and 13 show the SEM fractography of a TSN-03H specimen A-43, which was tested under maximum stress of 750 MPa and failed at 9,800 cycles. This fractograph^{*2} clearly shows a large pore of about 50 microns in size in the subsurface region of the specimen. The depth of this flaw was about 25% of the radius of the fractured section, indicating the maximum stress at the flaw was about 75% of the maximum bending stress at the OD of the gauge section, or $750 \times 0.75 = 563 \text{ MPa}$. Fig.14 shows the EDX plot of the failed region. The plot shows the presence of Yttrium at the inner edge of the pore.

² Courtesy of Dr. N.R. Katz, Army Research Laboratory, Watertown, MA.

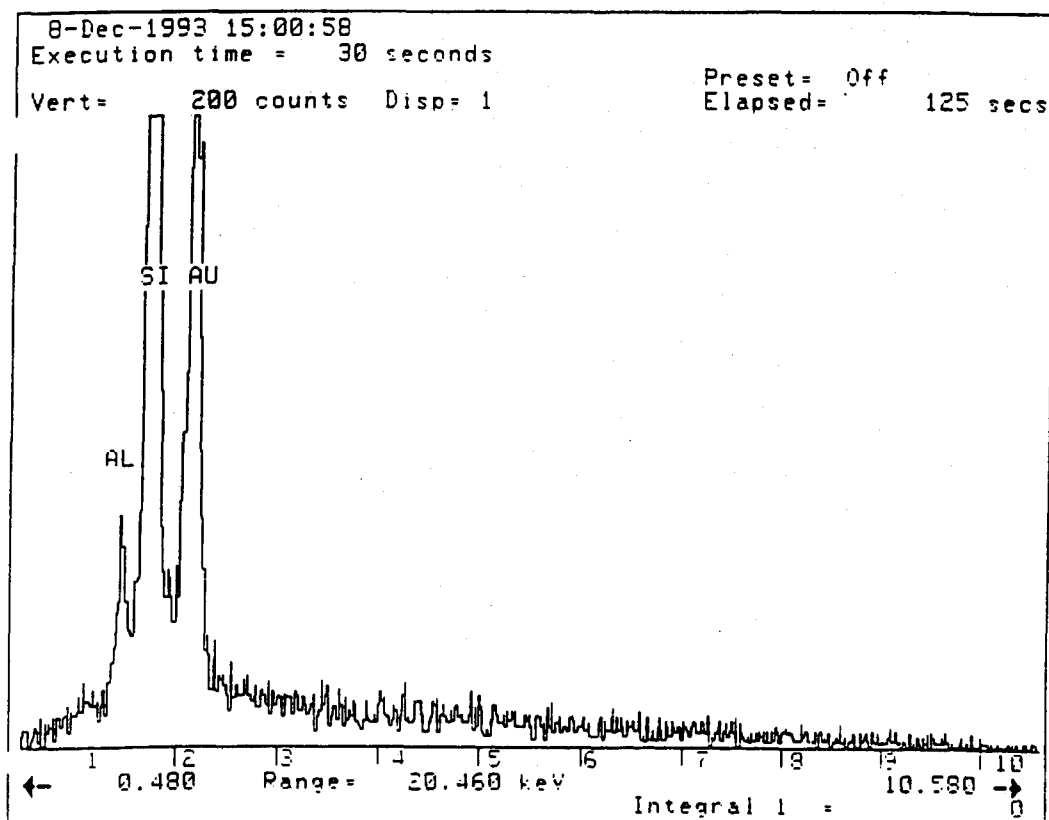


FIG.11 EDX result of specimen A37

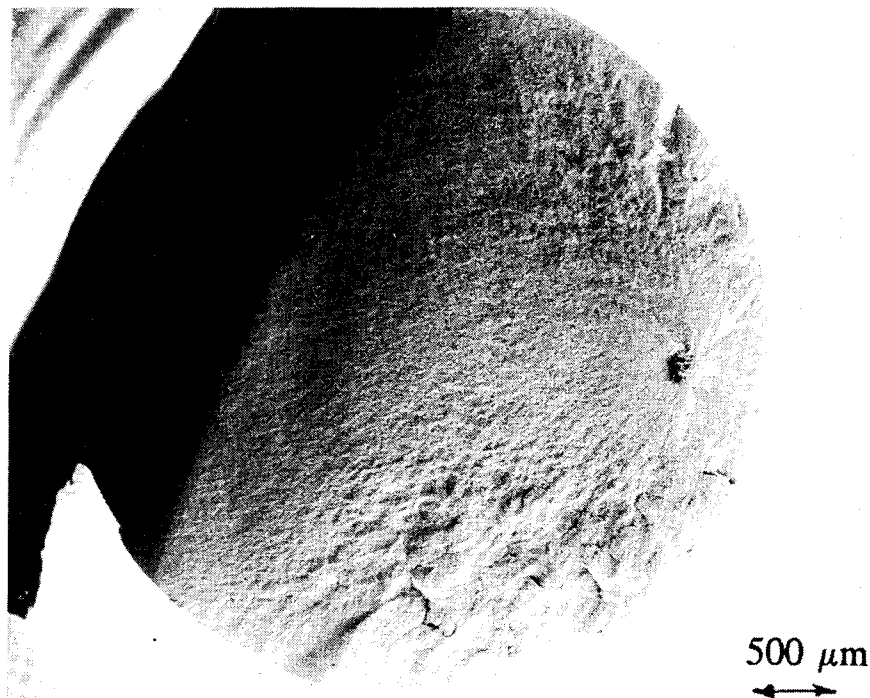
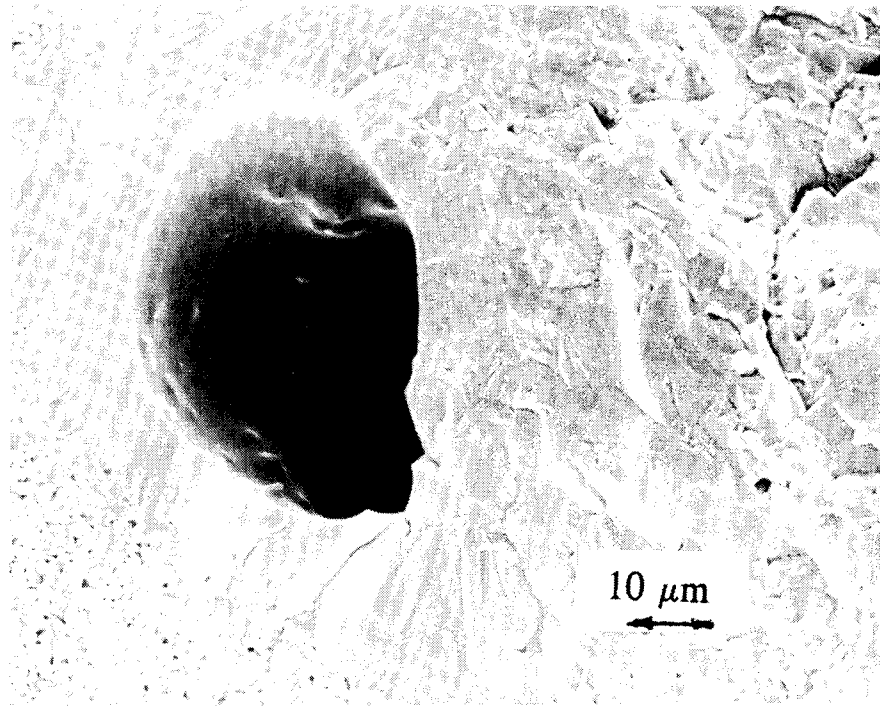
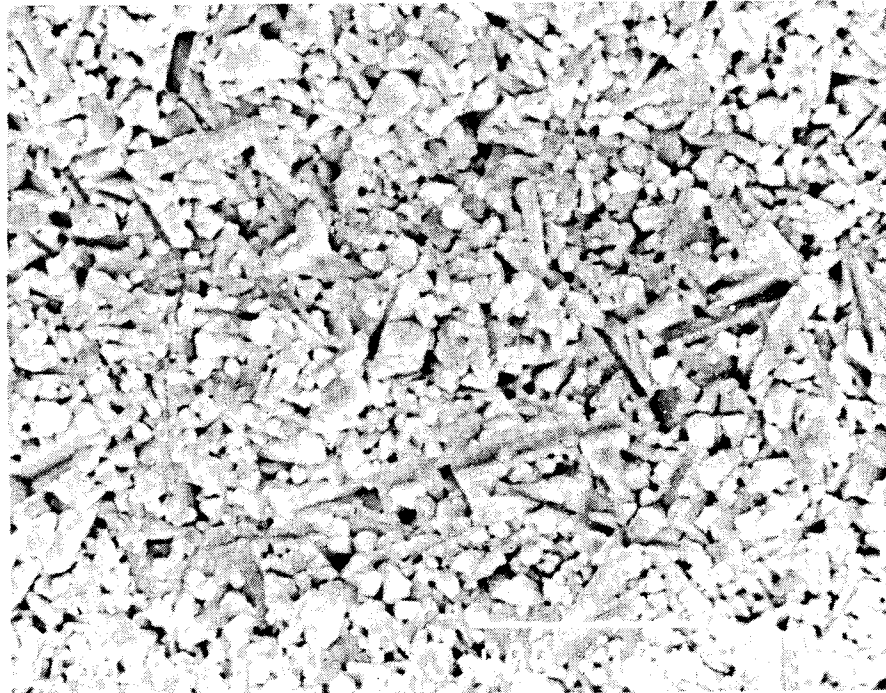


FIG. 12 Fractography of rotating beam specimen A43 (20x, 1000x)



3000X

FIG.13 Fractography of rotating beam specimen A43 (3000x)

The fractography reported here was performed
by Dr. Nathan R. Katz and his associates
U.S. Army Material Technology Laboratory, Watertown,MA.

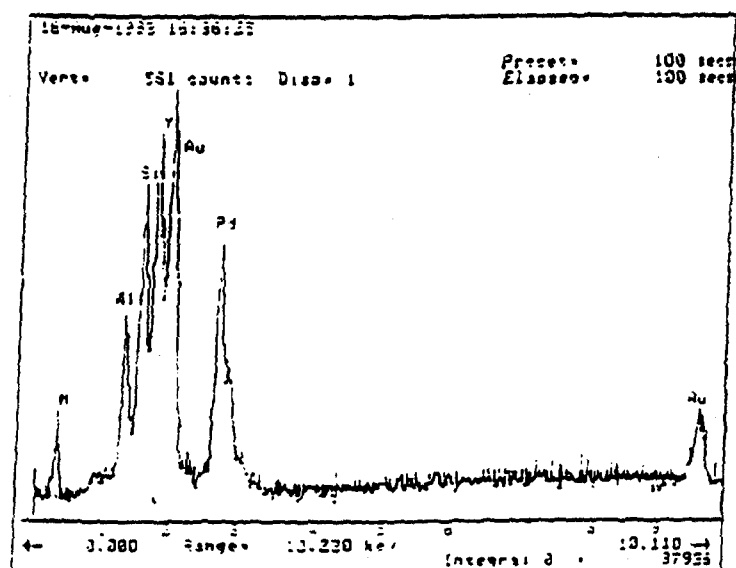
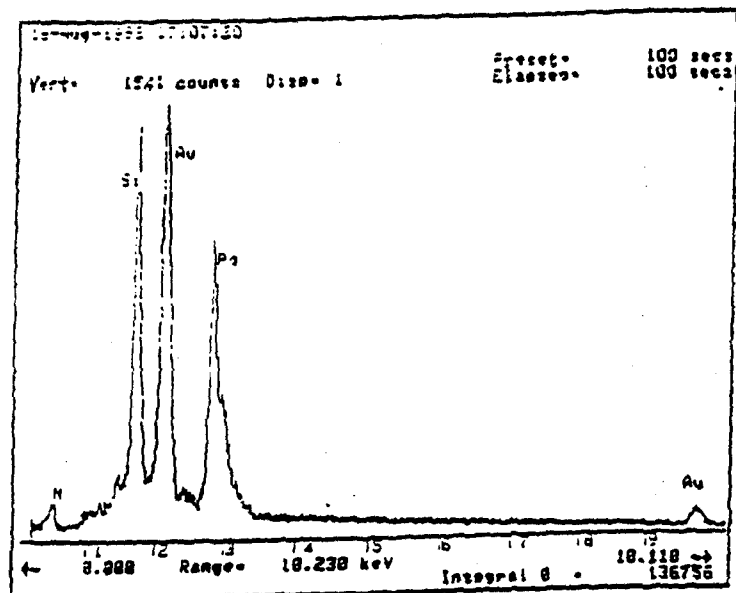


FIG.14 EDX result of rotating beam specimen A43

In comparing the above flaw with those in other failed specimens examined under stereo-microscope, the flaw in this specimen (A43) may be the worst case for all the Toshiba TSN-03H specimens tested.

2.4.2 Fractography of NBD-200 Specimens

Several failed NBD-200 specimens were examined using stereo-microscope. The identifiable failure origins appeared to be volume flaws. The results of the examinations for three failed specimens are described below:

The first NBD-200 specimen examined was No. B14, which failed at setup at the lowest bending moment tested, i.e., 55 in-lbs, which corresponded to a maximum stress of 586 MPa. Under stereo-microscope, in the broken sections shown near the perimeter, there was a diamond shape pull out of about 200 microns in width, while in the other half of the broken specimen, there is a deep cavity which was the mirror image of the other half. Fig. 15 shows the photomicrographs of the two halves of the broken section near the perimeter. This large defect was first suspected to be inclusion prior to SEM/EDX examination. The result of the EDX examination for chemical composition is shown in Fig. 16 and shows that the major components were silicon and nitrogen, indicating no foreign metallic inclusions existed in the defect.

Norton/Cerbec, Inc., requested to examine specimen No. B14. Their investigation has confirmed our EDX finding in that the large size material flaw was made of silicon and nitrogen. Furthermore, they found that the boundary of this foreign particle was 'contaminated', such that there was very poor bonding with the bulk matrix. In the course of their examination, they lost the particle, leaving behind a hole in the failed section of specimen B14.

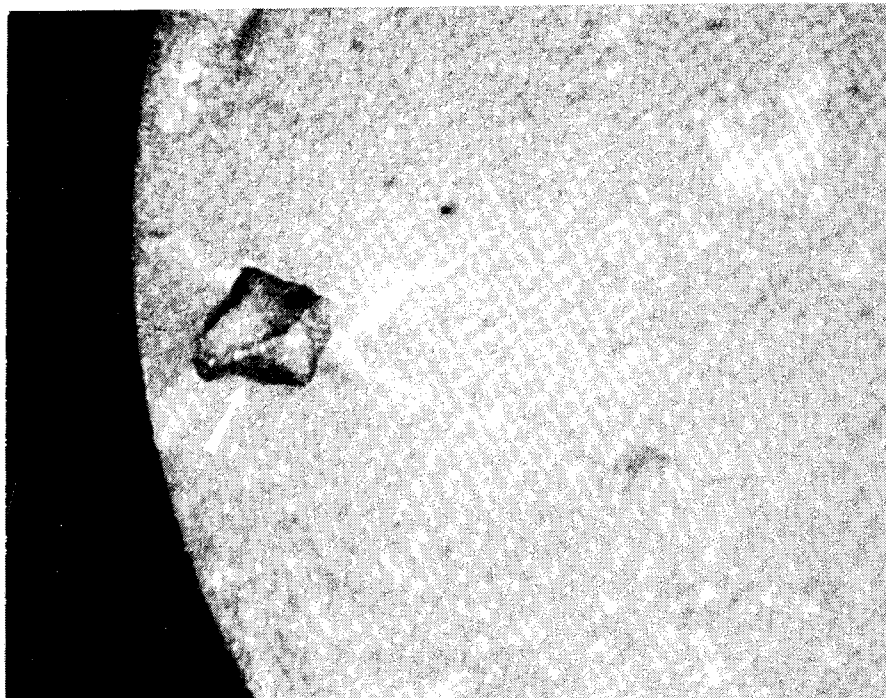


FIG. 15 Fractography of rotating beam specimen B14 (45x).

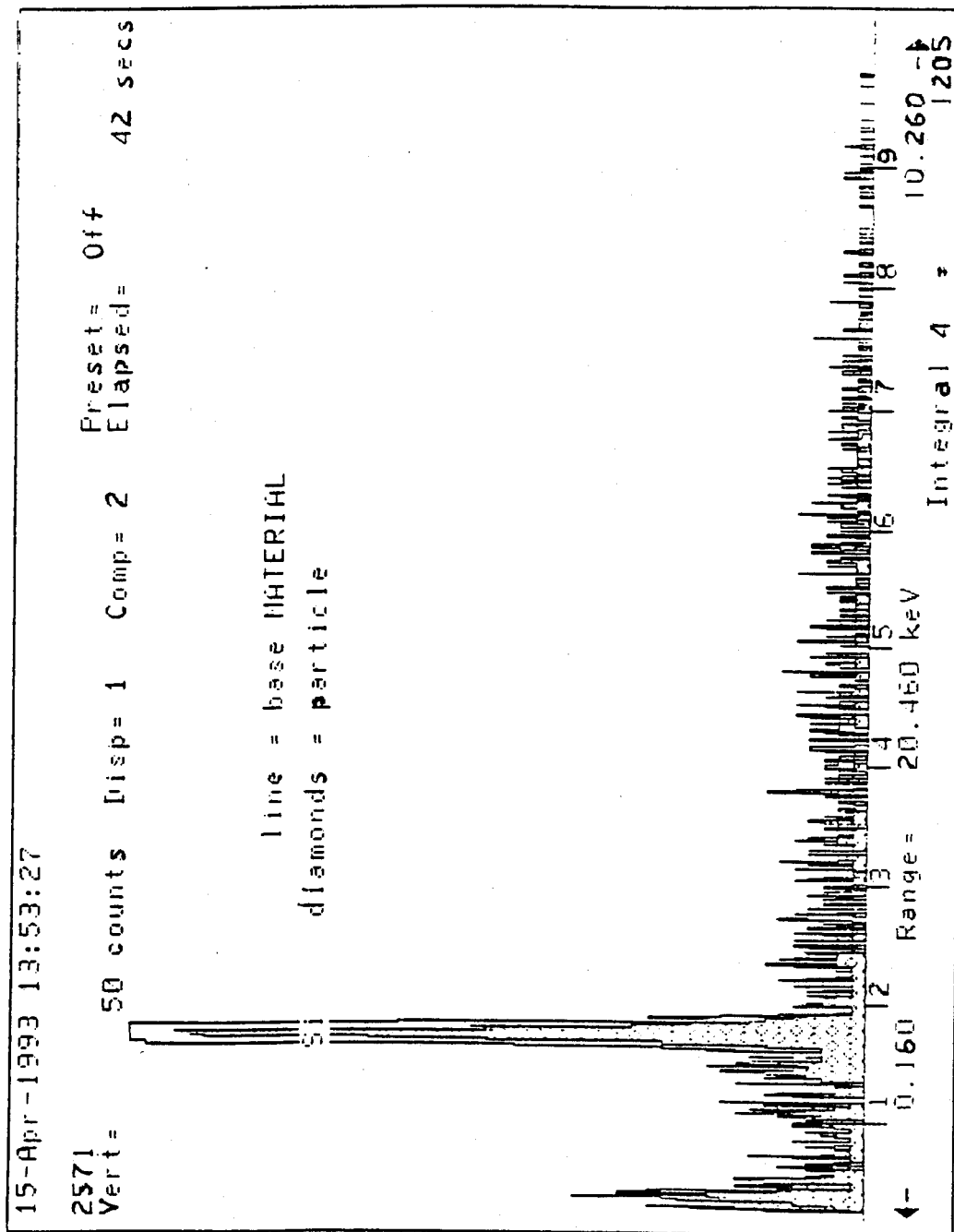


FIG.16 EDX result of rotating beam specimen B14

The second NBD-200 specimen examined was No. B3, which failed by fatigue at relatively low bending load (65 in-lbs or 100 ksi, 690 MPa max. stress). Under the stereo-microscope with 35X magnification, the failure origin appeared to be a smooth flat region near the surface. Fig.17 shows the photomicrograph of this failure origin, marked by white arrows. By comparing the photograph with those published in [19], the failure origin may be a pore seam.

The third NBD-200 specimen examined was No. B4, which failed at 77 in-lbs (or 119 ksi max. stress) with a very short fatigue life of 8200 cycles. Under stereo-microscope, the failed section showed a shiny area of about 300 microns in width near the perimeter. Fig. 18 shows the SEM photomicrograph of the shiny area, marked by white arrows. Fig.19 shows the result of EDX examination, which shows the major chemical components are Si, Al and N. It was therefore judged that the failure origin was an AlN agglomerate which has lower strength than the matrix silicon nitride material.

2.4.3 Further Fractography Study at the University of Florida

A total of 28 fractured rotating beam specimens, 14 for each material, were sent to University of Florida (AFOSR program). Their study showed that most identifiable failure origins in failed specimens were oxide glass, as reported in [21]. However, the failure origin for some of the failed specimens could not be identified because the material around the fracture origin was lost during the fracture. More specifically, only about half of the specimens sent to Florida could have their failure origin identified.

2.5 Assessment of Specimen Surface Finish

Prior to testing, visual examination was made of the finished specimen surfaces, using a low power microscope. The quality of each of the specimens was compared with that of two sample specimens provided by the finisher. Table 4 tabulates the distribution of the number of specimens which broke in setup and the total number of specimens versus the 'rating' of surface finish qualitatively determined based on the examinations. The tabulation shows that the number of specimens broken in setup did not depend strongly on the surface finish ratings inasmuch as the specimens were finished by one well-known finisher.

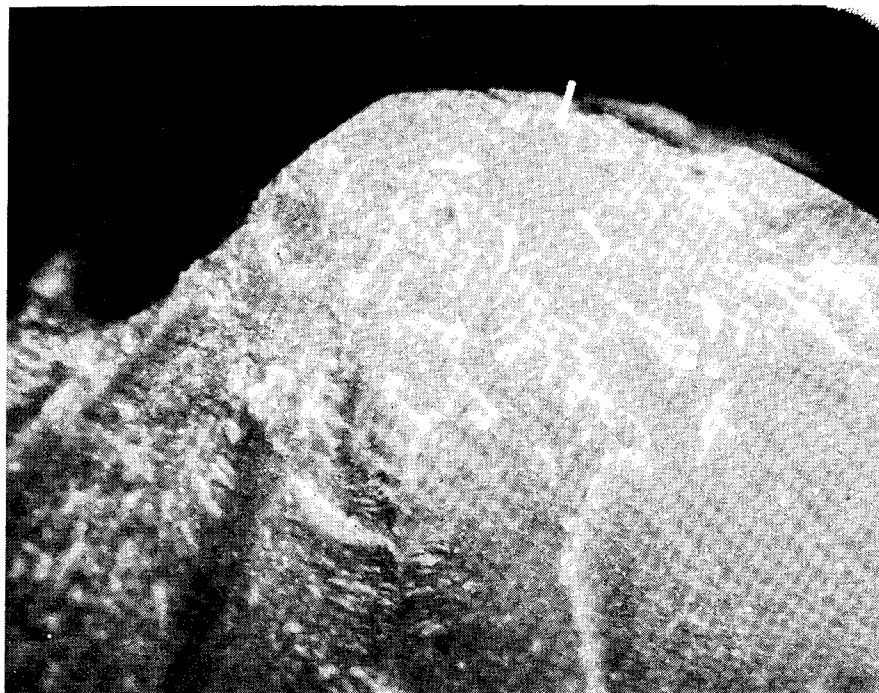


FIG. 17 Fractography of rotating beam specimen B3 (35x)

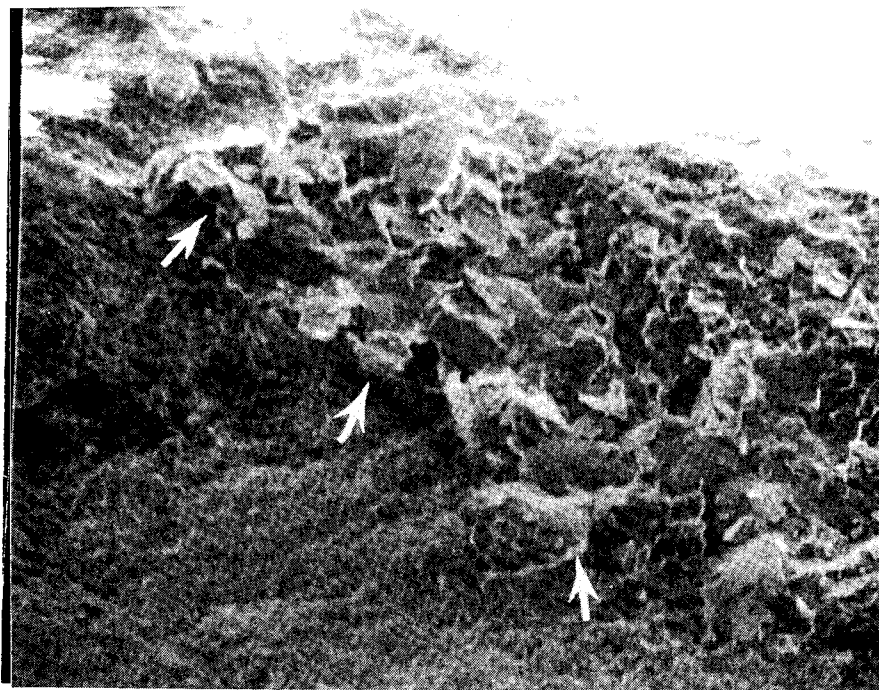


FIG. 18 Fractography of rotating beam specimen B4 (830x)

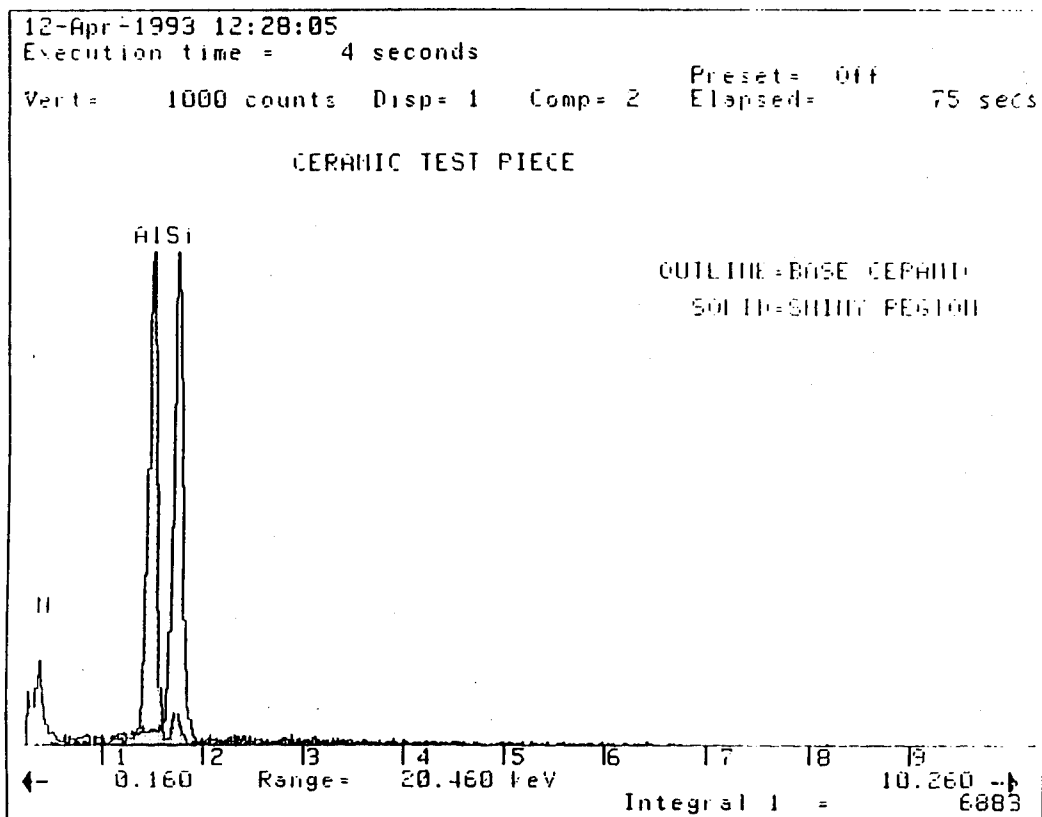


FIG.19 EDX result of rotating beam specimen B4

Table 4

**Distribution of Fast Fracture Specimen Number/Total Number
As a function of Material type and Finish**

Group	Finish of Group	TSN-03H	NBD-200
1	Very smooth	3 / 12	3 / 16
2	Smooth	2 / 42	2 / 31
3	Marginal	2 / 4	2 / 13
4	Slightly scratchy	0 / 4	0 / 0
0	All mixed	7 / 62	7 / 60

Surface profile measurements were made on sample specimens in the longitudinal direction using Taylor-Hobson instruments. The surface roughness was found to have an Ra value of 4.49 microinches and a peak-to-valley value of 44.83 microinches.

Since the specimens were finished in the longitudinal direction with axial lay, it was more meaningful to measure the profile in the circumferential direction. An unused specimen (A71) was recently measured at the gage section in the circumferential direction. The result for the roughness mode showed that the Ra value was $0.4\ \mu\text{m}$ (16.21 microinches), the skew was -.1, and the peak to valley value was $1.9\ \mu\text{m}$ (86.47 microinches). For the unfiltered mode, the Ra value was $0.55\ \mu\text{m}$ (22.25 microinches), the skew was -.8, and the peak to valley was $3.55\ \mu\text{m}$ (142.58 microinches).

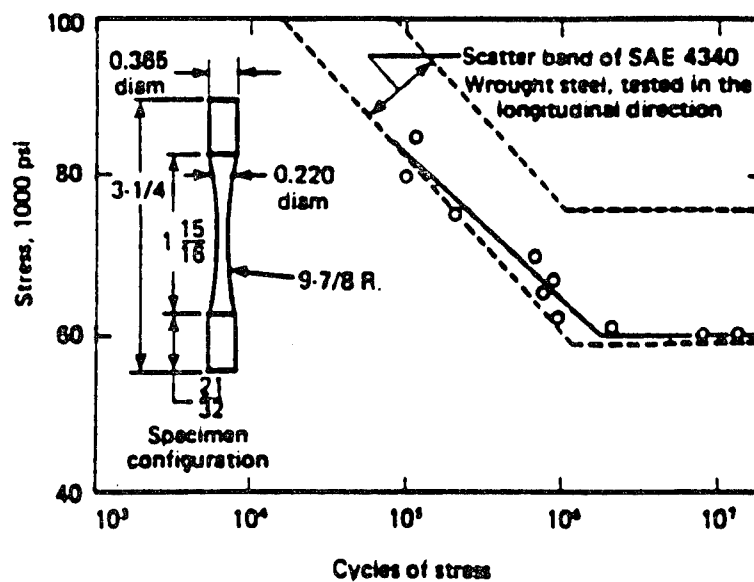
2.6 Comparison of RBF Test Results of HPSN, Steels and Sintered Si_3N_4

In order to answer the question, i.e., how does the fatigue strength of these two hot-pressed silicon nitrides (HPSN) compare with that of hardened bearing steels?, the following comparison was made based on the rotating beam test data of the two HPSN's in this project and those of steels reported in literature.

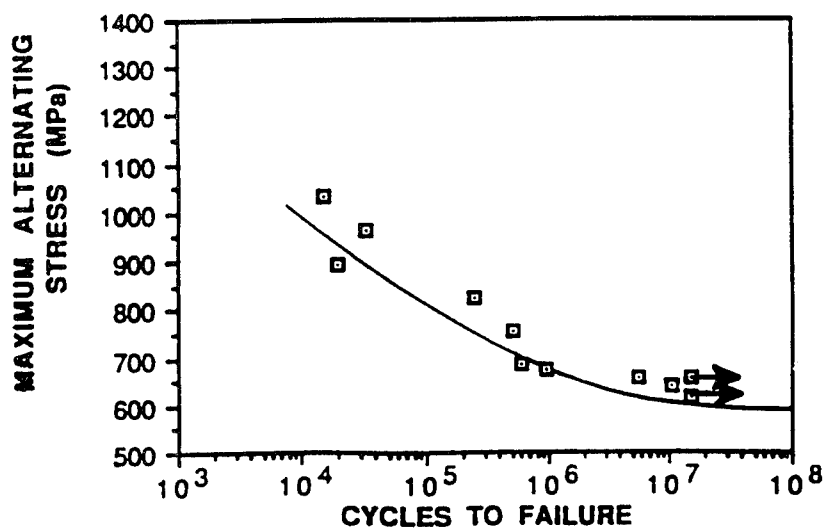
It is well known that the rotating beam fatigue test often has been used in the evaluation of fatigue strength of steels. Fig. 20, taken from published literature [22,23], shows the stress-cycle (S-N) relationships in the rotating beam fatigue test for two types of steels, i.e., an SAE-4340 steel of moderate hardness, i.e., HRC-33, reported in [22], and a 4680 P/M steel at high hardness, HRC 58-59 [23].

Figure 21 shows the comparison of the two HPSN's in the present program, with the two curves for the above mentioned steels as well as the sintered silicon nitride obtained by Ko [11]. The two plots in Fig. 21 show, with the exception of the fast fracture data, that most of the data for HPSN lie above the curve for 4340 steel, but lie around the curve for 4680 P/M steel of bearing hardness. In addition, the fatigue strength of the HPSN was more than two times higher than the sintered Si_3N_4 data published in 1987.

The results show that the fatigue strength of the two HPSN's tested in this project was equal or superior to the room temperature fatigue strength of hardened bearing steels. In the case of stationary loading, the strength of the two HPSN suffered reduction due to the fast fracture property, which was predictable from the MOR bending test of the silicon nitride ceramics.



R. R. Moore fatigue curve for P/M-forged 4640 steel hardened and tempered to 33 HRC and a yield strength of 138,000 psi.



S-N curve for RBF test results of fully dense 4680 P/M at HRC 58-59.

FIG.20 S-N Plots for Rotating beam tests of two P/M Steels.

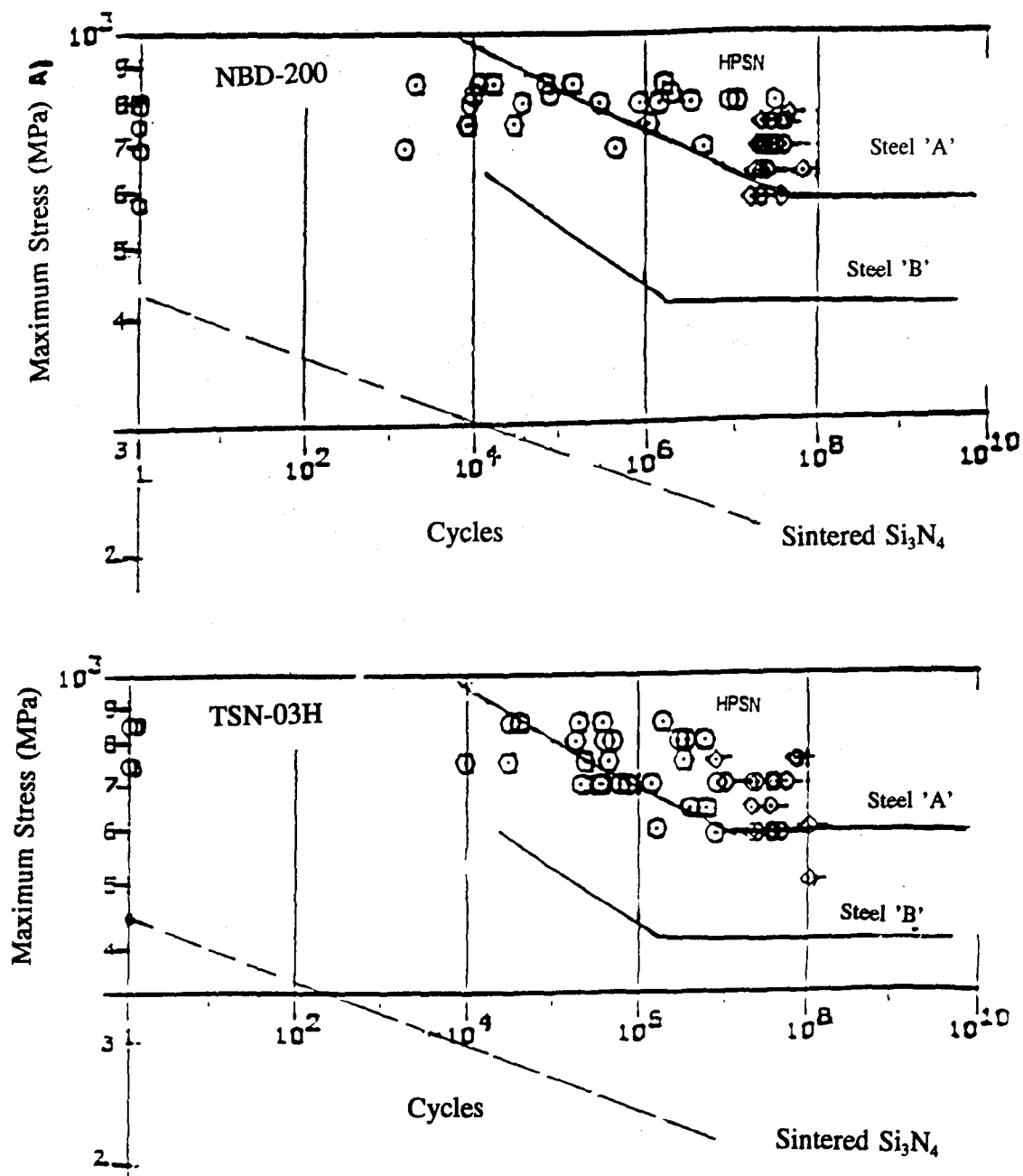


FIG. 21 Rotating Beam Fatigue Test Result for Two HPSN Ceramics (data points: \odot for fracture and \diamond for runout or suspension) and S-N Curves for Sintered Si_3N_4 [6] and two hardened P/M steels with hardnesses Rc 58-59 for Steel 'A' and Rc 33 for Steel 'B'.

3. DATA ANALYSIS AND RELIABILITY THEORY

Statistical method as well as reliability theory for ceramics are important tools to analyze the failure data and to characterize the material properties. The rotating beam test data showed that at low or moderate loads, runout or suspension at a large number of test cycles was a major mode of test completion. Fortunately, the currently available Weibull statistical methods, such as the maximum likelihood analysis, can adequately take the suspension data points into account. The well-known Weibull analysis computer software, such as Weibull-Smith and those in [24] by Abernethy were useful in treating the data.

3.1 Weibull Plots for Lives at Constant Load

Figures 22-26 contain Weibull plots of RBF test fatigue lives for the two materials at constant values of maximum bending stress at the outer surface of the neck of the RBF specimens. These plots were obtained using the Weibull-Smith computer software. The use of Weibull software to treat the data at constant load was inadequate at low maximum stress level, at which the number of suspensions was large and the number of failures was very low.

3.2 Median Life Calculation

The first method used a conventional approach, which was to calculate the median life (at 50% probability) for tests run at constant maximum bending stress (σ), using the maximum likelihood method [24]. In this calculation, the runout data were treated as suspensions and the fast fracture data was neglected. A linear regression analysis was then applied to obtain a power law relation between the median life ($N_{0.5}$) and σ , as well as the fatigue exponent (n), i.e.,

$$N_{0.5} \approx \sigma^{-n} \quad (3)$$

Figure 27 plots the variation of median life with the maximum bending stress. For the new specimens tested, the fatigue exponents n were found to be 25.73 and 50.88 for materials "A" and "B" respectively. For the new and survived test specimens, the values of n were 22.14 and 48.10 respectively for "A" and "B".

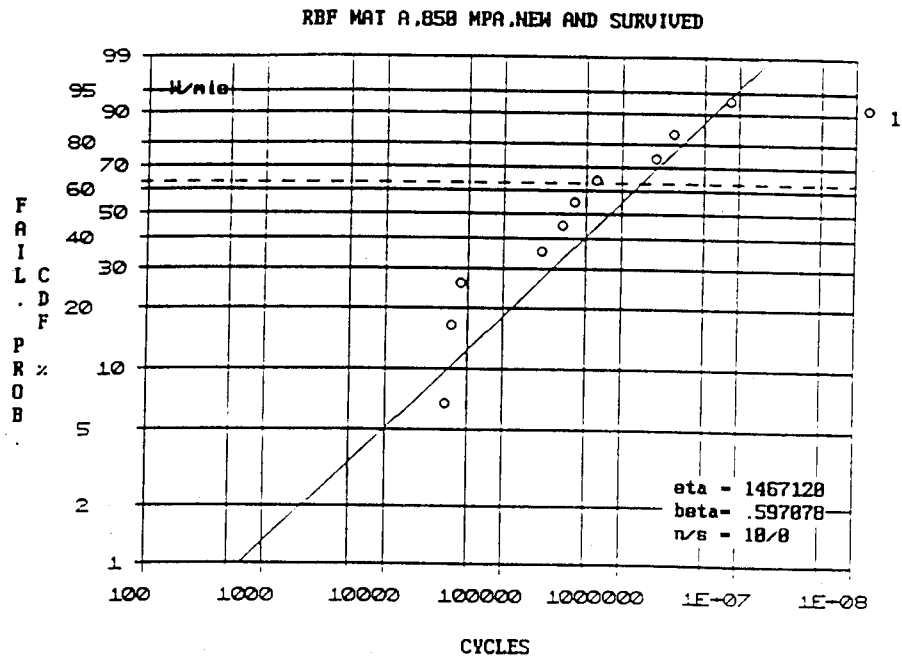


FIG.22 Weibull plot for fatigue life at maximum stress 850 MPa with TSN-03H rotating beam specimens

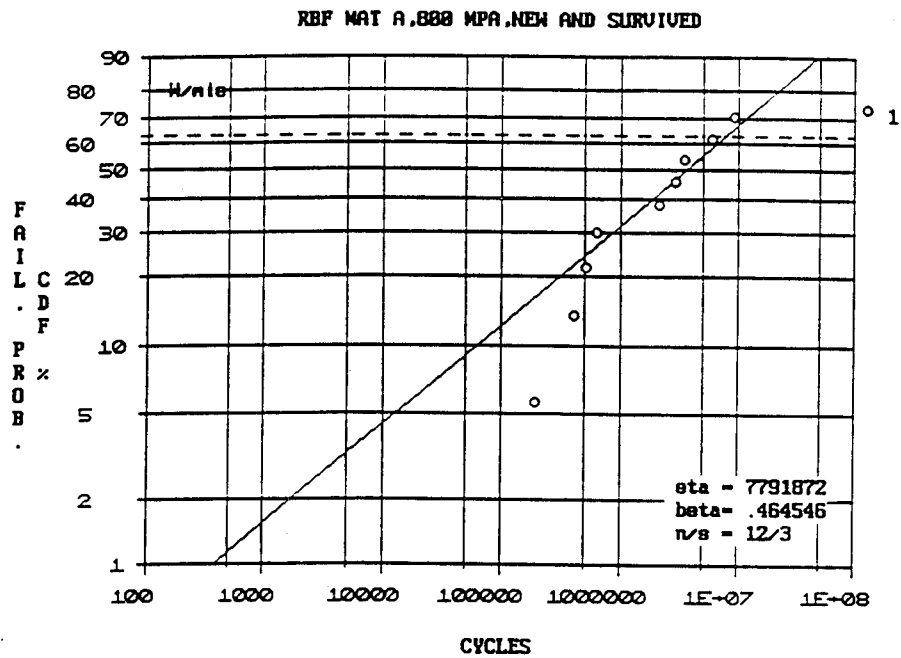


FIG.23 Weibull plot for fatigue life at maximum stress 800 MPa with TSN-03H rotating beam specimens

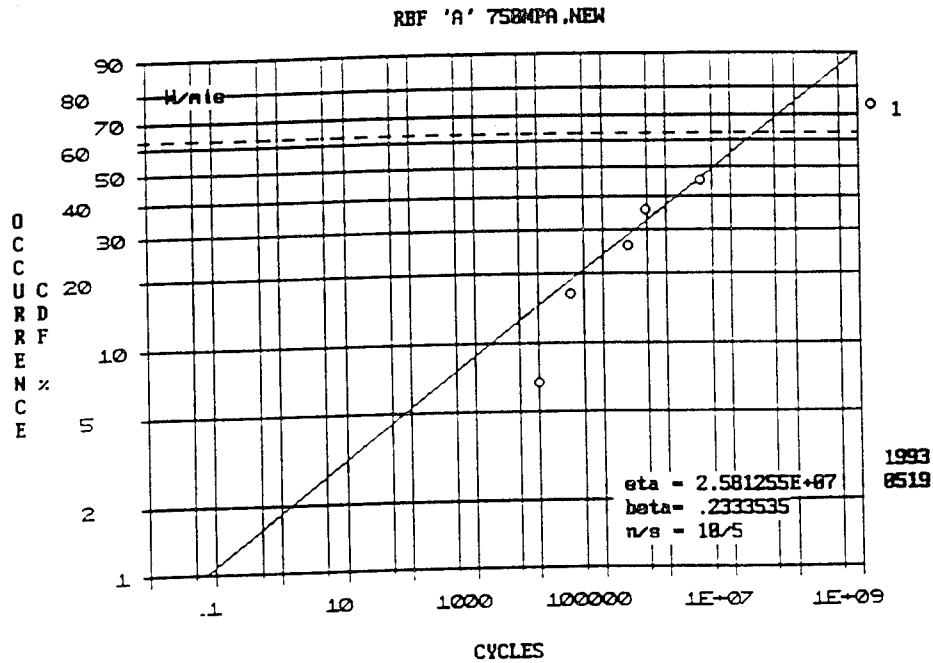


FIG.24 Weibull plot for fatigue life at maximum stress 750 MPa with TSN-03H rotating beam specimens

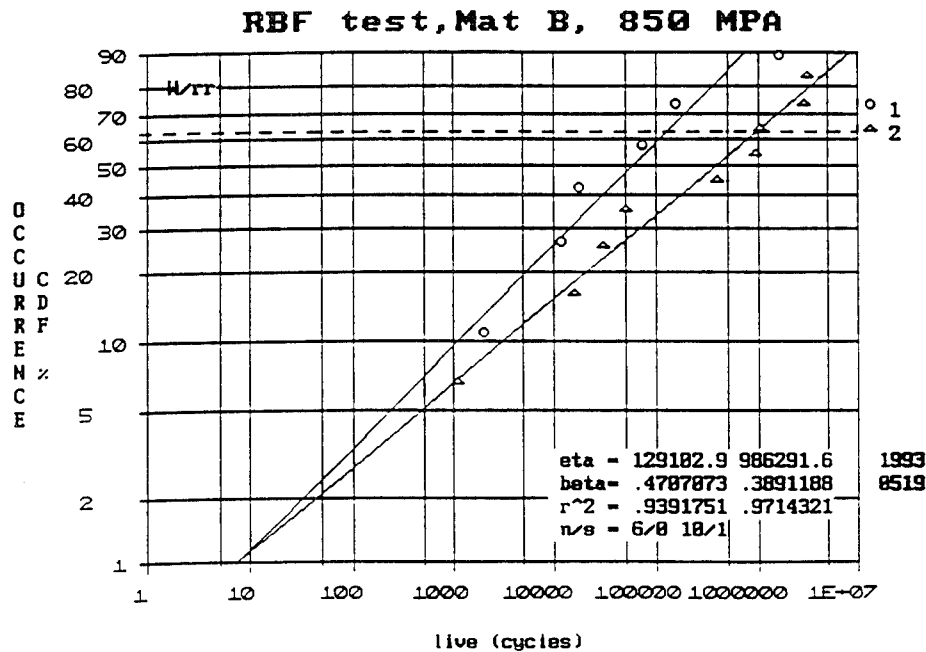


FIG.25 Weibull plot for fatigue life at maximum stress 850 MPa with NBD-200 rotating beam specimens.

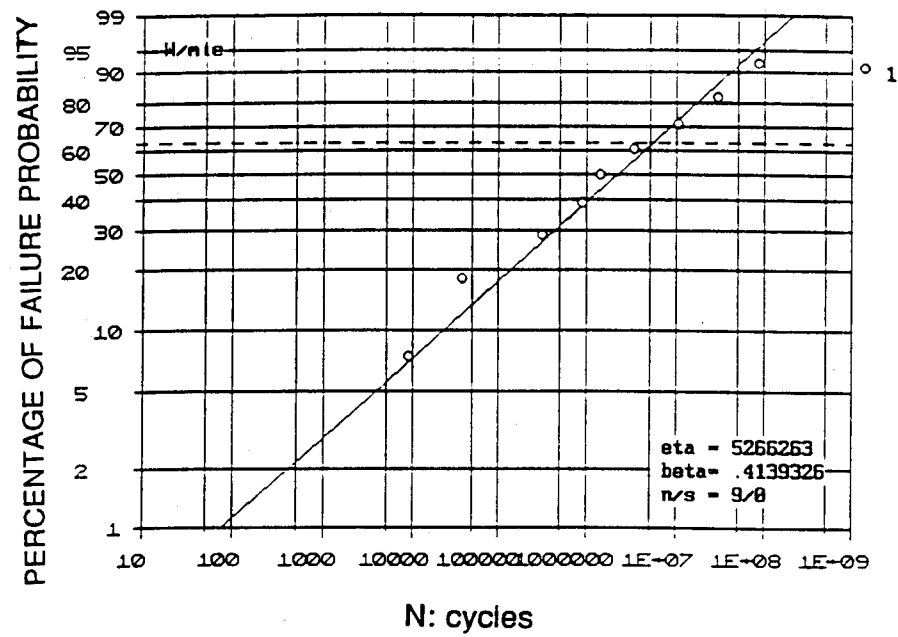


FIG.26 Weibull plot for fatigue life at maximum stress 800 MPa with NBD-200 rotating beam specimens

ROTATING BEAM FATIGUE TEST **VARIATION OF MEDIAN LIFE WITH MAXIMUM STRESS**

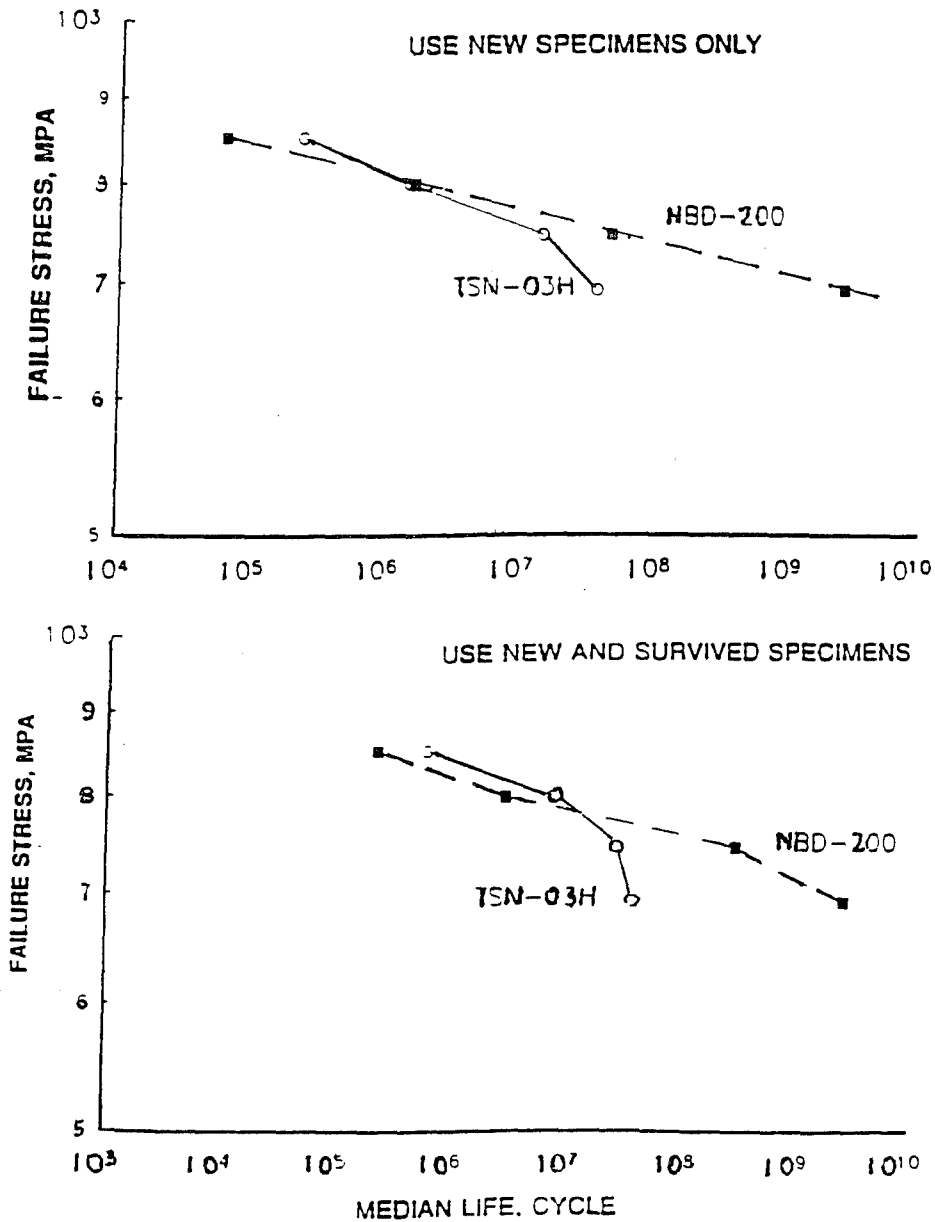


FIG.27 Variation of Median Life with Failure Stress

3.3 Maximum Likelihood Analysis for Multiple Step-Wise Load Test

The second method was an alternative approach, which was to apply the maximum likelihood estimation to all the test data (at different stress levels) at once for a given material to obtain the unknowns n and β in the following formula for the failure probability P_f , i.e.,

$$P_f = 1 - \exp \left[- \left(\sum_{j=1}^J N_j \sigma_j^n / N_o \right)^\beta \right] \quad (4)$$

where J is the number of load steps. This procedure is applicable to test data from tests with both single and multiple levels of loadings. For tests with single load level, $J=1$.

The above formulation is an extension of the previous maximum likelihood analysis by McCool [25] to the cases with $J > 1$. The derivation is given in Appendix B.

3.3.1 Weibull Distribution Plots of Equivalent Life

Figure 28 shows the Weibull plots, for NBD-200 and TSN-03H, the failure probability versus the 'equivalent life' N_e , where $N_e = \sum_{j=1}^J \sigma_j^n N$ for the two materials. In these plots, the unit of N is cycles, the maximum stress σ is in GPa and J is the number of load steps. The summation is taken over the range from 1 to J in the multiple load case. For tests with new specimens only without step-up loading, $J=1$.

Table 5 tabulates, for the two materials, the values of n , β , N_o and the median values of N_e or $\{ \sum_{j=1}^J \sigma_j^n N \}^{0.5}$.

ROTATING BEAM FATIGUE TEST - FAILURE PROBABILITY vs $\sigma^n N$ PLOTS

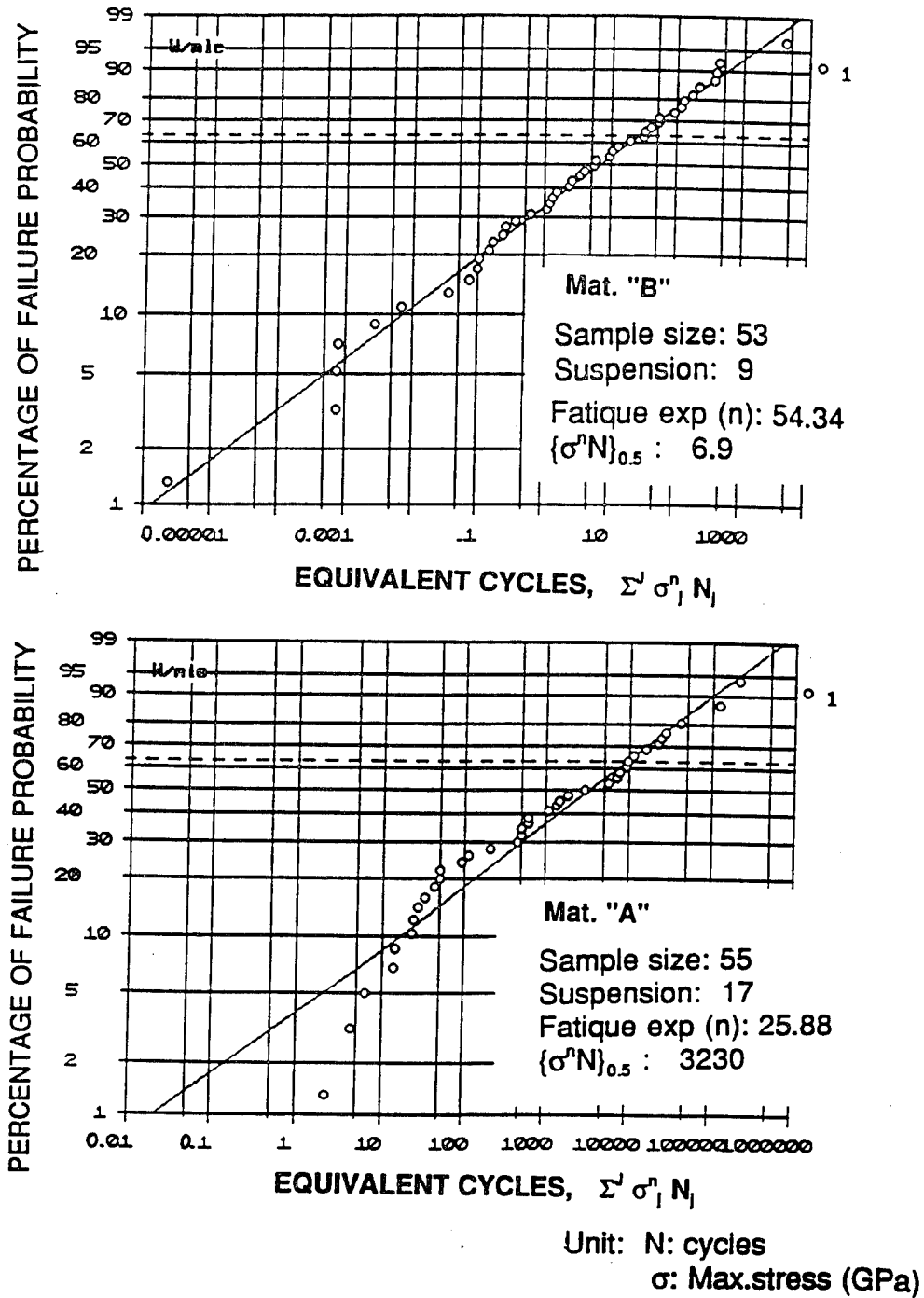


FIG.28 Weibull plots of equivalent cycles for NBD-200 and TSN-03H rotating beam specimens

**Table 5 Fatigue Property Data of the Two Test
Materials Based on Rotating Beam Fatigue (RBF) Testing**

<u>Material</u>	<u>TSN-03H</u>	<u>NBD-200</u>
Sample Size	55	53
Failure No./Runout No.	38/17	44/9
Fatigue Exponent, n	25.88	54.34
Weibull Slope, β	0.355	0.274
Scale Parameter, N_0	9078	14.90
Median Equiv. Life, $(N_e)_{0.5}$	3230	6.9
where $N_e = \sum_{j=1}^J \sigma_j^n N$		

3.4 Effect of Surface Finish on the Fatigue Performance of the RBF Specimens

By visual inspection using a low power microscope, we have classified and documented the surface finish conditions of the rotating beam specimens prior to testing. The ratings consist of 1. very smooth, 2. smooth (sample quality), and 3. marginal smooth. It was of interest to find whether the surface finish rating had any effect on the fatigue performance of the specimens. For the NBD-200 specimens, Figs. 29, 30 and 31 show, for the three different finishes respectively, the Weibull plots of failure probability versus N_e . Table 6 tabulates for RBF tests of NBD-200 specimens the values of the median value of $\Sigma \sigma^n N$ and the slope in the Weibull plot for the three groups of different surface finishes and the mixed group containing all the NBD-200 specimens.

Comparison of Figs. 29 and 30 shows no significant difference of Weibull curves for the super-fine and sample quality (average) surface finishes, while Fig. 31, for the rough specimens, shows a significant increase in Weibull slope.

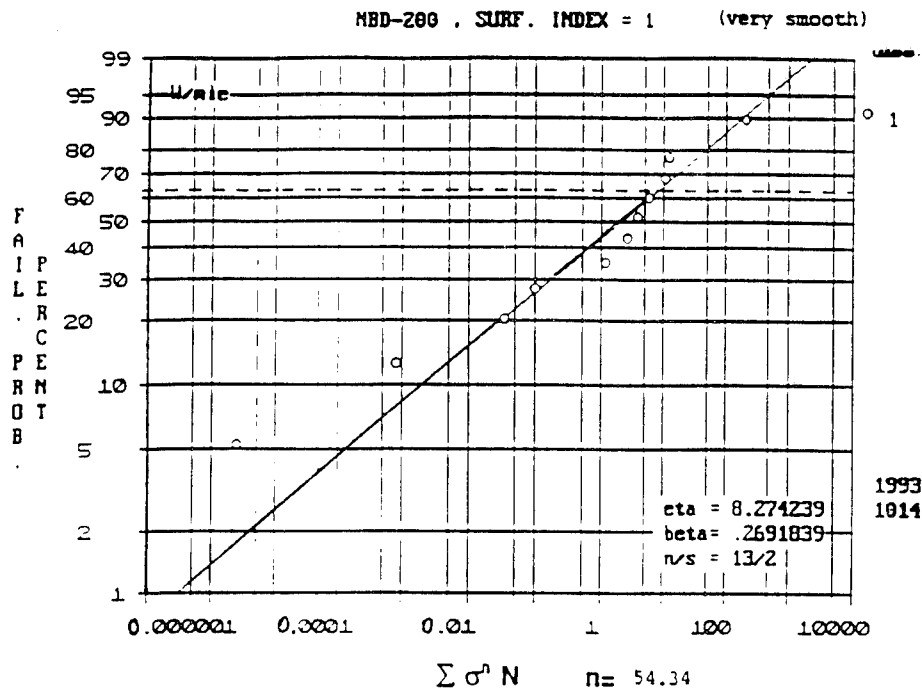


FIG.29 Weibull plot of equivalent cycles for NBD-200 rotating beam specimen with 'very smooth surface'

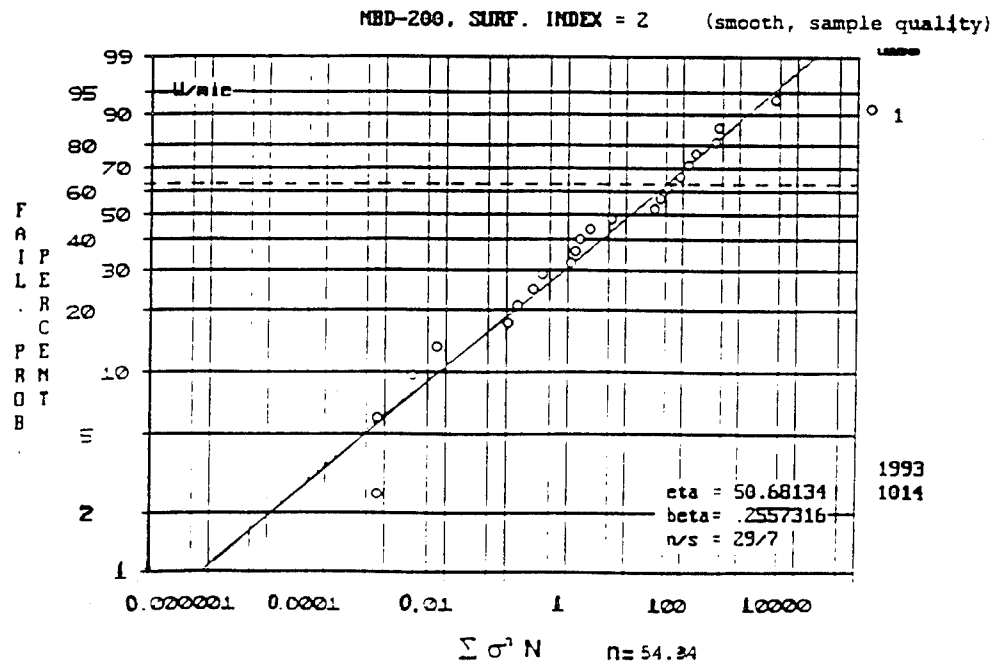


FIG.30 Weibull plot of equivalent cycles for NBD-200 rotating beam specimen with 'smooth' surface

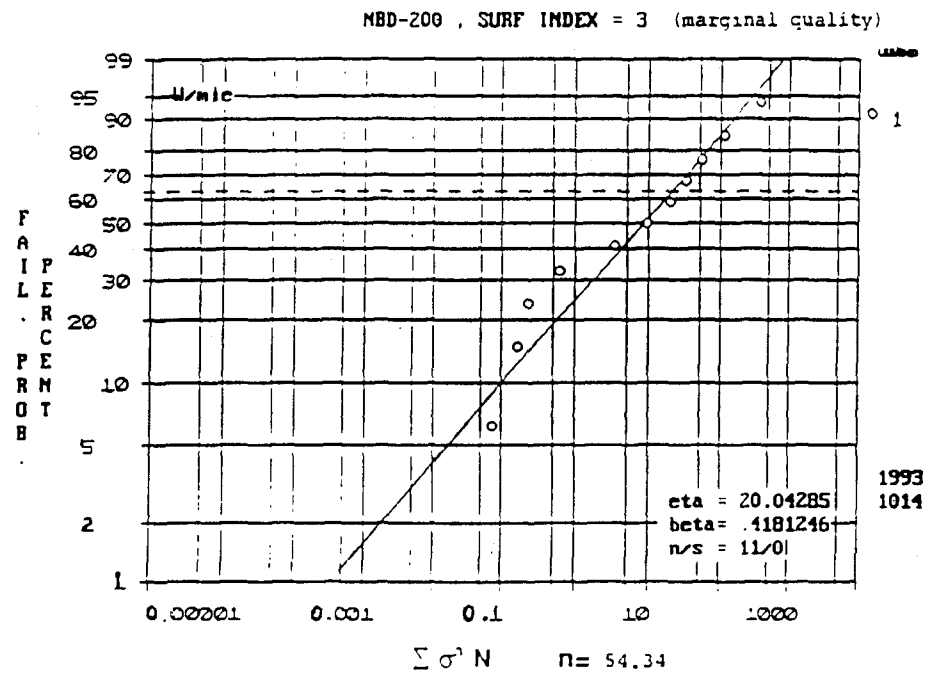


FIG.31 Weibull plot of equivalent cycles for NBD-200 rotating beam specimen with 'marginal' finish

Table 6

Tabulation of Median and Slope β
RBF Test Material: NBD-200

	Finish of Group	Sample no.	Suspension no.	Median $\Sigma\sigma^2N$	Slope	Rms Roughness
0	mixed	53	9	6.9	0.274	0.2-0.7
1	very smooth	13	2	2.5	0.269	≈ 0.2
2	smooth	29	7	15	0.256	≈ 0.4
3	marginal	11	0	9	0.418	≈ 0.6

3.5 Reliability Formulation with Volume Flaw Assumption

3.5.1 Fast Fracture

First for fast fracture, the failure probability of a component is an exponential function of a volume integration of stress (σ) to the power of the Weibull modulus m , i.e.,

$$\begin{aligned} P_f &= 1 - \exp \left[- \int (\sigma/\sigma_o)^m dV \right] \\ &= 1 - \exp \left[-V_{\text{eff}} \sigma_{\text{max}}^m / \sigma_o^m \right] \end{aligned} \quad (5)$$

where V_{eff} is the effective stress volume, defined by

$$V_{\text{eff}} = \int (\sigma/\sigma_{\text{max}})^m dV \quad (6)$$

The formulations and result of the calculation of V_{eff} for the present RBF specimens is given in Appendix C.

For the two baseline ceramics, values of m and σ_o have been presented in Table 7, and were calculated from the Weibull plots in Fig. 2, based on the MOR bending data using 3-pt bending tests (TSN-03H) and 4-pt bending tests (NBD-200).

Alternatively, the Batdorf theory [26,27] can be applied as in [31], which results in a new scale parameter $\sigma_{b,o}$ where the subscript b denotes Batdorf, as opposed to "Weibull" in the above formulation. For the Batdorf theory, eq(1) has the following form:

$$P_f = 1 - \exp \left\{ - \int_v \left[\int_o (\Omega/4\pi) dn_v(\sigma_{\text{cr}}/d\sigma_{\text{cr}}) dV \right] \right\} \quad (7)$$

where Ω is the area of the solid angle projected onto a unit radius sphere in principal stress space containing all of the crack orientation for which the effective stress is greater than or equal to the critical stress σ_{cr} . In [28], Chao and Shetty found that for silicon nitride, fracture initiating cracks nucleated at pores and oriented perpendicular to the maximum principal stress direction during loading. Therefore, the orientation factor $\Omega/4\pi$ can be set equal to unity for both uniaxial and biaxial loadings. With this important simplification, eq(7) can be reduced to eq.(5).

Table 7

SUMMARY OF MATERIAL PROPERTIES FOR THE TWO TEST MATERIALS**(for volume flaws)**

Material Type	Unit	Toshiba	Cerbec
Cyclic Fatigue -			
Fatigue Exponent (n)		25.88	54.34
Weibull slope (β)		0.355	0.274
Median Value $\{\sigma^n N\}_{0.50}$		3230	6.9
N_0		9078	14.9
Crack Growth Parameter (B_w)	MPa ² cycles	4.33×10^{12}	20.3×10^{12}
Fast Fracture -			
Method of Testing		3-pt bending	4-pt bending
Characteristic Strength σ_θ	MPa	1050	900
Effective volume, $V_{\text{eff,MOR}}$	mm ³	1.602	12.26
$V_{\text{eff,RBF}}$	mm ³	40	44
Weibull Modulus (m)		10.27	9.7
Scale Parameter σ_0	MPa	1098	1154

3.5.2 Cyclic Fatigue

Crack growth measurement for silicon nitride by H. Kobayashi [29] shows that the crack growth rate (da/dN) is governed by $K_{I,max}$ rather than its range, i.e., $\Delta K_{I,max}$ (as in the Paris' law). Thus the crack growth rate may be approximated by a power function of the equivalent Mode I maximum stress intensity factor $K_{I,max}$, i.e.,

$$da/dN = C K_{I,max}^n, \quad K_{I,max} = Y\sigma\sqrt{a} \quad (8)$$

where Y is a constant related to crack geometry. For penny-shaped cracks, $Y=2/\sqrt{\pi}$. C and n are material constants, which are called "crack growth parameter" and "fatigue exponent" respectively.

The above assumption is based on the recent measurement of crack growth in silicon nitride by Kobayashi et al. [29].

Following [30], the integration of the above formula with respect to the cycle N results in the following formula, for volume flaw analysis, for the probability of fracture (or macrocracking) after subcritical crack growth,

$$P_f = 1 - \exp\left[- \sigma_o^{-m} \int \sigma^m (1 + \sigma^2 N/B)^{m/(n-2)} dV \right] \quad (9)$$

$$B = \frac{2}{CY^2 (n-2) K_{Ic}^{n-2}} \quad (9a)$$

As suggested by Nemath et al. [31], the constant B in the above formula can be obtained from the cyclic fatigue test under uniaxial stress, such as the rotating beam fatigue test, if the value of the fatigue exponent and the mean value $\{\sigma^n N\}_{0.5}$ is known. (Note the subscript 0.5 denotes 50% probability, or the 'mean value')

For the case $P_f = 0.5$ and $\sigma^n N \gg B$, the above equation for P_f is reduced to

$$B = \{\sigma^n N\}_{0.5} \sigma_o^{2-n} [-V_{eff,RBF}/\ln(1-0.5)]^{(n-2)/m} \quad (10)$$

where m is the Weibull modulus, σ_0 is the scale parameter and $V_{\text{eff,RBF}}$ denotes the effective stress volume of the RBF specimen (a function of m), which has been formulated and computed in Appendix C.

Table 7 tabulated the various constants for the two materials. Note that the Weibull modulus (m) was based on the MOR test data (see Fig.2) obtained from the two suppliers. The fracture toughness values were also from the supplier, although a recent indentation test of the two silicon nitride materials [21] shows somewhat different values of fracture toughness of the two materials.

3.6 Rolling Element Under Contact Load of Multiple Stress Levels

Particular interest was focused on the material elements subject to multiple levels of contact loadings between the ball and raceways. In the tensile test and rotating beam fatigue test of the ceramic material, the applied maximum tensile stress in each stress cycle was a constant. In the RCF test of ceramic rods which were in contact with three steel balls, the contact load and stress in each of the ball-rod contacts was considered to be identical. Therefore, the maximum tensile stress in each stress cycle was constant.

In the case of ball bearings, the ball surfaces were subject to multiple levels of loadings, such as that from the inner ring contact and that from the outer ring contact, if the contact angles are equal.

3.6.1 Theory of Subcritical Crack Growth under Multiple Loadings

A modified formulation of failure probability in terms of crack growth with cyclic loading of multiple stress levels is given as follows as an extension of the previously given subcritical crack analysis for cyclic loading.

For the case of multiple loads, the crack is subject to different levels of stress intensity factor, i.e.,

$$\begin{aligned} \frac{da}{dN} &= C \sum K_{I,k}^n \\ &= C Y^{n/2} a^{n/2} \sum \sigma_k^n \end{aligned} \quad (11)$$

where k is the index for a stress level and σ_k is the stress at the k -th level. Integration of the above equation results in

$$\begin{aligned} da/a^{n/2} &= C Y^{n/2} \sum \sigma_k^n dN \\ -2/(n-2) a^{-(n-2)/2} &= C Y^{n/2} \sum \sigma_k^n N_k \end{aligned} \quad (12)$$

where N_k is the number of stress cycles at the stress level σ_k . Following an analysis given in [30], the limit of integration on the left side of the above equation is from a_a to a_f , where a_a and a_f represent the critical crack length at the beginning of the loading and at failure respectively. Note that these limits can be related to the maximum stress values:

$$a_a = [K_{Ic} / Y \sigma_{a,max}]^2, \quad a_f = [K_{Ic} / Y \sigma_{f,max}]^2 \quad (13)$$

where the subscript max denotes the maximum value of the stress levels σ_k applied.

The following equation is obtained:

$$(\sigma_{a,max})^{n-2} - (\sigma_{f,max})^{n-2} = 1/B \sum \sigma_{k,n}^n N_{k,n} \quad (14)$$

where B is given in Eq.(9a).

Note the failure probability in the case of fast fracture is given by

$$P_f = 1 - \exp \left[- \int (\sigma_{a,max} / \sigma_0)^m dV \right] \quad (15)$$

where m is the Weibull modulus and σ_0 is the scale parameter.

In the case of cyclic fatigue with multiple loading with different stress levels, the failure probability becomes

$$P_f = 1 - \exp \left\{ - \sigma_o^{-m} \int \left[\sigma_{f,\max}^{n-2} + \sum \sigma_{k,n} N_{k,n} \right]^{m/(n-2)} dV \right\} \quad (16)$$

In most situations, the contact angles at the inner ring and outer ring are not equal. Then the inner ring contact and outer ring contact tend to roll on two separate tracks. In this case, each track is subject to a single level of load. The failure probability is calculated separately for each track and then combined using the following relation to obtain the failure probability of a ball with two tracks:

$$P_{\text{ball}} = 1 - (1-P_{,1})(1-P_{,2}) \quad (17)$$

where $P_{,1}$ and $P_{,2}$ are, respectively the failure probability of material around track 1 and track 2 on the ball respectively.

Numerical calculations have shown, that in the Hertzian contacts, the bulk ceramic materials are under a triaxial state of compression (i.e., all the three principal stresses are negative), except for a narrow band of stress volume around the perimeter of the elliptical contact area in which one of the principal stress components becomes tensile. In the compressive stress field, ceramic failure can also occur as a result of shear stress, under a high magnitude of compression. Current formulations on effective stress take into account the tensile stress, not the compressive stress across the crack plane. It is recalled that previous research by Nemeth and Gyekenyesi of NASA Lewis Center [31] suggests that when the normal stress is compressive, it may be set equal to zero and the shear stress alone contributes to the crack growth. Since the shear stress is zero on the plane perpendicular to the principal stress, any crack growth in the plane normal to the compressive principal stress would be zero. In the Batdorf theory [26,27], penny shaped cracks of random orientations are assumed to simulate the material flaws. In a stress field where all the principle stresses are compressive, the shear stress on the crack plane whose normal does not coincide with the directions of the principal stress is not zero.

4. HYBRID BALL BEARING TESTING AND ANALYSIS

4.1 Hybrid Bearing Test Preparation

Grade 5, 3/8" diameter silicon nitride ceramic balls of nominal size (220 for each material) were finished and purchased from two suppliers: Hoover Precision Products, Inc. for TSN-03H, and Norton/Cerbec Inc. for NBD-200. A total of 55 sets of bearing rings made of 52100 steel and of machine tool quality (ABEC-5 or better) were specially manufactured by the Fafnir Bearing Division to a size required to fit the 206 test rig. The special size is MMW206K4FS649A, which has the inner ring width (23.75 mm or 0.920"), about 50% wider than that of the outer ring (16 mm or 0.6299"). Fig. 32 shows the ring set, the cage and nine ceramic balls used in each bearing.

Forty-eight hybrid ceramic 206 ball bearings were fabricated with nylon cages and ceramic balls of the two kinds (9 in each bearing). Visual inspection of the ceramic balls and ring sets was made prior to fabrication. Talysurf traces were made on the raceways of four ring sets. The results gave an average inner race surface finish of 1.5 microinch Ra, which is highly satisfactory. Close tolerance was found on the groove radius. The inner ring conformity for the four rings varied from 0.52058 to 0.52186, while the outer ring conformity varied from 0.5193 to 0.5207 (see Appendix D).

Modification of the 206 bearing test rigs was made at The Torrington Company's Bearing Test Laboratory which performed the required endurance tests of hybrid bearings. The modification involved the installation of one new test shaft, six oil jet caps and the I.D. grinding of six housings.

4.2 Analysis of Test Bearing

The bearing ring has 52% inner and outer race conformity and 0.0015" diametral clearance. Calculations using a computer program developed by Jones [32] were made for the test hybrid bearing as shown in Table 8. The maximum ball load was found to be 579.6 lbs. The maximum contact stress at the most heavily loaded ball was found to be 515.2 ksi (3.55 GPa).

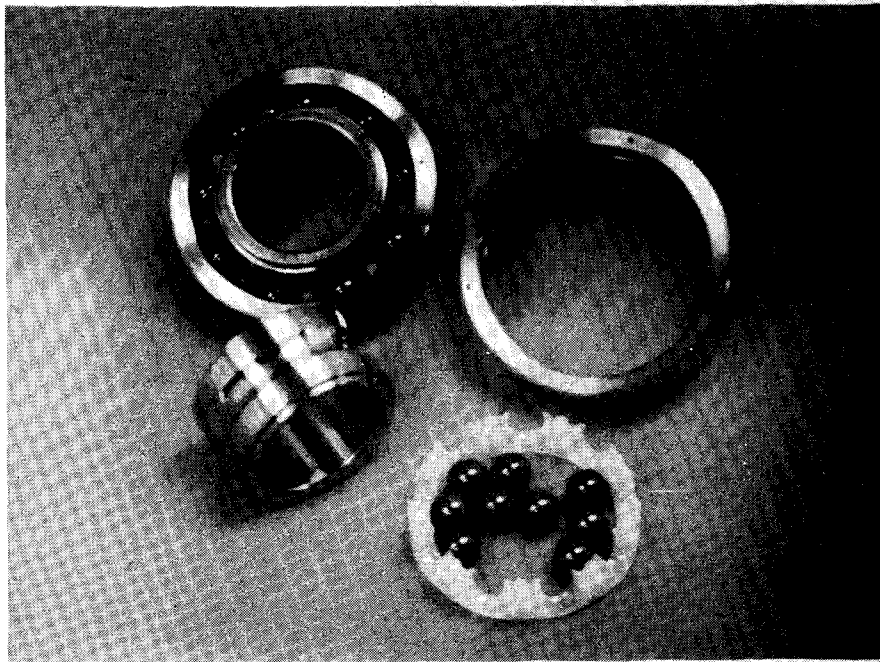


FIG. 32 Components of Hybrid Test Ball Bearing

Table 8

Input Data and Result of 206 Bearing Analysis

Ball Number:	9
Ball Diameter:	0.375: (9.525 mm)
Pitch diameter:	1.820 in. (46,228 mm)
Race Conformity:	0.52 (inner)
	0.52 (outer)
Diametral Clearance:	.0015 in. (0.038 mm)
Bearing Radial Load:	1175 lbs (5226.4 N)
Bearing Speed:	3000 rpm
Young modulus (ball)	45000000 psi (310 GPa)
Poisson ratio (ball)	0.26

Results:

Maximum Ball Load: 579.6 lbs (2578 N)

Maximum Contact stress:

ball-inner race: 515.2 ksi (3.55 GPa)

ball-outer race: 426.1 ksi (2.94 GPa)

Lundberg-Palmgren Life: 31.5 Hours (10% failure probability)

at the inner race contact and 426.1 ksi (or 2.938 GPa) at the outer race contact. The above calculation took into account the elastic modulus of the silicon nitride ball, i.e. Young's modulus of 45×10^6 lb per sq. inch and Poisson ratio 0.26. Based on a bearing speed of 3000 rpm and the calculated ball load distribution, an L_{10} life of 99.5 hours was calculated by the computer program. This calculated life did not take into account the elastic modulus of ceramics in the hybrid bearing. The Lundberg Palmgren theory [13] shows that the load capacity of a ball race contact varies with the reduced Young's modulus to the power of 2.1. The fatigue life of a ball bearing varies with the cube of the bearing load. Thus the calculated life was inversely proportional to the reduced Young's modulus to the power of 6.3. Note that the reduced Young's modulus of the hybrid ceramic-steel contact was 1.2 times that of a steel to steel contact. Thus, the calculated life of a hybrid bearing was that of the steel bearings (with the same ball loads and contact geometry) multiplied by a factor of $1/1.2$ to the power of 6.3, or 0.364.

Multiplying the previously calculated life 99.5 hours by the factor 0.364 gives a Lundberg Palmgren fatigue life of 31.5 hours. Recognizing that in the Lundberg Palmgren theory, the probability of ball failure is neglected, this 31.5 hours is the theoretical fatigue life of the bearing rings in the hybrid bearing arrangement.

4.3 Endurance Test of Hybrid Ball Bearings

Three endurance test rigs were used. Each rig was capable of testing two 6206 ball bearings. Tests were completed for eight groups as planned. Each group consisted of six identical hybrid bearings. The sudden-death method was used in the tests, such that if one of the six bearings in each group failed, the test of the group was ended with one failure and five suspensions. The test load was 1175 lbs (radial) for each bearing, and the speed was 3000 rpm. A circulating oil system was used with Mobil DTE extra heavy oil. The oil inlet temperature was 105 deg. F and the bearing O.D. temperature was monitored. The runout time of the test was 1500 test hours (or 270 millions bearing revolutions) if no failure occurred. The maximum test hours were the same as those used by NSK Company in testing 6206 bearings at the same speed in 1987 [33].

Table 9 tabulates the test conditions and test results of the endurance test of 48 hybrid ceramic bearings. The results show one bearing failure for hybrid bearings with NBD-200 balls and four bearing failures in hybrid bearings with TSN-03H balls.

Appendix D is a laboratory test report, which covers the details of the test conditions, test rigs, bearing ring inspection, and the test results of the eight groups of test bearings. The report shows that all the bearing failures were due to ball spalling, not ring failures.

4.4 Hybrid Ball Bearing Failure Analysis

4.4.1 Norton/Cerbec Balls

The failed bearing (No.535-92) was removed from the test rig and disassembled for failure inspection in the test laboratory. It appeared to be certain that the bearing failure initiated from spalls on one ball only. Using a low power microscope, the failure was found to be on one ball with multiple spalls on the ball surface. The surfaces of other balls and the ring raceways showed no spalls. Severe glazing, but no spalls, was found on the raceway track. This wear was believed to be caused by the debris of the spalls on the failed ball after failure. Figures 33 and 34 show the photomicrograph of the two spalls on the failed ball with 16X and 18X magnifications respectively.

The spalled ceramic was been examined using a SEM and EDX analyzer. Digital X-ray mapping was used to obtain a quick overview of the distribution of possible contaminants on the spall surfaces. Two small Mg rich spots were detected on each of the spalls examined. One spot in the large spall was found outside of the spall and another was found just inside the spall edge as shown in the lower photo of Fig.35. The EDX spectrum of the Mg rich feature (2) is shown overlayed on that of the adjacent smooth ball surface of Fig.36. This shows a significant enrichment of Mg and an increase in Fe and O over the smooth area. This fragment appears to have come from another region of the spall and was redeposited in the edge zone. The photo in Fig. 37a shows what appears to be an initiation point of the spall, which has a mirrored area, about 500 microns in diameter.

Table 9

Summary of Hybrid Bearing Tests

BEARING TYPE: MM206K4
 RING MATERIAL: SAE 52100
 MANUFACTURED BY: FAFNIR BEARING DIVISION
 NUMBER OF BALLS: 9
 BALL SUPPLIERS: CERBEC, INC AND HOOVER PRECISION, INC.
 MAXIMUM STRESS : 3.6 GPA (525 KSI)
 TEST SPEED: 3000 RPM
 LUBRICANT: DTE EXTRA HEAVY
 CAGE MATERIAL: NYLON
 RING FINISH, Ra < 0.1 MICRON
 AFBMA L₁₀ LIFE: 31 HRS.

Ball Mat.	Group No.	No.Brg.	No. Failure	Hours	10 ⁶ Per
NBD-200	1	6	0	-1509	-271.6
NBD-200	2	6	1	13.6	2.45
NBD-200	3	6	0	-1511	-272
NBD-200	4	6	0	-1509	-271.6
TSN-03H	1	6	1	173.2	31.2
TSN-03H	2	6	1	183.3	33.0
TSN-03H	3	6	1	50.1	9.0
TSN-03H	4	6	1	142.3	25.6

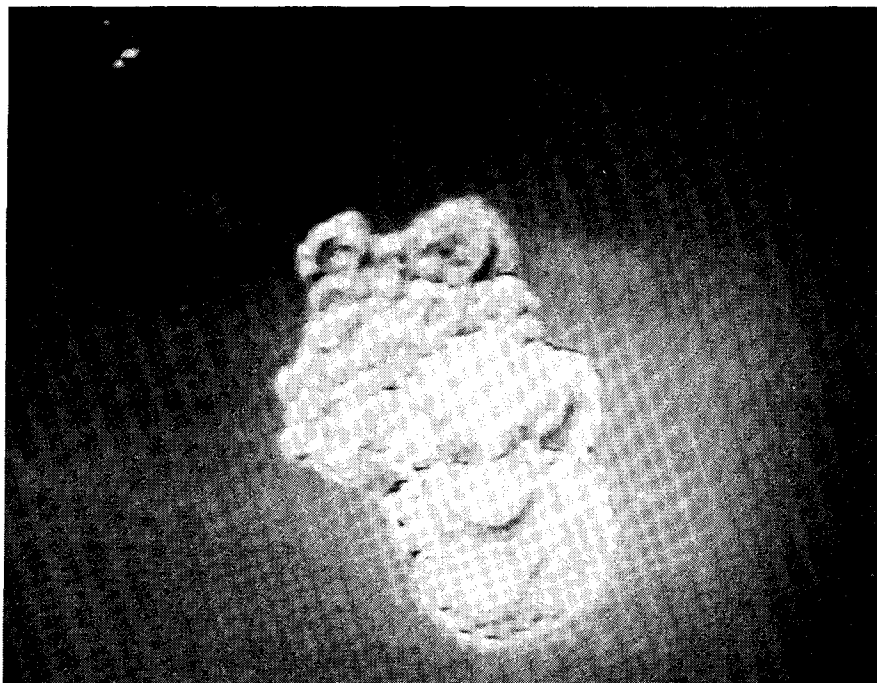


FIG. 33 Photomicrograph of spall on failed NBD-200 ball (bearing No. 535-92)

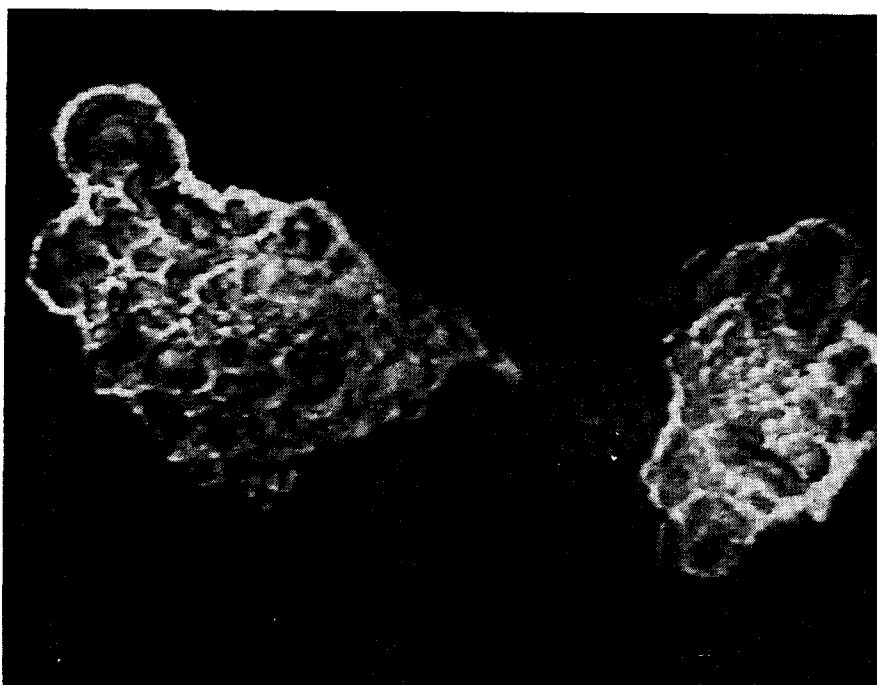


FIG. 34 Photomicrograph of spalls on failed NBD-200 ball (bearing No. 535-92)

SEM Fractography of a Spalled NBD-200 Ball

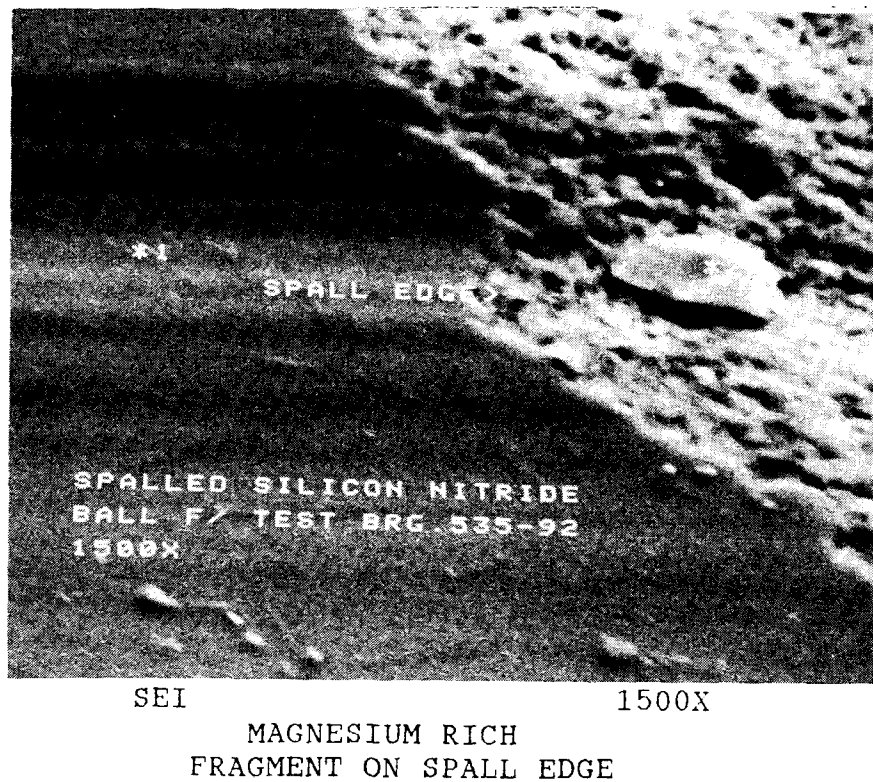
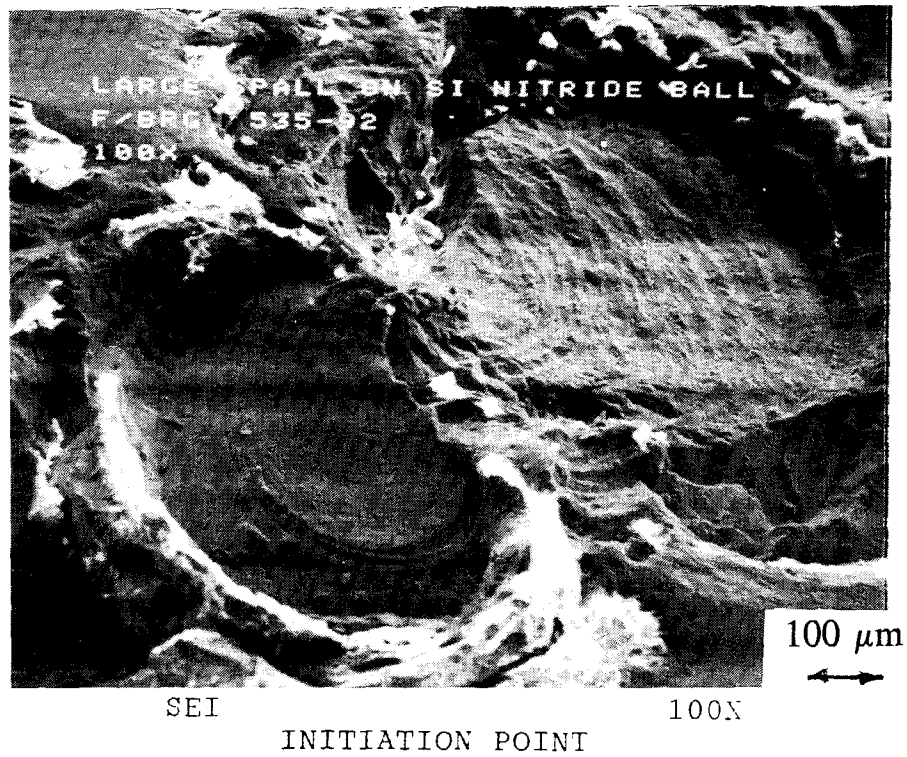


FIG.35 SEM photograph of large spall on a failed NBD-200 ball.

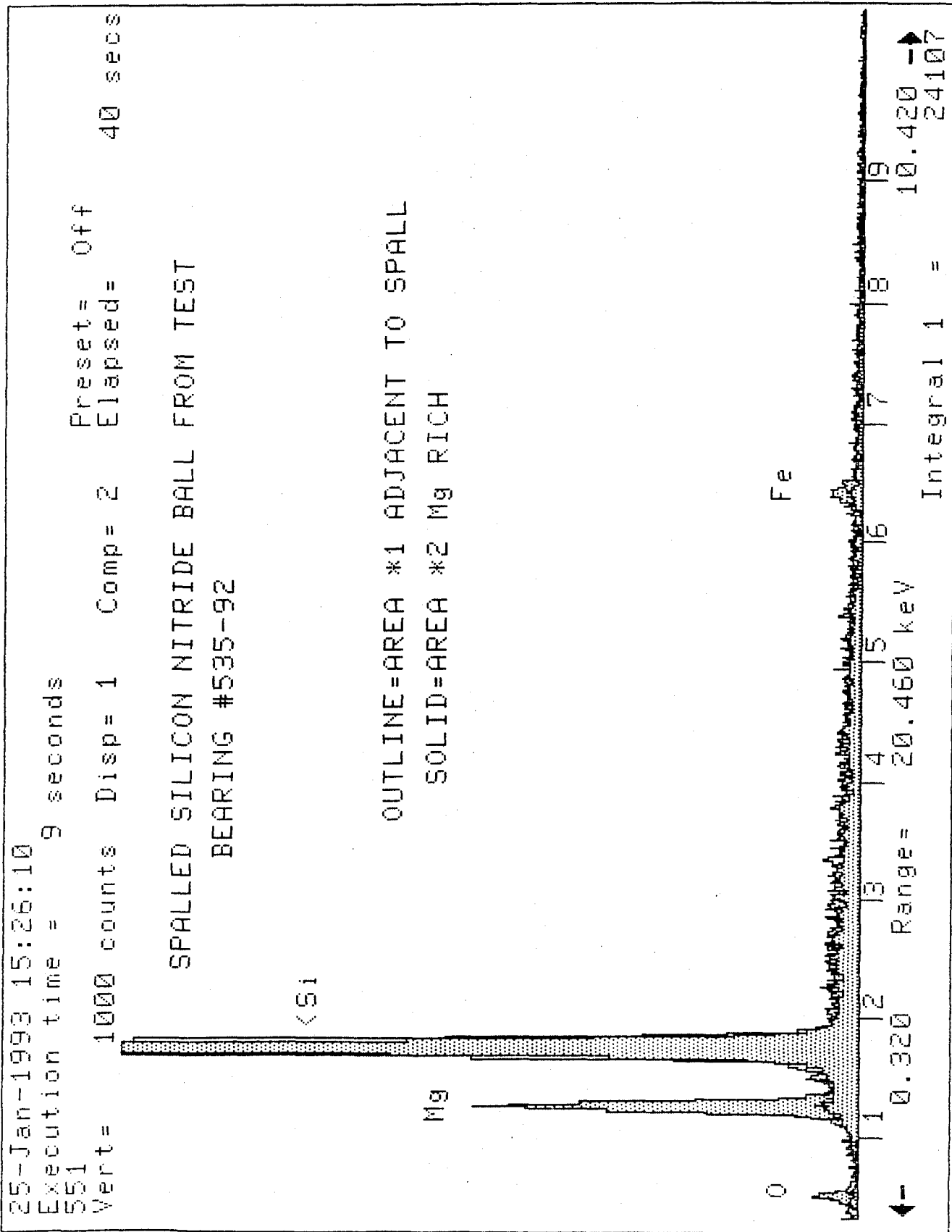
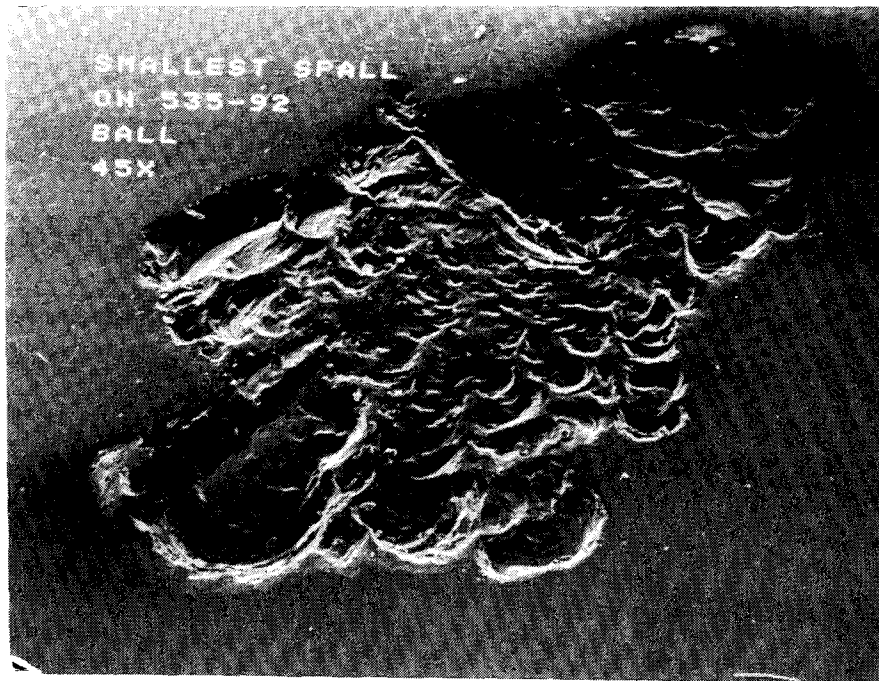


FIG.36 EDX Spectrum on the large spalls on a NBD-200 ball
(bearing No.535-92)

SMALL SPALL ON SILICON NITRIDE BALL f/ 535-92 BRG.

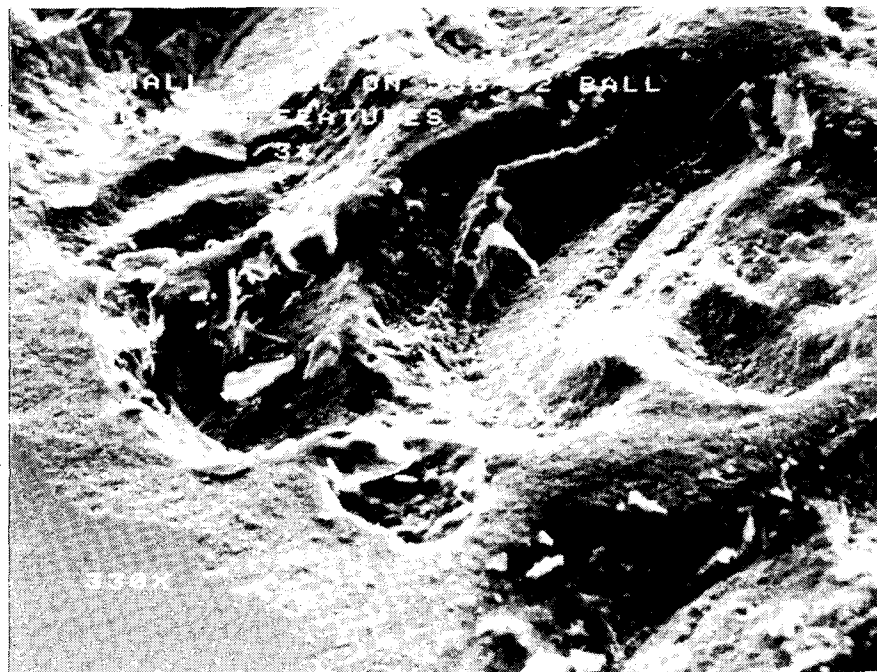


SEI

45X

SMALL SPALL

FIG.37a SEM photograph of a small spall (45x)
(bearing No.535-92)



SEI

330X

MAGNESIUM RICH
FEATURES IN SMALL SPALL

FIG.37b SEM photograph of a small spall (330x) around a Mg rich
feature (bearing No.535-92)

Both of the Mg rich features on the small spall map showed them to be inside the spalled area itself, as shown on the photos in Fig.37b. The individual EDX spectrums acquired from each of these ("3" and "4") are shown on Figs.38 and 39. Again, substantially more Mg was observed in these areas than in the typical silicon nitride. Of these two areas, "4" appears to be in its original position in the material. These observations indicate that excess sintering aids in the subsurface led to spalling.

4.4.2 Toshiba Balls

In the endurance test of 24 hybrid 206 ball bearings with Toshiba balls, there were four bearing failures. The failed bearing in the first group was #259-93, which had one spalled ball with a spalled area of about 2 mm in size (shown in Fig.40). The other balls had no spalls, but two of the eight unspalled balls had wear tracks. The steel raceways had severe wear and plastic deformation, as a result of overrolling by the spalled ball.

The failed bearing in the second group was No. 266-93. Examination showed there were four balls, each of which contained a spall, but one of the balls (shown in Fig. 41) had a spall larger than the other three. The raceways had no spalls but did have severe plastic flow, peeling and cracks. In this failed bearing, the failure origin could be on the ball with largest spalled area. The spalling failure on one ball caused severe damage to the inner raceway, which then caused the other three balls to spall.

The bearing that failed in the third group was No. 274-93, which had one spalled ball as shown in Fig.42. Again, the inner raceway had no spalls but did have plastic deformation and peeling.

The bearing that failed in the fourth group of six hybrid ceramic ball bearings with Toshiba balls was bearing No. 276-93. The test life of the bearing was 142.3 hours. After failure, the bearing was disassembled for examination, which showed that one ball had a spall of about 2 mm in size (shown in Fig. 43). The other balls had no spalls. The steel raceways, which show no spalls, had suffered severe wear and plastic deformation, as the result of the overrolling by the spalled ball.

26-Jan-1993 12:16:09
 Execution time = 1 seconds
 583
 Vert= 1000 counts Disp= 1
 Preset= Off
 Elapsed= 35 secs

Mg RICH FEATURE IN SMALLEST SPALL ON
 Si NITRIDE BALL F/ 535-92 BRG. (*3)

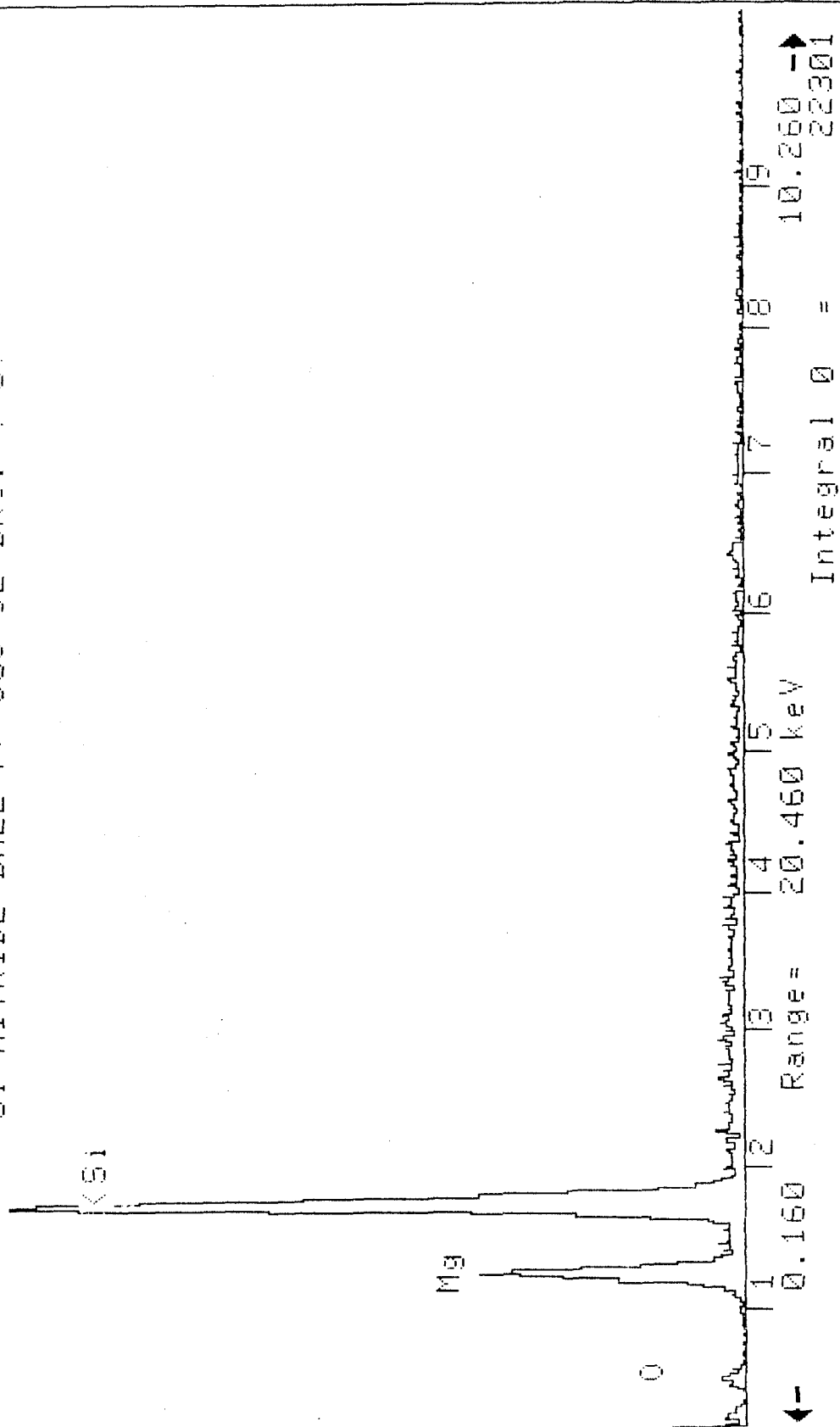


FIG.38 EDX spectrum of the Mg rich feature ('3')

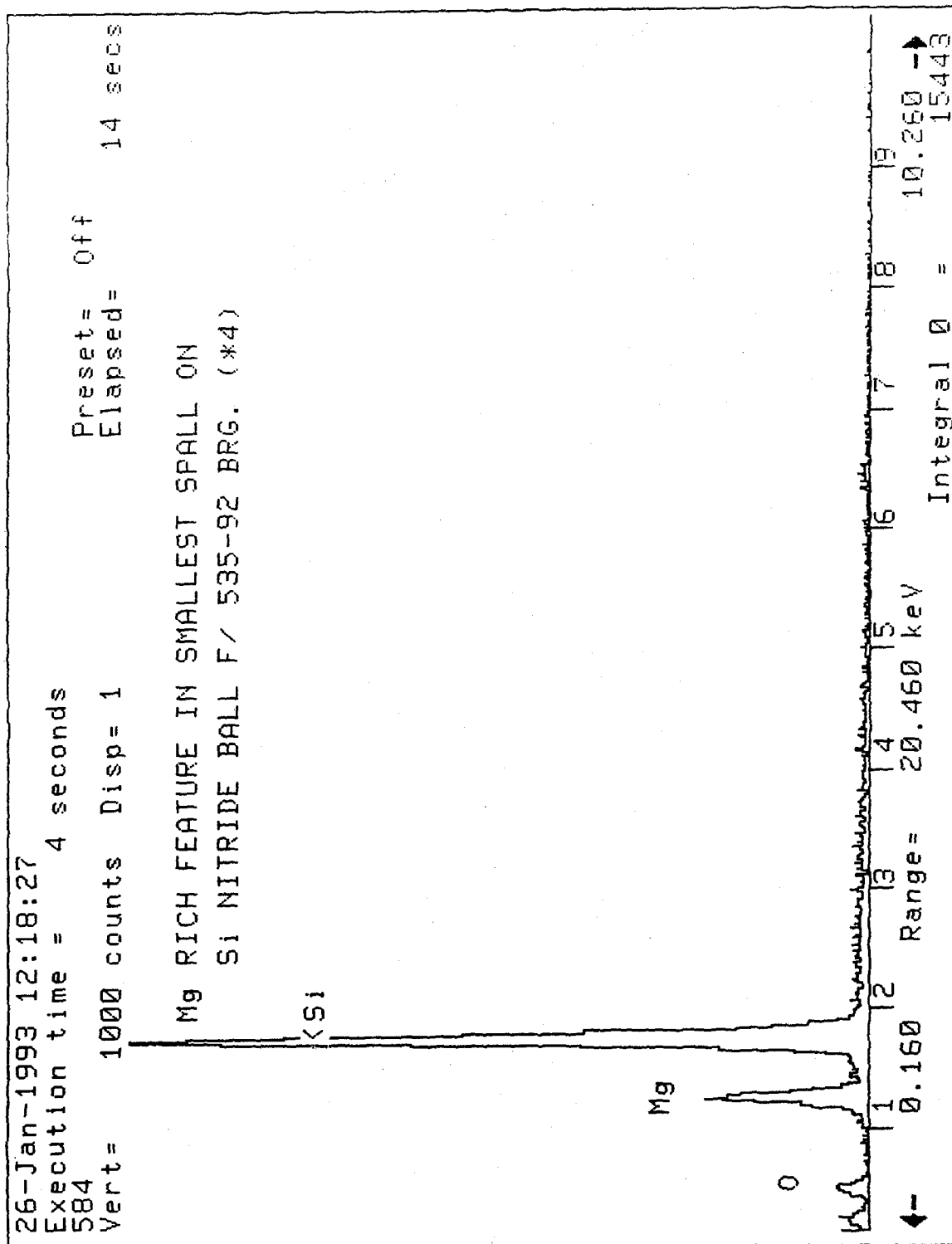


FIG.39 EDX spectrum of the Mg rich feature ('4')

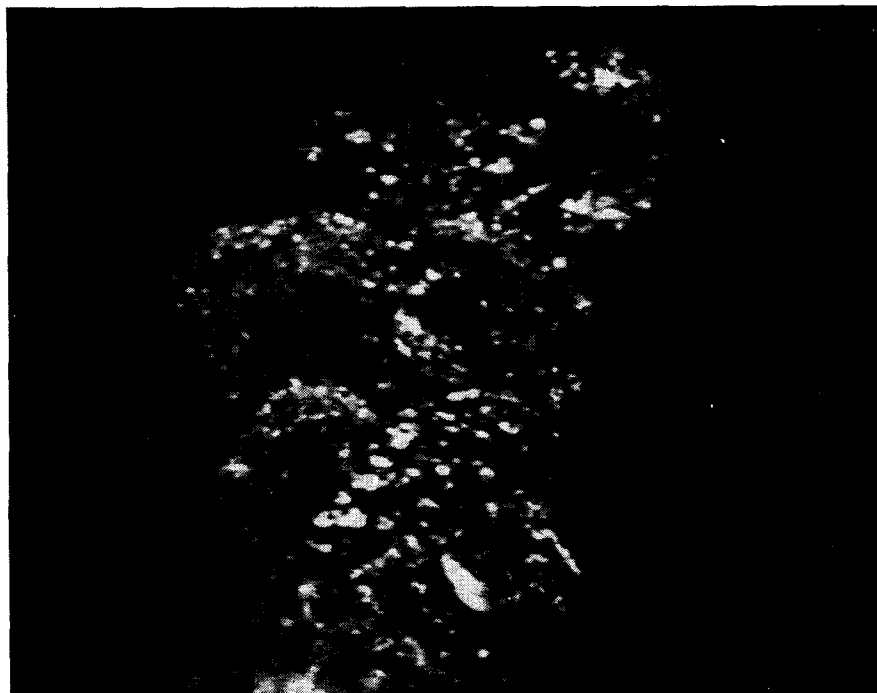


FIG. 40 Photomicrograph of spalled TSN-03H ball (80x) (bearing No. 259-93)

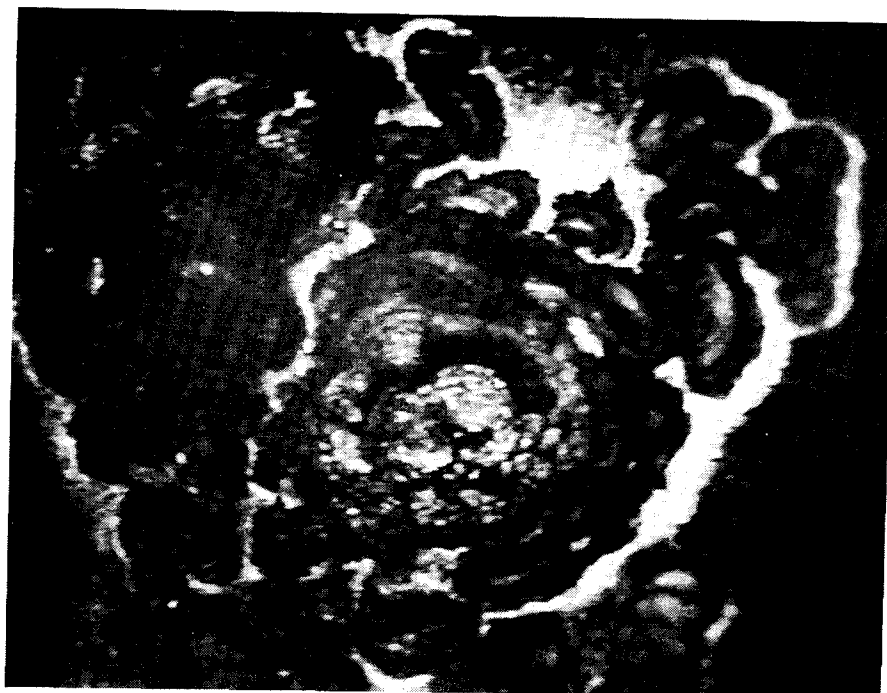


FIG. 41 Photomicrograph of spalled TSN-03H ball (bearing No. 266-93)



FIG. 42 Photomicrograph of spalled TSN-03H ball (bearing No. 274-93)

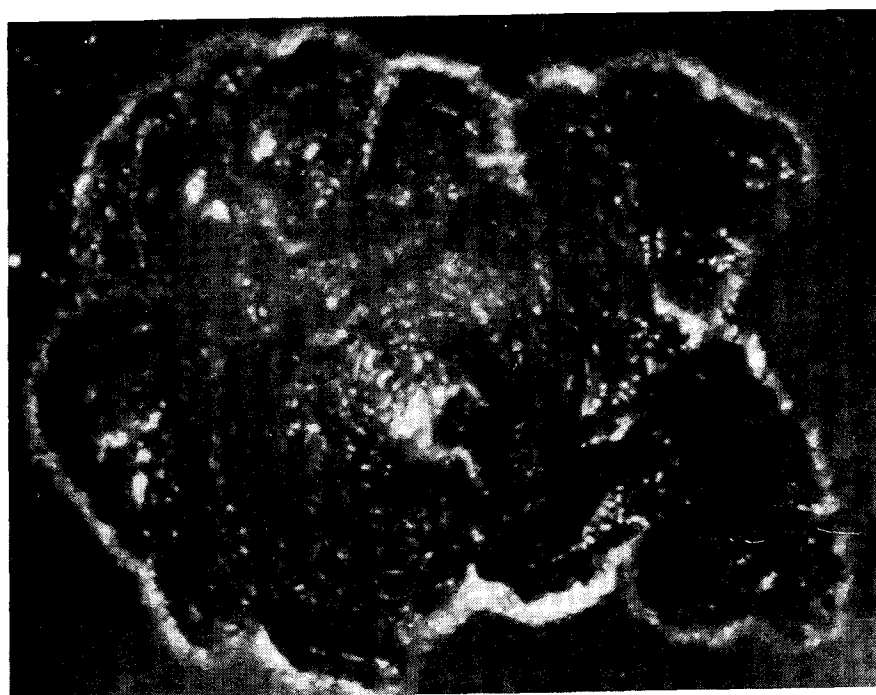


FIG. 43 Photomicrograph of spalled TSN-03H ball (bearing No. 276-93)

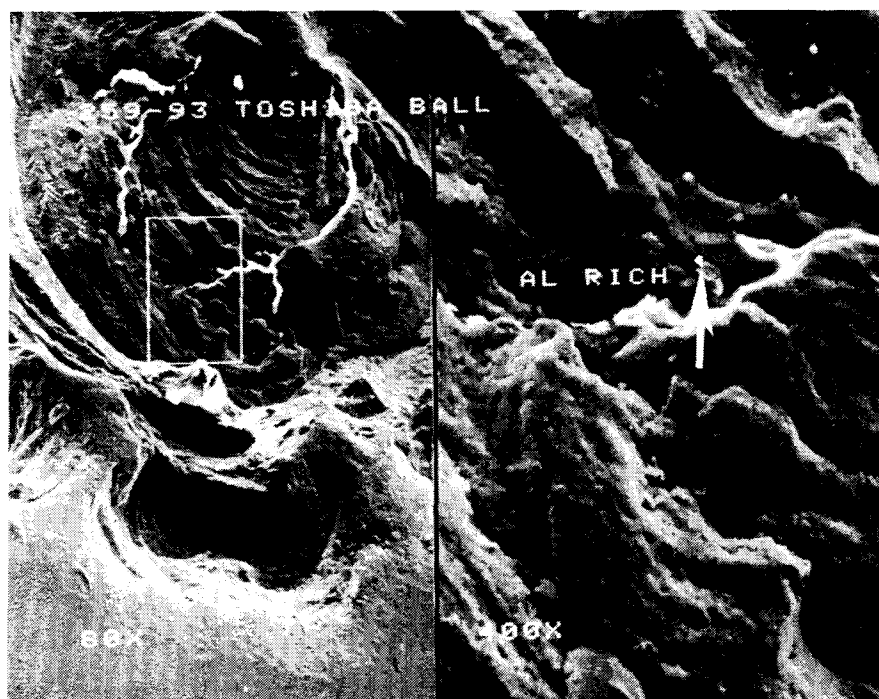


FIG. 44 SEM photograph of spalled TSN-03H ball (bearing No. 259-93).

Four spalled balls, one each from the failed bearings, were examined using SEM and associated EDX analyzer. Each of the spalled areas was lightly coated with carbon prior to the examination. The SEM/EDX examination of the four spalled balls showed there were two balls which contained small areas of several microns in size that were rich in a metallic element. In particular, the ball in failed bearing number 259-93 (173.2 hours test life) was found to contain an aluminum rich feature. Fig. 44 is the SEM photomicrograph of the magnified spalled area containing aluminum, shown by a white arrow. Fig. 45 contains the EDX result of the aluminum rich feature. The spalled ball in failed bearing number 266-93 (183.3 hours test life) was found to contain magnesium (Mg) and steel rich areas of several microns in size. Fig. 46 is the SEM photomicrograph of the magnified (80X) spalled area containing Mg (black arrow) and steel (Fe). Figs. 47 and 48 are the EDX results of the Mg rich and Fe rich areas respectively.

4.4.3 Bearing Rings

Visual examination has shown that the failure of the bearing originates from the ball spalling, rather than the bearing rings. The absence of failure origination from the ring surface is probably due to the excellent surface finish of the ring and the balls, as well as good lubricant film separating the surfaces in contact.

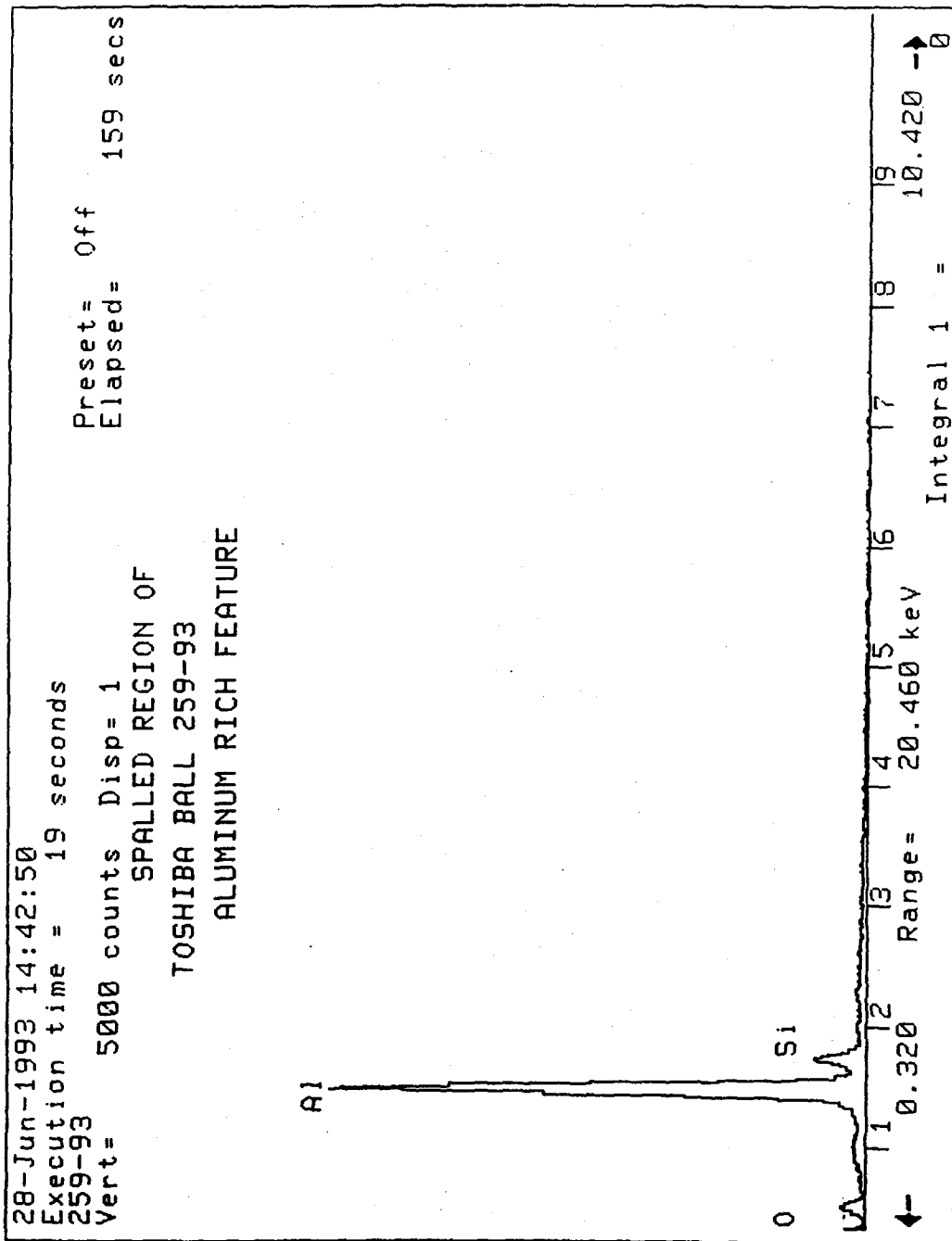


FIG.45 EDX result for spalled TSN-03H ball
(bearing No.259-93)

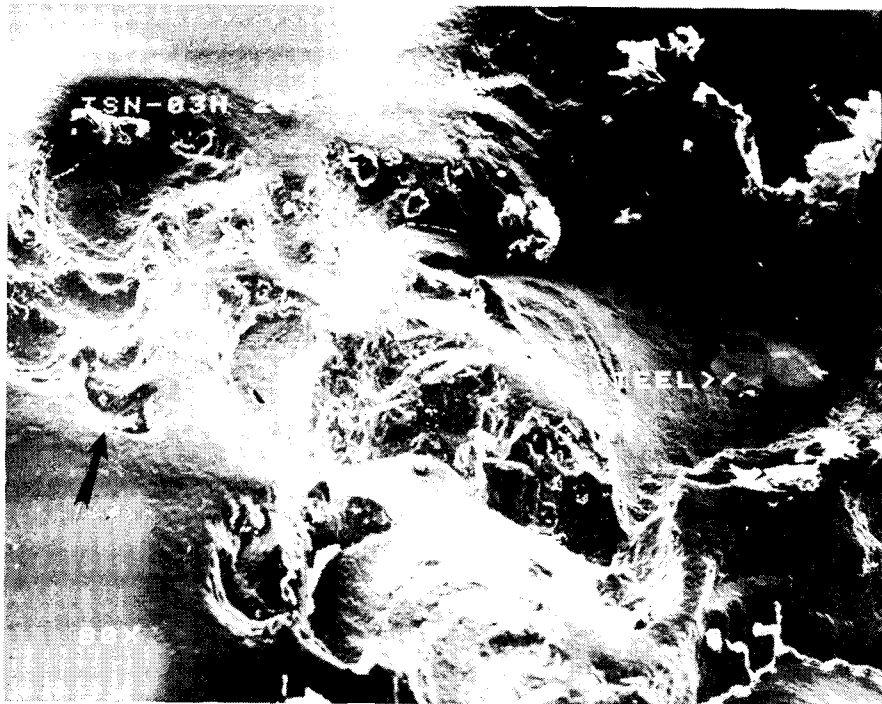


FIG.46 SEM photograph of spalled TSN-03H ball
(bearing No.266-93)

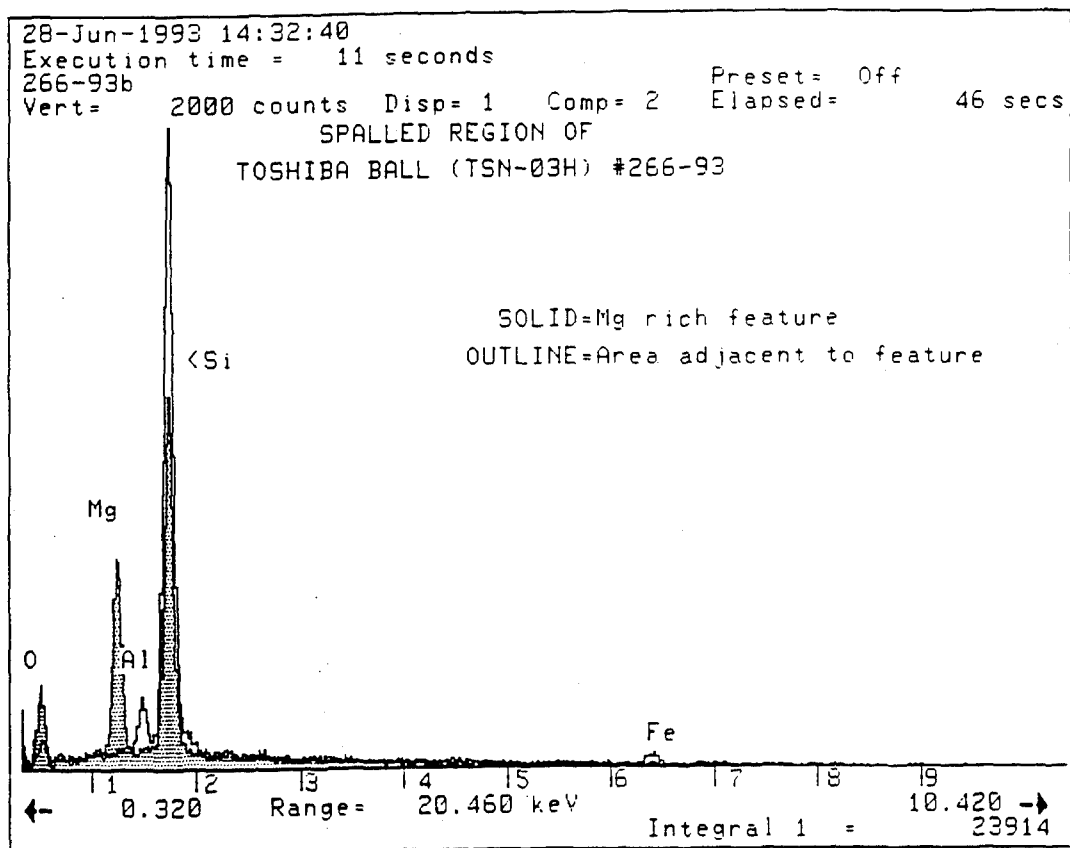


FIG.47 EDX result of spalled TSN-03H ball, Mg rich area
(bearing No. 266-93)

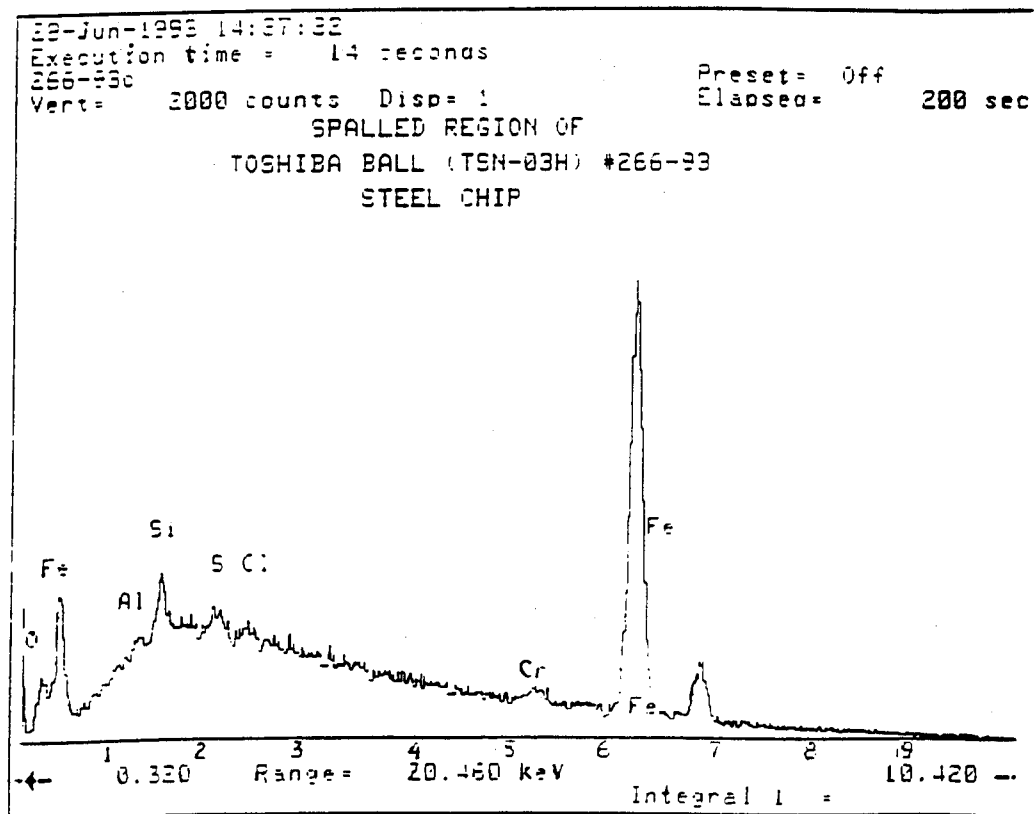


FIG.48 EDX result of spalled TSN-03H ball, Fe rich area
(bearing No. 266-93)

4.5 Maximum Likelihood Estimate of L10 Life for the Hybrid Bearings

Tests of the 48 hybrid bearings were completed with five bearings that failed by spalling, four of which contained TSN-03H balls and one which contained NBD-200 balls. For the hybrid bearing tests with Norton/Cerbec balls, there was only one bearing failure out of a total of 24 bearings tested. This single failure data point makes the conventional Weibull analysis inapplicable to obtain L_{10} life.

In the absence of applicable (conventional) Weibull analysis, a maximum likelihood analysis was applied to the reliability prediction of balls based on the following conditions:

1. The balls were subject to identical loading conditions at different test times and test rig positions.
2. Each bearing contained the same number of balls of the same type and the test conditions (i.e. temperature and lubricant) were the same.
3. The failure of the hybrid bearing in the particular group of bearings tested was due to (spalling) failure of one ball only.
4. The bearing failure was due to ball failure, not ring failure.

These conditions appeared to be valid for the present endurance tests with three identical test machines using six bearings.

For the endurance test of 24 bearings with Norton/Cerbec balls, there are $9 \times 24 = 216$ balls. The sample size of this ball test is 216, which consists of one failure of 13.6 hours of life and 215 suspensions with varying known lives.

A Maximum likelihood analysis was performed to determine the failure probability of a ceramic ball, based on the ball sample size of 216, with known lives for each of the balls. Knowing the failure probability of a ball subject to stress cycles in the bearing test, it was possible to calculate the failure probability of a hybrid ball bearing with a known number (9) of balls.

4.6 Theory

The failure probability of a ball in a hybrid bearing can be expressed as:

$$P_{f,ball} = 1 - \exp [- (N/N_o)^\beta] \quad (18)$$

where N is the life, N_o is the scale parameter and β is the Weibull slope. It was assumed that bearing failure was attributed to one ball failure, while the rest of the balls were treated as "suspensions." For a sample size of n and assuming the lives of all n balls were known for input, the use of maximum likelihood analysis permitted the unknowns N_o and β to be determined. Note that for the present test group of 24 bearings, the sample size $n=9 \times 24=216$.

For a ball bearing consisting of Z balls, the failure probability of the bearing is expressed in terms of N_o , β and Z as follows,

$$\begin{aligned} P_{f,bearing} &= 1 - [1 - P_{f,ball}]^Z \\ &= 1 - \exp [-Z(N/N_o)^\beta] \end{aligned} \quad (19)$$

From the above, the life N can be expressed in terms of bearing failure probability ($P_{f,bearing}$) as:

$$N = N_o \{ - \ln (1 - P_{f,bearing}) / Z \}^{1/\beta} \quad (20)$$

4.7 Result of ML Calculations

This maximum likelihood analysis for 216 balls in 24 bearings shows that the L10 life of the hybrid bearing with NBD-200 balls is about 35540 hours, while the one percent failure life (L1) is only 1.7 hours.

Table 10 tabulates the lives of 216 balls of NBD-200 material and the result of the maximum likelihood analysis based on 216 balls. The negative life values denote suspensions.

Similar calculations were performed for the test data of 24 hybrid 206 bearings with Toshiba balls based on 4 failures and 212 suspensions. Table 11 lists the lives of 216 balls of Toshiba

material and the results of analysis. It was shown that the calculated L_{10} life was 132 hours and the L_{50} life was 243 hours. Note that in Appendix D, Weibull software was used to calculate the L_{10} and L_{50} lives based on the failure lives of the four groups of hybrid bearings with Toshiba balls.. The calculated L_{10} was 124 hours and L_{50} was 424 hours. Comparison of the calculated lives based on the two methods shows closer agreement in L_{10} calculation (i.e., 132 versus 124 hours) than in the L_{50} calculation. The Weibull software was not applicable for test results of hybrid bearings with Norton balls, since only one failure data joint was available, which is insufficient for the conventional Weibull analysis.

The maximum likelihood calculated failure probability of hybrid 206 bearings with two baseline ball materials in terms of test hours and bearing revolutions is plotted in Figure 49. The calculated Weibull slopes were 0.236 and 3.1 respectively for the NBD-200 and TSN-03H. The value of Weibull slope for the hybrid bearing test with TSN-03H balls is many times greater than the Weibull slope in the rotating beam test of the same material. The reason for the large discrepancy in Weibull slopes in the rotating beam test and hybrid bearing test with the TSN-03H material is not known. Possible manufacturing flaws could exist in the ceramic balls, such as that reported by Bill Ellingson [34] of the Argonne Laboratory in his examination of Garrett made silicon nitride balls.

Table 10

NBD-200 ball endurance test data and
failure probability calculation
using maximum likelihood

TOTAL NUMBER OF ROLLING ELEMENT, SAMPLE SIZE= 216

LIST OF ROLLING ELEMENT LIVES

13.600	-13.600	-13.600	-13.600	-13.600	-13.600
-13.600	-13.600	-13.600	-13.600	-13.600	-13.600
-13.600	-13.600	-13.600	-13.600	-13.600	-13.600
-13.600	-13.600	-13.600	-13.600	-13.600	-13.600
-13.600	-13.600	-13.600	-13.600	-13.600	-13.600
-13.600	-13.600	-13.600	-13.600	-13.600	-13.600
-13.600	-13.600	-13.600	-13.600	-13.600	-13.600
-13.600	-13.600	-13.600	-13.600	-13.600	-13.600
-13.600	-13.600	-13.600	-13.600	-13.600	-13.600
-1509.900	-1509.900	-1509.900	-1509.900	-1509.900	-1509.900
-1509.900	-1509.900	-1509.900	-1509.900	-1509.900	-1509.900
-1509.900	-1509.900	-1509.900	-1509.900	-1509.900	-1509.900
-1509.900	-1509.900	-1509.900	-1509.900	-1509.900	-1509.900
-1509.900	-1509.900	-1509.900	-1509.900	-1509.900	-1509.900
-1509.900	-1509.900	-1509.900	-1509.900	-1509.900	-1509.900
-1509.900	-1509.900	-1509.900	-1509.900	-1509.900	-1509.900
-1509.900	-1509.900	-1509.900	-1509.900	-1509.900	-1509.900
-1509.900	-1509.900	-1509.900	-1509.900	-1509.900	-1509.900
-1509.900	-1509.900	-1509.900	-1509.900	-1509.900	-1509.900
-1511.500	-1511.500	-1511.500	-1511.500	-1511.500	-1511.500
-1511.500	-1511.500	-1511.500	-1511.500	-1511.500	-1511.500
-1511.500	-1511.500	-1511.500	-1511.500	-1511.500	-1511.500
-1511.500	-1511.500	-1511.500	-1511.500	-1511.500	-1511.500
-1511.500	-1511.500	-1511.500	-1511.500	-1511.500	-1511.500
-1511.500	-1511.500	-1511.500	-1511.500	-1511.500	-1511.500
-1511.500	-1511.500	-1511.500	-1511.500	-1511.500	-1511.500
-1511.500	-1511.500	-1511.500	-1511.500	-1511.500	-1511.500
-1511.500	-1511.500	-1511.500	-1511.500	-1511.500	-1511.500
-1511.500	-1511.500	-1511.500	-1511.500	-1511.500	-1511.500
-1509.000	-1509.000	-1509.000	-1509.000	-1509.000	-1509.000
-1509.000	-1509.000	-1509.000	-1509.000	-1509.000	-1509.000
-1509.000	-1509.000	-1509.000	-1509.000	-1509.000	-1509.000
-1509.000	-1509.000	-1509.000	-1509.000	-1509.000	-1509.000
-1509.000	-1509.000	-1509.000	-1509.000	-1509.000	-1509.000
-1509.000	-1509.000	-1509.000	-1509.000	-1509.000	-1509.000
-1509.000	-1509.000	-1509.000	-1509.000	-1509.000	-1509.000
-1509.000	-1509.000	-1509.000	-1509.000	-1509.000	-1509.000
-1509.000	-1509.000	-1509.000	-1509.000	-1509.000	-1509.000
-1509.000	-1509.000	-1509.000	-1509.000	-1509.000	-1509.000

WEIBULL SLOPE (BETA) = 0.2356
SCALE PARAMETER = 0.5601E+13

NUMBER OF ROLLING ELEMENT PER BEARING = 9

FAILURE PROBABILITY VS TEST HOURS

0.005000	0.1
0.010000	1.7
0.050000	1675.1
0.100000	35544.1
0.500000	105425120.0

TSN-03H ball endurance test data and failure probability calculation using maximum likelihood

LIST OF ROLLING ELEMENT LIVES

[illegible]

HETULL SLOPE (BETA) = 3.1061
 SCALE PARAMETER = 0.5544E+03

NUMBER OF ROLLING ELEMENT PER BEARING = 9

FAILURE PROBABILITY VS TEST HOURS

0.005000	49.7
0.010000	62.2
0.050000	105.0
0.100000	132.4
0.500000	242.9

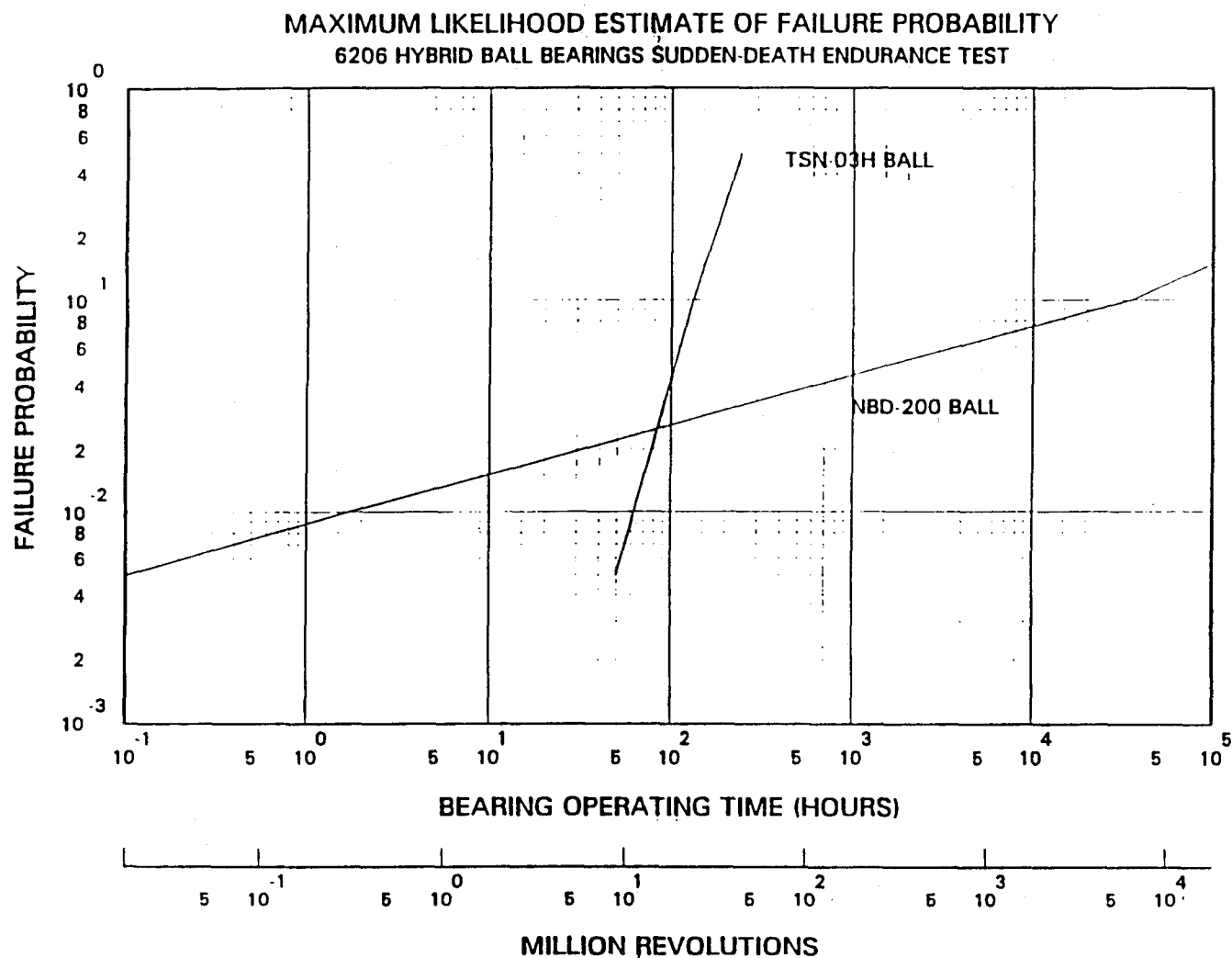


FIG.49 Maximum likelihood estimate of TSN-03H and NBD-200 ball failure probability based on endurance test data

5.0 TENSILE STRESS IN HERTZIAN CONTACTS

5.1 Tensile Stress On the Perimeter of a Hertzian Contact

The loading of a ball onto a shaft or a ball bearing raceway results in a Hertzian elliptical contact, in which an ellipsoidal pressure distribution prevails. The perimeter of the elliptical contact area is subject to tensile stress, acting normal to the elliptical boundary. For ceramic rolling element components, we consider the tensile normal stress as the critical stress which governs the crack growth under fatigue loading. For stationary Hertzian circular contact, which occurs when indenting a hard ball onto a flat, the tensile stress is the cause of "cone crack," which has been studied thoroughly by Lawn [35].

For a frictionless Hertzian contact, the magnitude of the tensile stress is a function of the Poisson ratio and the aspect ratio (axes ratio) of the ellipse. Johnson [36] and Lure [37] presented the closed form formulas for the stresses at the ends of the major and minor axes of a contact ellipse as shown in Table 12.

TABLE 12
Contact Ellipse Axes

	Coordinates	Formulas for Stresses
End of Major axis	$x = \pm a, y = 0$	$\sigma_x = -\sigma_y = p_0 (1-2\nu)(b/ae^2) [e^{-1} \tanh^{-1} e - 1]$
End of Minor axis	$x = 0, y = \pm b$	$\sigma_y = -\sigma_x = p_0 (1-2\nu)(b/ae^2) [1 - (b/ae) \tan^{-1}(ae/b)]$

where $e^2 = 1 - b^2/a^2$.

Figure 50 presents the plots of the ratio of principal tensile stress at the ends of the major and minor axis to the maximum contact pressure as a function of the aspect ratio (b/a) and Poisson ratio (ν). For given aspect ratio and maximum contact pressure, the maximum tensile stress at the edge of the contact ellipse is higher in ceramics ($\nu=0.26$) than in steel ($\nu=0.29-0.30$).

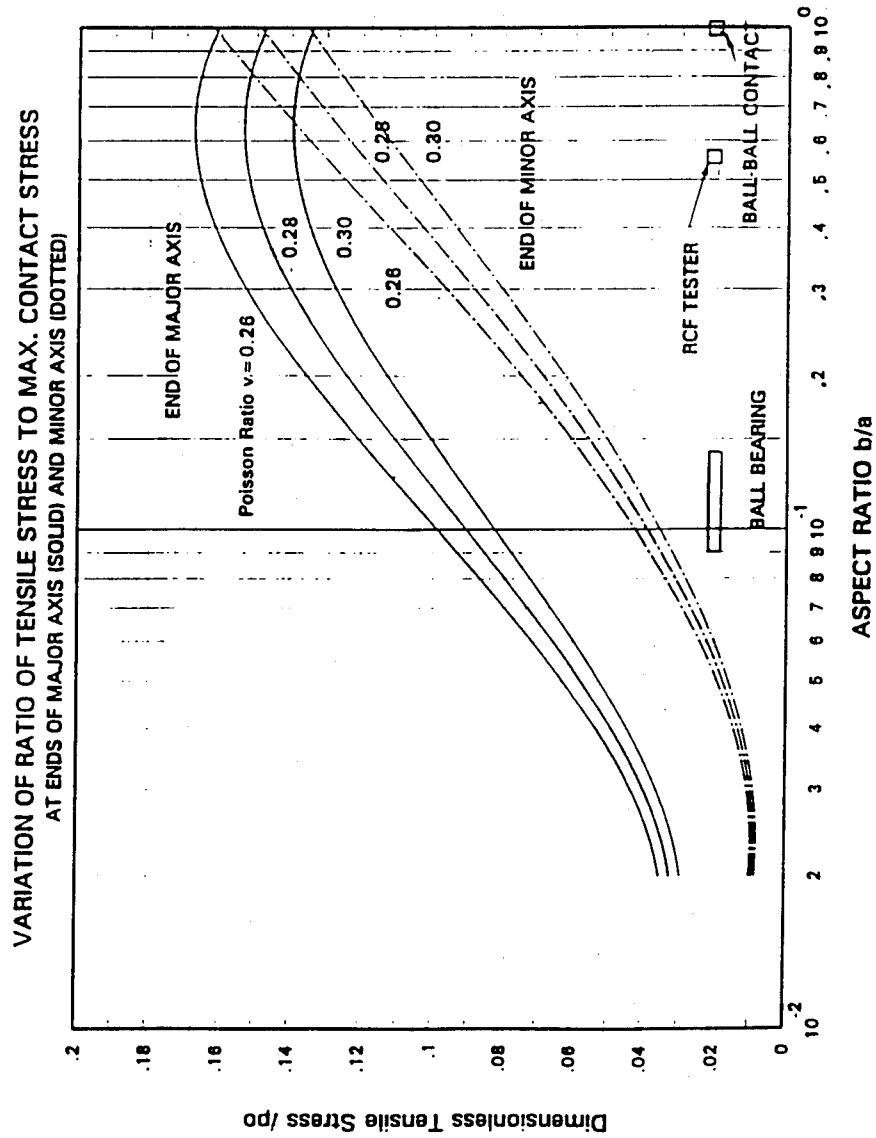


FIG. 50 Variation of Ratio of Tensile stress to maximum contact pressure at end of major and minor axes

Calculations have been made for the Hertz contact parameters of the elliptic contact for the 206 ball bearing and RCF test rig with particular interest in the tensile stress at the edge of the contact area. Table 13 tabulates the values of the aspect ratio a/b and the maximum tensile stress (scaled by the maximum contact pressure) for the 206 ball bearing, RCF test rig and the NASA five ball test rig. Table 13 also shows for three cases of maximum contact pressure, the maximum tensile stresses in the five ball rig and the RCF rig (under three levels of loadings). This calculation indicates the high likelihood of crack initiation along the edge of contact in the RCF rig and the five ball test rig.

TABLE 13
Calculation of Maximum Tensile Stresses
for Hybrid Hertzian Contacts
(use Poisson ratio 0.26 for silicon nitride)

	<u>206 Ball Bearing</u>	<u>RCF Test Rig</u>			<u>Five Ball Rig</u>
Radius of curvature:					
Rx	4.875		0.250		0.125
Ry	0.1663		0.107		0.125
Aspect ratio a/b	8.7736		1.756		1.0
<u>Max. Tensile stress</u> = Max. Contact stress	0.1043		0.168		0.16
Max. Contact stress (ksi)	538	<u>860</u>	<u>910</u>	<u>1000</u>	700
Max. tensile stress (ksi)	56.1	144	153	168	112
(MPa)	387	993	1055	1159	772

5.2 The Subsurface Principal Tensile Stress Field in Hertzian Elliptical Contact

The formulation for the stress at any arbitrary point in the solid under the Hertzian normal is available in [38,43]. In the subsurface zone beneath the perimeter of the contact, the maximum tensile stress occurs outside the projected elliptical area. Therefore, for given values of coordinates x ($< A$) and z (the depth), the computer program has to search for the y value where the principal tensile stress reaches the maximum value.

For the Hertzian contact without friction, Figs. 51 and 52 show the contours of equal maximum tensile principal stress as a function of x and z coordinates (scaled by b , the semi-minor axis) for the aspect ratio (a/b) equal to 8.774 and 1.765 respectively. Note that the aspect ratio 8.774 and 1.765 correspond to the inner ring contact of the 206 test hybrid bearing and the ball rod contacts of the FMC rolling contact test rig respectively. The values of the Poisson ratio used in these two plots are the same, i.e., 0.26, which is applicable to silicon nitride.

The principal tensile stress is important to the failure initiation in silicon nitride material. Experiment by Chao and Shetty [28] has shown that for silicon nitride, crack initiates mostly from the pores in a direction perpendicular to the direction of tensile principal stress. Thus, the stress contours shown in Figs. 51 and 52 are measures of volume distribution of severity for crack initiation in the cross section of the rolling track of a silicon nitride rolling element.

5.3 Tensile Stress Distribution in Frictional Hertzian Contact

Analytical solution of contact stresses is also available in [37,39] for a half space under the tangential traction acting on a contact ellipse. The friction force is assumed to follow the Coulomb law, i.e., the frictional traction is proportional to the Hertzian contact pressure. As a result of the friction force, additional tensile stress component arises at the trailing edge of the contact with friction. This solution is assumed to be applicable to the contact in hybrid ball bearing with uni-directional (or gross) sliding. A previous paper by Richerson et al. [44] has shown substantial tensile stress is present at the surface under combined normal and tangential

Note: Numbers around the contours denote values of ratio of principal tensile stress to the maximum Hertzian contact pressure. A and B are respectively the semi-major and minor axis of the contact ellipse.

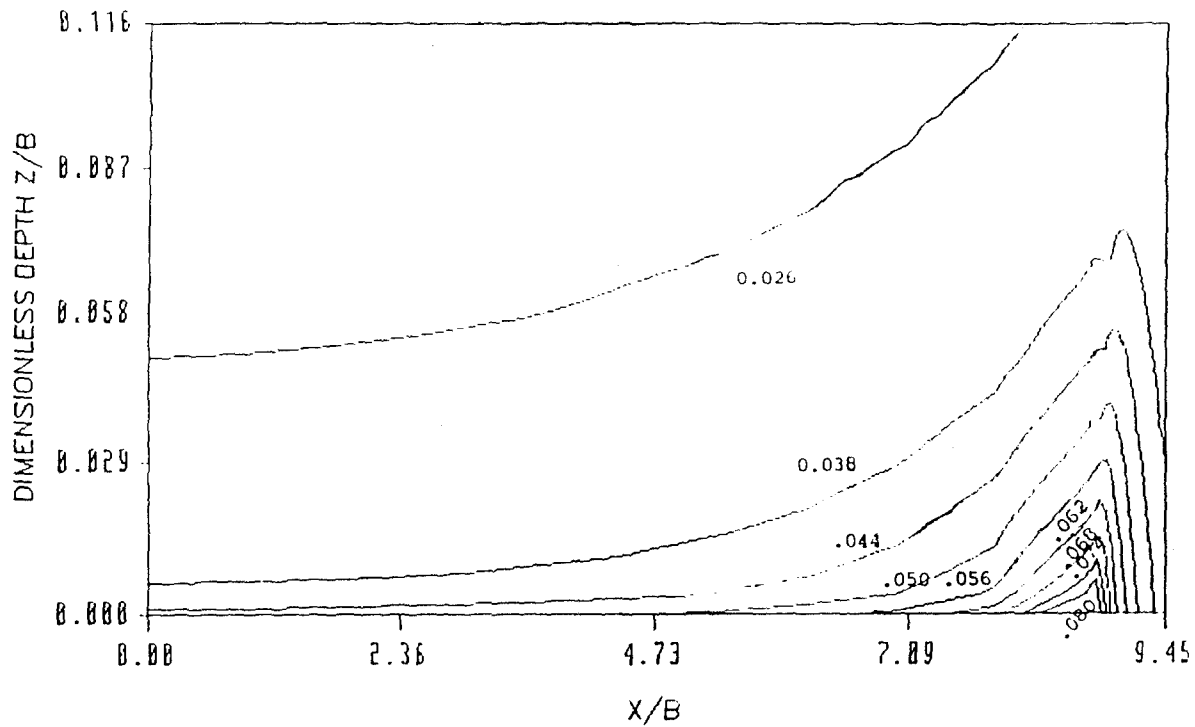


FIG.51 Contours of equal principal tensile stress for $a/b=8.774$, $\nu=0.26$ and $\mu=0$.

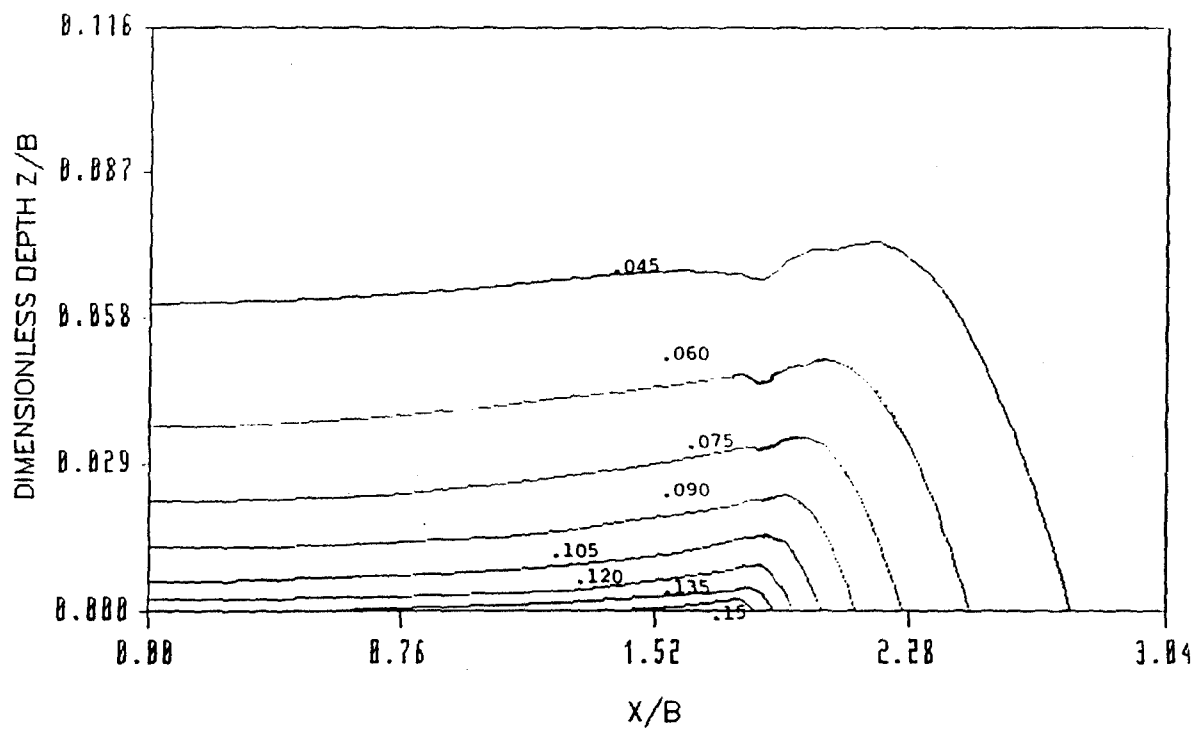


FIG.52 Contours of equal principal tensile stress for $a/b=1.765$, $\nu=0.25$ and $\mu=0$

load at the trailing edge of the contact. This tensile stress is very localized at the surface and its magnitude is highly dependent upon the coefficient of friction.

Detailed distribution of the principal stresses under a sliding Hertzian load with specified friction coefficient have been investigated for the case of 206 ball bearing inner ring contacts. The direction of sliding is assumed to be parallel to the minor axis of the elliptical contact. The results show that the maximum tensile principal stress occurs at the surface and the trailing edge of the contact at the end of the semiminor axis. Figs. 53 and 54 show, for friction coefficients equal to 0.05 and 0.10 respectively, the contours of equal principal tensile stress. The abscissa of the plot is x/B whereas the ordinate is z/B , where z is the depth from surface and x is the transverse coordinate from the center of the contact ellipse. The Poisson ratio is 0.26, which is applicable to silicon nitride material. The parameters of the contours are the ratios of tensile stress to the maximum contact stress. The maximum values of the tensile principal stress at the end of the minor axis are 0.142 and 0.238 for friction coefficients equal to 0.05 and 0.10 respectively.

$$A/B=8.774 \quad \nu=0.26 \quad \mu=0.05$$

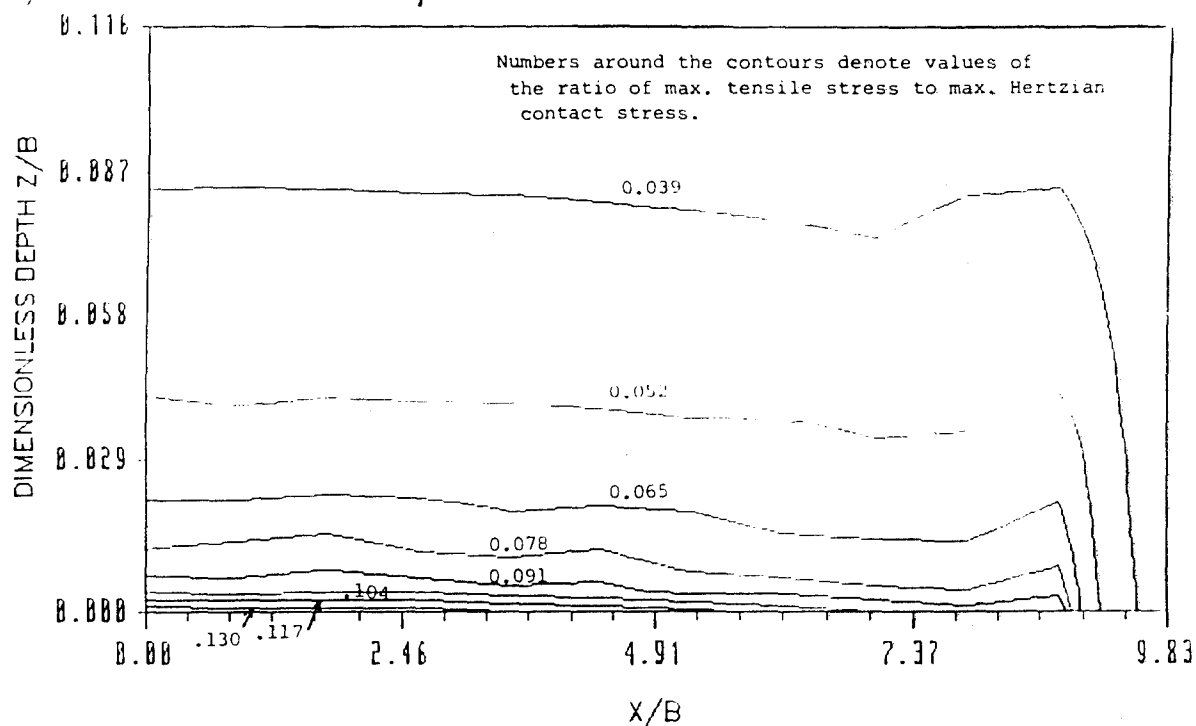


FIG.53 Contours of equal principal tensile stress for $a/b=8.774$, $\nu=0.26$ and $\mu=0.05$

$$A/B=8.774 \quad \nu=0.26 \quad \mu=0.10$$

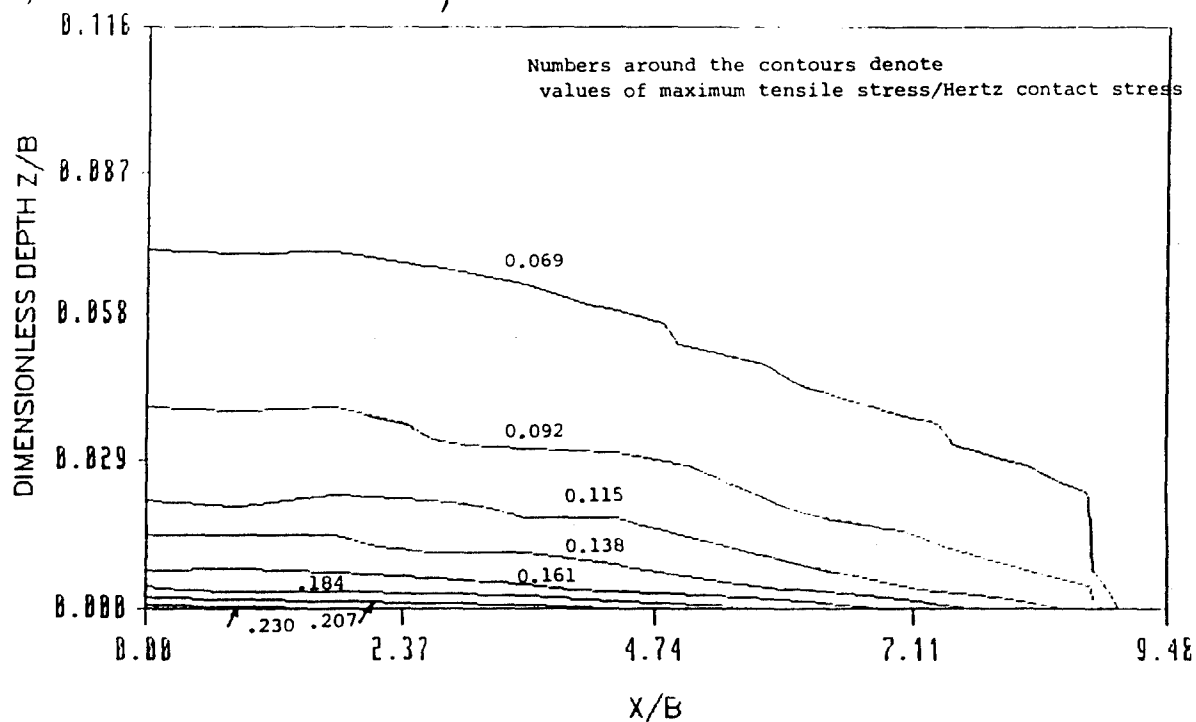


FIG.54 Contours of equal principal tensile stress for $a/b=8.774$, $\nu=0.26$ and $\mu=0.10$

Table 14 tabulates the values of the ratio of tensile stress to the maximum contact pressure for elliptical contact of two aspect ratios corresponding to those in a 206 bearing inner ring contact and the RCF test rig. The calculations were conducted for two surface locations, i.e., (1) at the end of the semi-minor axis, which is parallel to the direction of sliding, and (2) at the end of the semi-major axis of the contact ellipse. Also, two friction coefficient values, i.e., 0.05 and 0.10 have been used as input. The low friction coefficient corresponds to the case of well lubricated EHD contact whereas the high friction coefficient (i.e., 0.10) corresponds to a boundary lubricated contact under gross sliding.

TABLE 14
Values of Tensile Stress/Maximum Hertz Stress
at the Edge of Sliding Contact
(direction of sliding is parallel to the minor axis)

a/b	z/b	Friction coef. = 0.05		0.10	
		(1)** x*0	(2) x*a	(1) x*0	(2) x*a
8.774	0.	0.1423	0.1047	0.2384	0.1061
	0.10	0.0352	0.0010	0.0579	0.0019
1.756	0.	0.2220	0.1700	0.3100	0.1762
	0.10	0.0495	0*	0.0771	0.0665

* Compressive stress only.

** Location (1) at the lower end of minor axis. (2) at the end are respectively the semimajor and semiminor axis of the contact ellipse.

The results show that there is a strong effect of surface friction on the maximum tensile stress in contact with gross sliding. For a friction coefficient equal to 0.1, the maximum tensile stress reaches 31% of the maximum contact pressure. Even in the case of a low friction coefficient (0.05), the maximum tensile stress is about 21% of the maximum pressure. In most severely loaded ball bearing contacts, these tensile stresses precipitate the initiation of surface cracks, depending on the material or surface defects. The results indicate that gross sliding is detrimental to the contact fatigue of ceramic bearings.

6.0 FAILURE PROBABILITY PREDICTION FOR ROLLING CONTACTS

The objective here was to calculate the reliability of a silicon nitride rolling element using the solution of contact stress and the previously presented volume integration formulation for failure risk formulated in Section 3.5.2.

6.1 Assumptions

Several assumptions were made as follows:

1. The contact pressure between the rolling elements was assumed to be ellipsoidal as in a frictionless Hertzian contact, having an elliptical area of contact.
2. The frictional traction within the contact ellipse was assumed to be unidirectional, following the Coulomb law. The distribution of frictional traction is also ellipsoidal as is the contact pressure.
3. The effect of friction on the contact pressure in a Hertzian contact was neglected.
4. The critical stress in the failure probability formulation of a material element was assumed to be the maximum value of tensile stress the element experienced during the passage of a Hertz load. Also, volume flaw analysis was applied, which assumed that failure initiation was due to volume defect, rather than surface defects.

In both RCF rig and hybrid ball bearings, the contact pressure is Hertzian distributed. For the ball bearings, the calculations began with the contact force between the ball and the rings, the maximum contact pressure, and the major and minor axes of the ellipse of each contact. Subsurface stress distribution was calculated point by point in the material to determine the maximum tensile principal stress along the direction of rolling, over a grid on the plane normal to the direction of rolling. Volume integration was then performed numerically on Eq. (7) around the rolling track on the ball.

Only the failure probability of the ceramic components, i.e., the RCF rod and the balls in the hybrid bearings were to be calculated. The results of calculation are presented for the failure probability in terms of the number of stress cycles, or bearing revolutions.

A Cartesian coordinate system was used with its origin at the center of the elliptic contact area. We assumed z was the depth coordinate, x pointed to the transverse direction of the rolling track and y pointed to the rolling direction. For given values of x , y and z , the normal and shear stresses were first calculated, from which the principal stresses were obtained. For given values of x and z , the maximum values of principal tensile stresses along the points along the y -direction were determined by iteration. An area integration was performed over the highly stressed zone on the x - z plane using eq. (4) and the maximum tensile stress calculated above, which is a function of z and x . The volume integration in eq. (4) is the product of the above area integration and the track length of the RCF rod, which is 29.9 mm in perimeter.

Table 15 shows the material variables and operating parameters required as input to the failure probability calculation of a ceramic body with a rolling track under the moving Hertzian load with sliding friction. Typical values of the input are also given in the rightmost column of Table 15.

In thrust loaded ball bearings, all the balls were assumed to be equally loaded. The ball rotational axis was stationery with respect to the bearing axis. The ball-race contact should remain on the same track, resulting in a single wear track to be formed.

6.1.1 The Relationship Between Ball Rotational Cycles and Bearing Revolutions

The bearing angular velocity Ω_o is defined as the relative angular velocity between the inner ring and outer ring. Ω_o is the sum of the relative angular velocity between the inner ring and cage, Ω_{ic} , and the relative angular velocity between the outer ring and the cage, Ω_{ec} , or

$$\Omega_o = \Omega_{ic} + \Omega_{ec}$$

Note that $\Omega_{ic} R_i = \Omega_{ec} R_e = \frac{1}{2} \Omega_b D \cos \alpha$

$$R_i = \frac{1}{2} d_m (1 - \gamma)$$

$$R_e = \frac{1}{2} d_m (1 + \gamma) \quad (22)$$

TABLE 15 Input Constants for Reliability Prediction

<u>Material Constants:</u>		<u>Units</u>	<u>Typical values</u>
	Weibull modulus, m		10.
	Scale Parameter, σ_0	GPa	1.1
	Poisson ratio, ν		0.26
	Fatigue Exponent, n		25
	Crack Growth Constant, B	GPa ² Cycles	4.E+6
<u>Operating Constants:</u>			
	Maximum Hertzian Pressure, P_{max}	GPa	3.5
	Wear Track Diameter	mm	11.1
	Number of Load		1
	Semi-major axis, a	mm	2.2
	Semi-minor axis, b	mm	0.25
	Sliding friction coefficient, μ		0.05
	Cycles		1.E5

where d_m is the bearing pitch diameter, D the ball diameter, α the contact angle,
and $\gamma = D \cos \alpha / d_m$

The above equations become:

$$(1-\gamma)\Omega_{ic} = (1+\gamma)\Omega_{ec} = \Omega_b \gamma \quad (23)$$

The bearing angular velocity becomes:

$$\Omega_o = [\gamma/(1+\gamma) + \gamma/(1-\gamma)] = 2 \Omega_b \gamma / (1-\gamma^2) \quad (24)$$

Thus the number of bearing revolutions is equal to the number of ball rotational cycles multiplied by a factor $2\gamma/(1-\gamma^2)$.

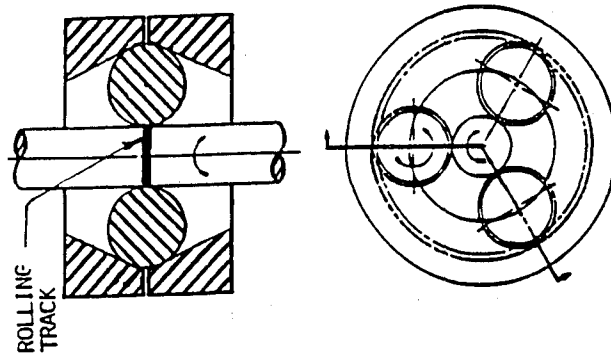
6.2 Example 1 - Ceramic Rod in RCF Tester

A RCF rod of silicon nitride ceramics tested in a ball-rod test rig (i.e., the Federal Mogul tester) was considered. In this test configuration (see Fig. 55a), there were three preloaded orbiting balls of 1/2" diameter in contact with the rod of 3/8" diameter. The maximum contact stress between the rod and the balls was assumed to be 6.0 GPa for steel ball and ceramic rod contacts. Under this load, the semimajor and semiminor axes of the contact ellipse were 0.398 mm and 0.227 mm respectively. The aspect ratio $a/b = 1.756$.

Ref. [41] shows that, in a RCF rig, one revolution of the test rod corresponds to 2.389 contact stress cycles acting on the rod.

The typical maximum contact pressure applied in this test was 6.4 GPa (930 ksi). However, as reported by Lucek [5], wear and possible plastic deformation on the ball and rod surfaces resulted in a concave curvature and subsequently lower maximum contact pressure. According to Lucek [42], the reduced maximum contact pressure was about 6.0 GPa as the result of wear. Note that both [5] and [7] reported that the major cause of failure in the highly stressed RCF test was the microcracking at the edge of the rolling track due to the tensile stress at the edge of the elliptical Hertz contact.

RCF TESTER
(CERAMIC ROD)



HYBRID BALL BEARING
(CERAMIC BALLS)

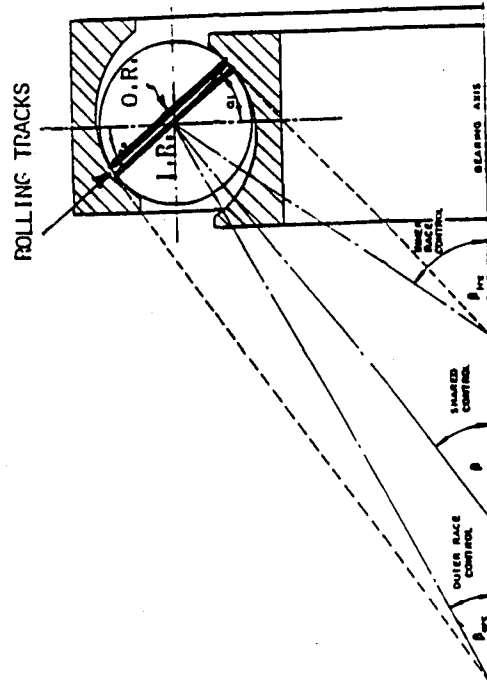


FIG.55b Rolling Tracks on ball bearing balls

FIG.55a Federal Mogul RCF test configuration

Numerical examples were calculated for the failure probability, i.e., the probability of the occurrence of a macrocrack as a function of life in cycles for the two materials using Poisson ratio 0.26 for the two cases. The results of failure probability calculation versus the life in cycles for the two materials were plotted in Fig.56. It was shown that at low cycles, the failure probability was dominated by that due to fast fracture, the failure probability of the two materials at low cycles was about equal. At higher cycles, the NBD-200 rod had lower failure probability than the TSN-03H rod. Since the property data of TSN-03H showed the values of the Poisson ratio varied from 0.26 to 0.28, additional reliability calculation was performed for TSN-03H using Poisson ratio (ν) equal to 0.28. The results of failure probability in these calculations, together with the previously calculated values for the two materials using Poisson ratio equal to 0.26 were plotted in Fig.57. It was shown that the failure probability of TSN-03H at $\nu=0.28$ was lower than that with $\nu=0.26$, because the former had lower maximum tensile stress at the edge of the contact than the latter. The failure probability of TSN-03H using three values of Poisson ratio (0.26, 0.27 and 0.28) as parameters was plotted in Fig.58. The results show that failure probability was a strong function of the Poisson ratio of the ceramic material.

For the RCF test at maximum contact stress of 6 GPa between the ceramic rod and three orbiting balls, Fig.59 plots the variation of failure probability with stress cycles for the rod of the TSN-03H ceramics using the sliding friction coefficient on surface as parameters was plotted in Fig.59. The curves show that the failure probability was not zero at small number of stress cycles because ceramic material always had certain probability of fast fracture failure even before the cycling began. It was also shown that the failure probability increased rapidly with increasing friction coefficient. The greater predicted failure probability in TSN-03H rod than in NBD-200 rod in high cycles is consistent with the previous RCF testing at MTI reported in [14].

Figure 60 shows that the maximum tensile stress in the ball-rod contact with maximum pressure 4 GPa at the edge of the rolling track (Fig. 55a) increased rapidly with the friction coefficient.

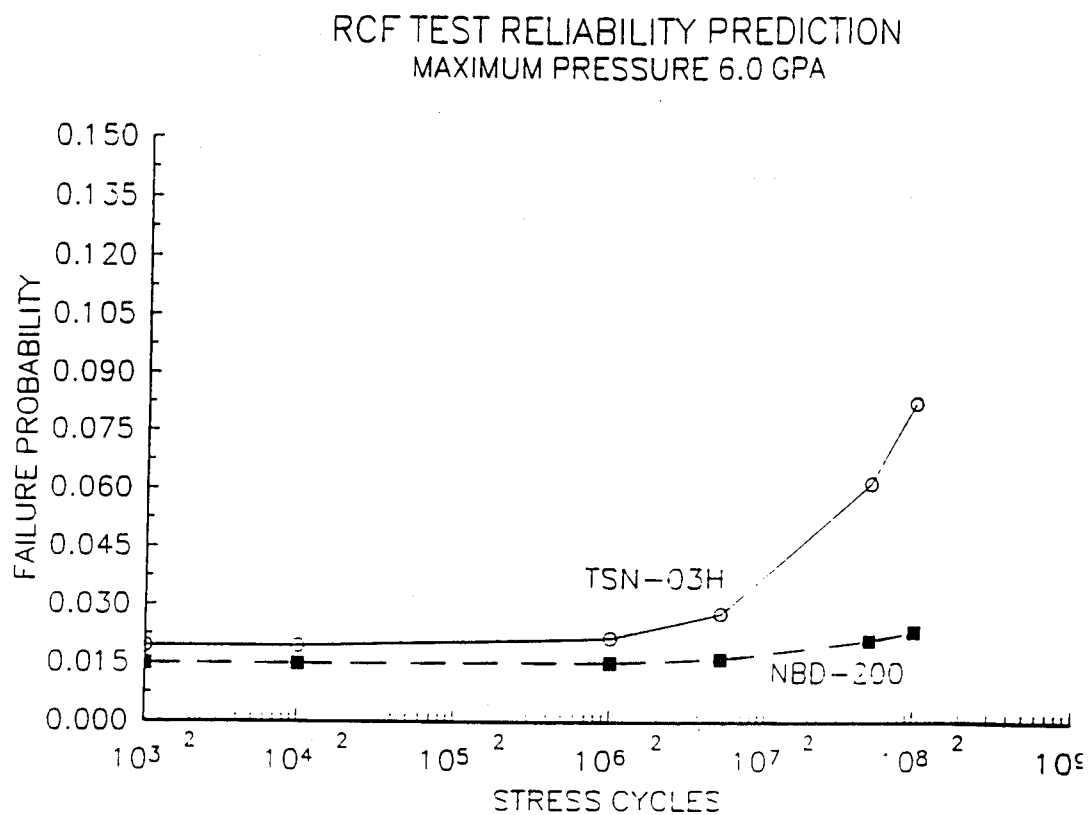


FIG.56 Failure probability of RCF rod of two ceramic baseline materials at $p_{\max} = 6.0$ GPa

RCF TEST RELIABILITY PREDICTION MAXIMUM PRESSURE 6.0 GPa

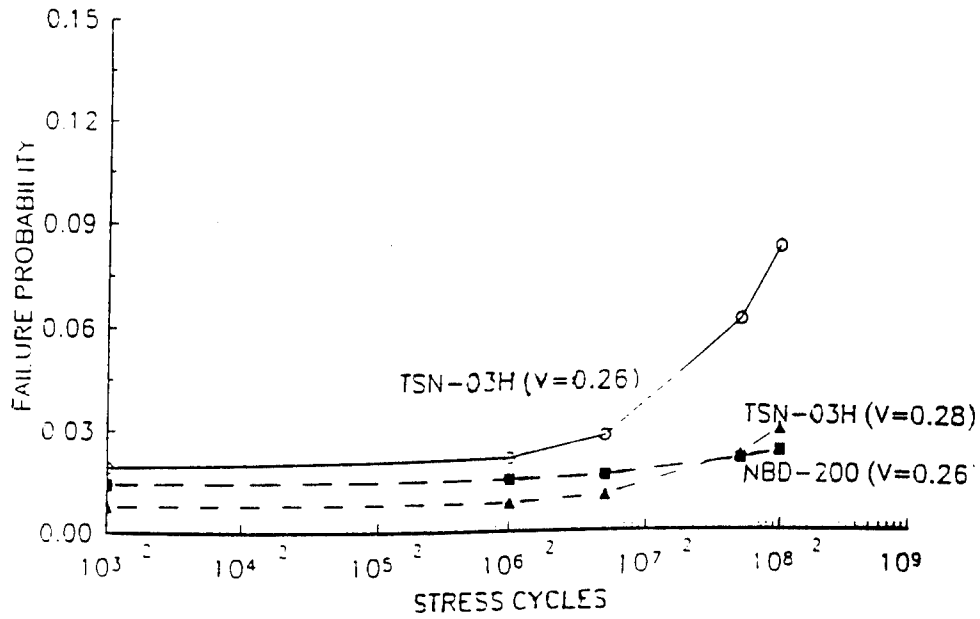


FIG.57 Failure probability of RCF rod of two ceramics with different Poisson ratios at $p_{max} = 6.0$ GPa

VARIATION OF RELIABILITY WITH POISSON RATIO TSN-03H

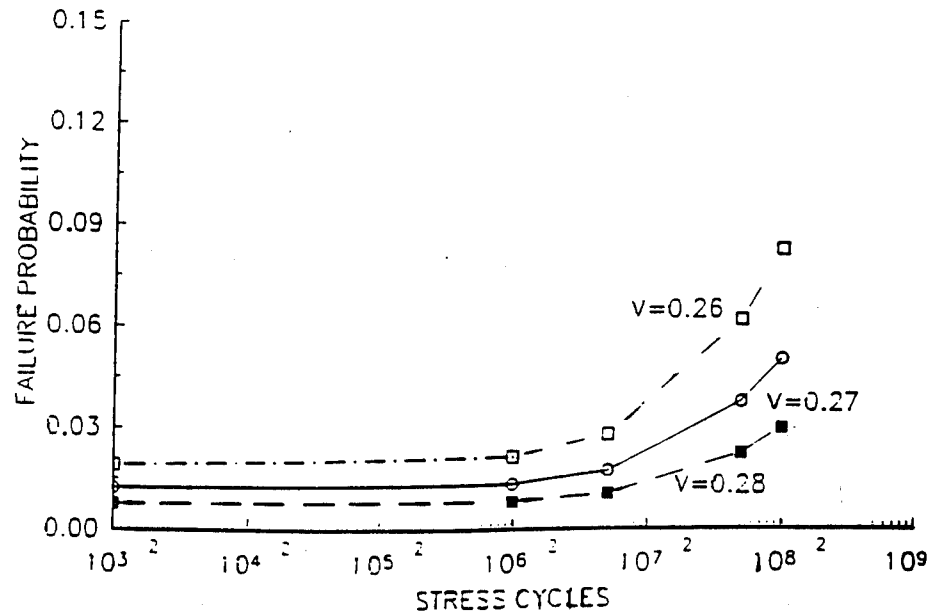


FIG.58 Variation of failure probability of TSN-03H RCF rod with Poisson ratio at $p_{max} = 6$ GPa

RELIABILITY OF RCF ROD MAT."A"
MAX. PRES. 6 GPa

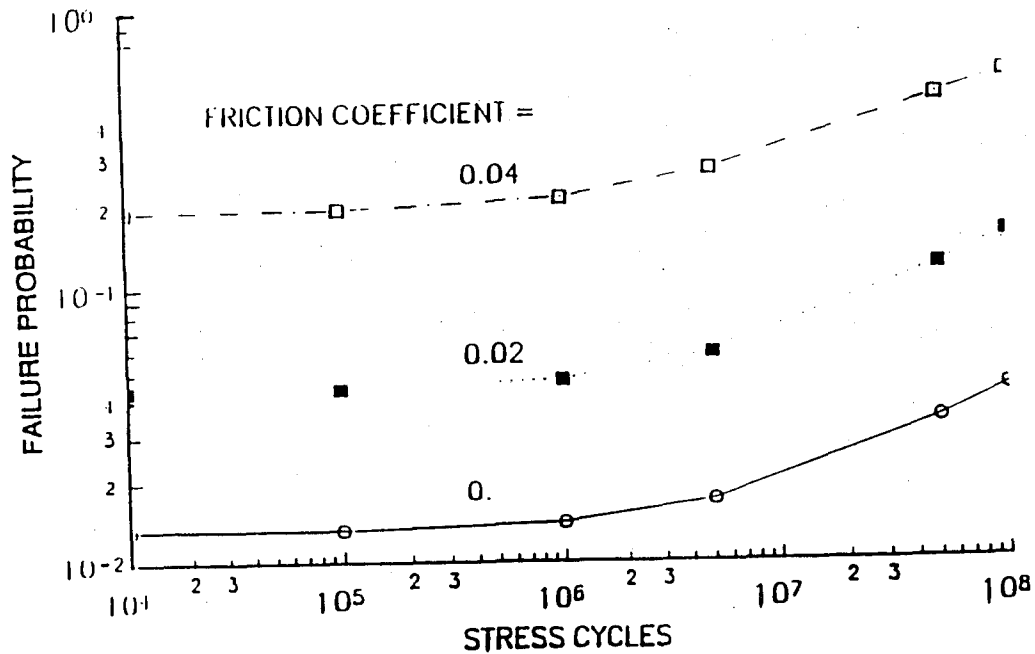


FIG.59 Variation of failure probability of TSN-03H RCF rod with friction coefficient at $p_{max} = 6.0$ GPa

MAXIMUM TENSILE STRESS VS FRICTION COEFF.
RCF ROD, MAX.PRES. 4 GPa

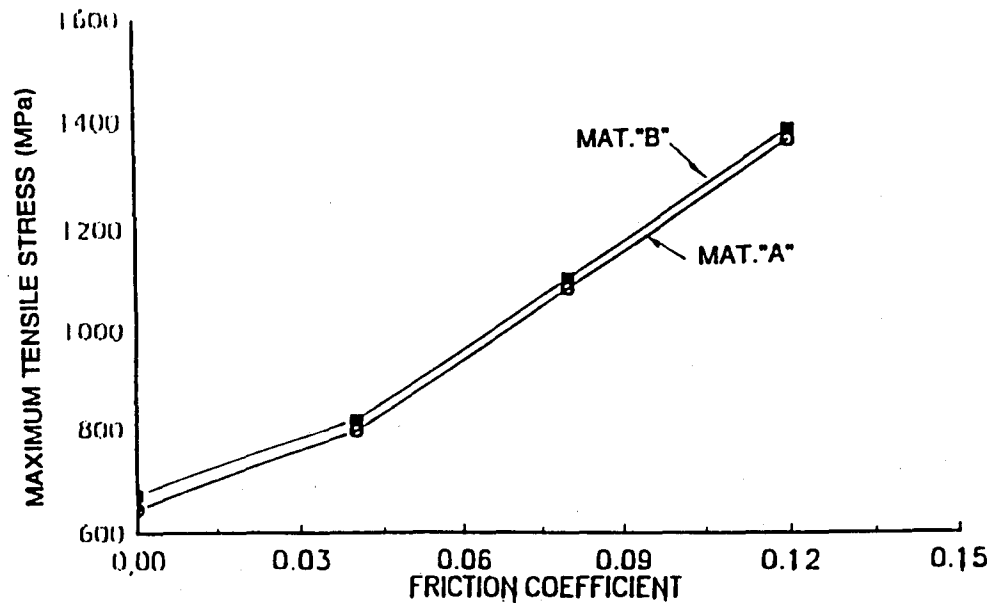


FIG.60 Variation of Maximum tensile stress in NBD-200 RCF rod with friction coefficient, at $p_{max} = 4.0$ GPa

6.2.1 Maximum Tensile Stress and Effective Volume in RCF Contacts

Table 16 tabulates, for the RCF rod contact with maximum contact pressure 6.0 GPa, the values of maximum tensile stress and effective volume for three cases. Table 17 shows the comparison of effective volume in the RBF test specimen, the 4-point bending test (used by Norton/Cerbec), the 3-point bending test (used by Toshiba Co.), as well as the RCF test rod at 6.0 GPa maximum pressure. The very low values of the effective volume in the RCF rod explain its ability to stand very high tensile stress (in the order of 1 GPa) with many million cycles of fatigue life, while in the static 3-point bending (MOR) test by Norton/Cerbec Inc., the failure stresses of the MOR bars were mostly lower than 1 GPa. In the latter, the effective stress volume was 12 mm³, which is much greater than that of the RCF rod under loading from balls. This comparison showed the stress volume was an important parameter in reliability estimation, in both fast fracture as well as in cyclic fatigue. For rolling contacts, the stress volume was small, so that high tensile stress did not cause high failure probability.

6.3 Example 2 - Angular Contact Hybrid Ball Bearings

An angular contact hybrid ball bearing under pure thrust load was considered. The detail bearing and contact dimensions are given in Table 18. The balls were equally loaded and the ball-race contact forces moved around rolling tracks on the balls, which lies on a plane perpendicular to the axis of rotation of the ball with respect to the bearing cage, as shown in Fig.55b.

The case of a thrust loaded ball bearing was considered here for simplicity, since the ball and race contact remained on the same track.

The failure probability of a ball set with Z balls was calculated using

$$P_{\text{ball set}} = 1 - (1 - P_{\text{ball}})^Z \quad (25)$$

For the stressed volume around the rolling track (or tracks) on a ball, the failure probability was first calculated for one ball under the moving loads of inner and outer ring contact forces.

TABLE 16
Variation of Maximum Tensile Stress, Effective Volume
in RCF Contacts at Maximum Pressure 6.0 GPa

Material type ratio	Poisson Stress (MPa)	Max. Tensile Stress (MPa)	Eff. Volume (mm³)
TSN-03H	0.26	1007	0.0485
TSN-03H	0.28	923	0.0472
NBD-200	0.26	1007	0.0554

TABLE 17
Comparison of Effective Volumes in Various Tests

Test Type	Effective Volume, mm³
RBF Test	40 - 44
4-pt bending (Cerbec)	12
3-pt bending (Toshiba)	1.6
RCF Test (P _{max} = 6 GPa)	0.047 - 0.055

The reliability prediction of ceramic balls in a pure thrust loaded hybrid ball bearing, in which the balls "track" without tumbling was similar to that of a ceramic rod in a RCF ball-rod tester, since both have clear rolling tracks in which the stress volume and stress cycles can be defined. Such purely thrust loaded hybrid ball bearing testing is currently underway in the Timken Company's test laboratory under contract with Norton/Cerbec Co.

Table 18

Test Conditions and Dimensions of A Pure Thrust Loaded Hybrid Ball Bearing

Number of balls	28
Ball Diameter	11.11 mm
Speed	2700 rpm
Bearing load F_{axial}/F_{radial}	30.3/0 kN
Lubricant	Exxon-89
Ball material	Si_3N_4 'B'
Bearing Pitch Diameter	111.8 mm
Contact angle	33 degrees
Maximum contact pressure	2.41 GPa (inner), 2.39 GPa (outer)
Contact Semi-major/minor axis	2.11 mm/0.183 mm(inner) 1.84 mm/0.212 mm(outer)

Based on the method of volume integration of a moving Hertzian elliptical contact given in Section 3.6 for single and multiple contact loads and the material constants obtained from the statistical analysis of the rotating beam test data for the two baseline materials, a calculation was performed to determine the failure probability of the ceramic body (i.e., a ball) under cyclic contact loads. The contact loads consisted of the ball-inner race contact load and the ball-outer race contact load. The failure probability was calculated separately for the inner and outer ring contact loading. Equation (17) was then applied to obtain the total failure probability of a ball in a bearing subjected to both inner and outer ring contact loading.

Using the above Hertzian contact parameters as input, the failure probability of one ball (P_{ball}) in the Norton/Cerbec test bearing was calculated first. The failure probability of the 28 ball set in this bearing was calculated using Eq. (25). For the above mentioned pure thrust loaded hybrid bearing, the failure probability of the 28 ball set with a single rolling track (dashed curves) and the double tracks (in solid curves) as a function sliding friction coefficient, ball contact cycles (or bearing revolutions) were plotted in Figs.61 and 62, respectively, for TSN-03H and NBD-200 ball materials.

In the above plots, the increased failure probability in the case of double tracks on the balls was due to the increased stressed volume from the single track.

In the above calculation, the maximum contact stress was 350 ksi (or 2.4 GPa). The sliding friction coefficient was assumed to be uniform throughout the contact ellipse. The direction of sliding was the same as the direction of rolling, i.e., it applied to the case of gross sliding in the bearing.

For the case of Cerbec test bearings, we had $D = 11.11$ mm and $d_m = 112$ mm, $\alpha = 33^\circ$, which yielded $\gamma = 11.1/112 \times 0.8387 = 0.083$ and

$$\Omega_o / \Omega_b = 2\gamma / (1 - \gamma^2) = 0.1675$$

The result shows that the failure probability was a weak function of the stress cycles and strong function of the friction coefficient. The failure probability was approximately a constant for stress cycles less than 10^7 cycles. Also, for friction coefficient less than 0.10, the failure probability was negligibly small below 10^8 cycles.

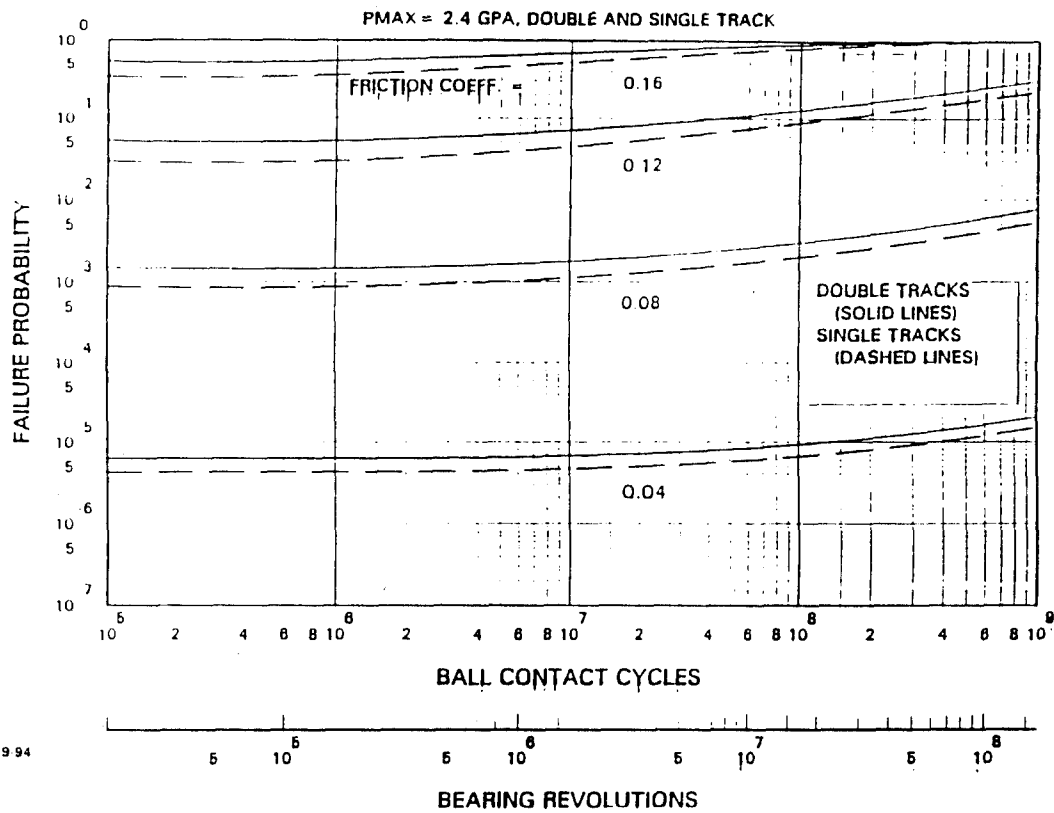


FIG. 61 Failure probability of track-forming TSN-03H (28) ball set with cycles and friction coefficient, $p_{\max}=2.4$ GPa

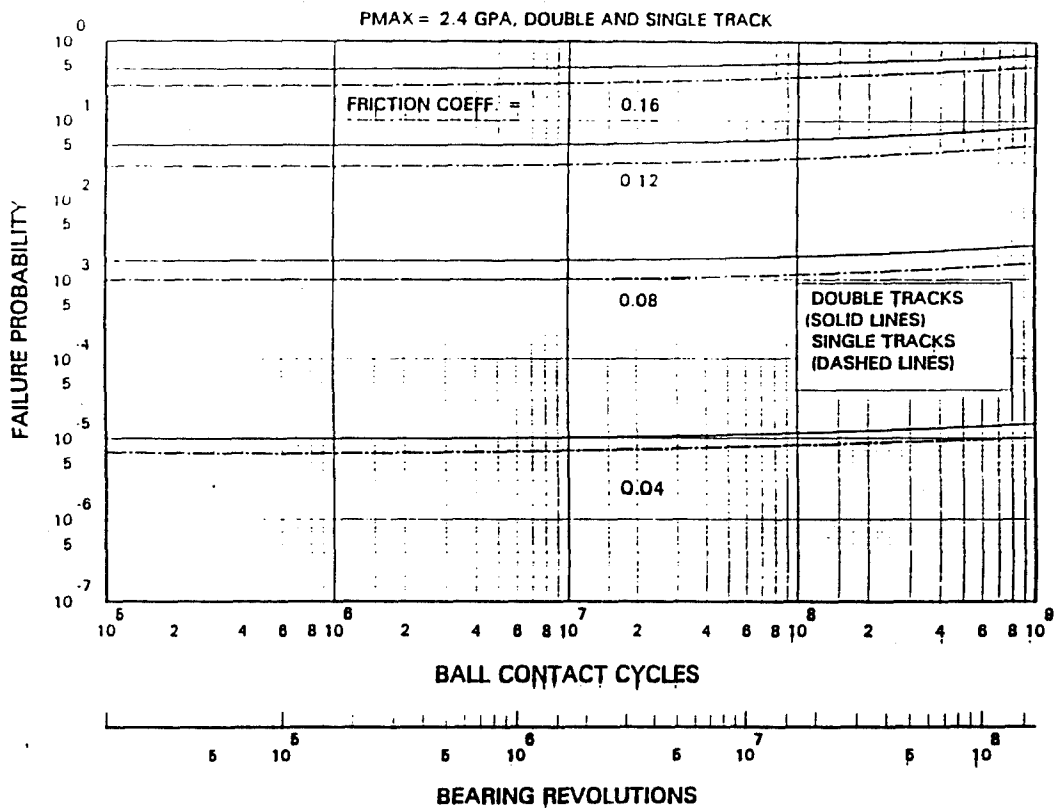


FIG. 62 Failure probability of track-forming NBD-200 (28) ball set with cycles and friction coefficients

The plots show for friction coefficients less than 0.12, as in most liquid lubricated bearings, the failure probability of the ball set (with 28 balls) is negligibly small. This means for both the materials, the hybrid bearings are almost fail-safe at the stress level of 350 ksi. This is consistent with the endurance test in the Cerbec contract with no failures (at 1100 hours) in all 12 bearings tested.

6.3.1 Hybrid Ball Bearing with Non-track Forming Ball

Under certain operating conditions, such as in bearings under fluctuating load, or radial load, there was no track formed on the ball in a ball bearing if the rotational axis of the ball relative to the bearing axis was not stationary. In this case, the stress volume spread uniformly over the entire ball surface area, rather than around the rolling track. The depth of the stress volume was assumed to be the same as that under a rolling track.

As in the preceding calculation, the maximum contact stress was 350 ksi (or 2.4 GPa). The sliding friction coefficient was assumed to be uniform throughout the contact ellipse and the direction of sliding was the same as the direction of rolling, i.e., it applied to the case of gross sliding in the bearing.

Figures 63 and 64 presented for the two baseline materials, the failure probability of the (28) ball set in the Cerbec test bearing as a function of friction coefficient and the "equivalent bearing cycles" (as abscissa). The loading on the hybrid ball bearing was the same as the preceding calculation.

The "equivalent bearing cycles" is the number of bearing revolutions to generate a (inner ring or outer ring) contact pass on a surface element on a ball.

Appendix E gives the derivation of the relation between the equivalent bearing cycles and the bearing revolution. It was shown that the number of bearing revolutions was equal to the number of equivalent bearing cycles multiplied by the following quantity

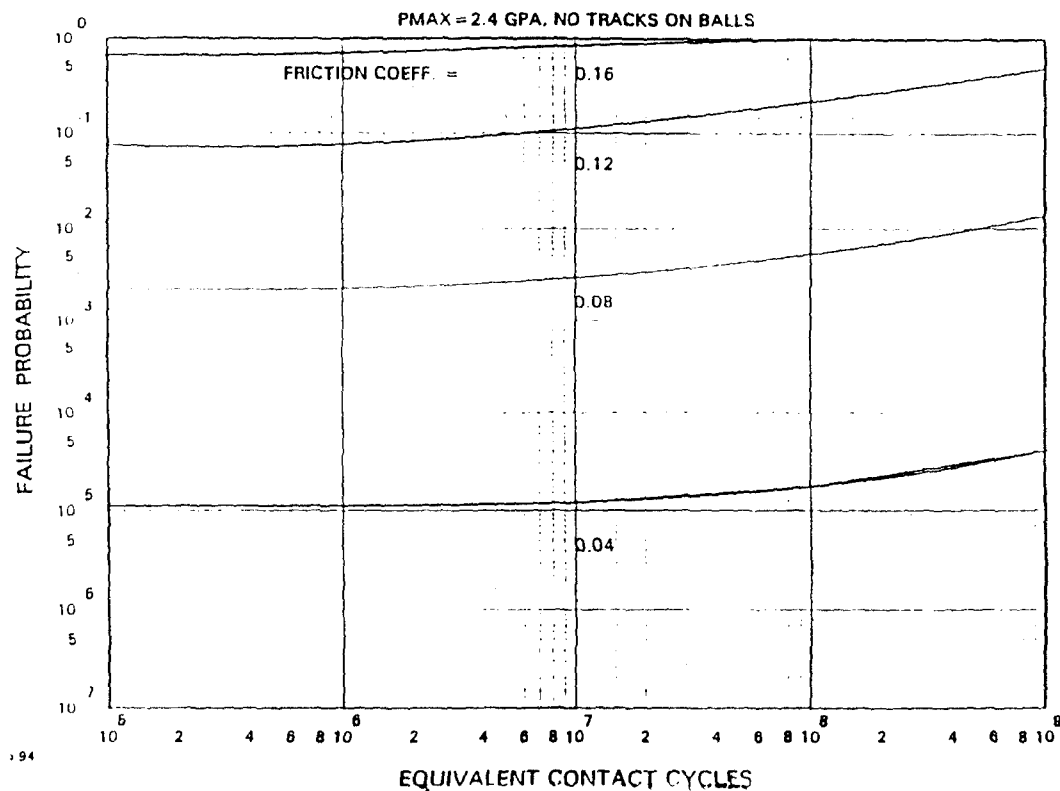


FIG.63 Failure probability of non track-forming TSN-03H (28) set with cycles and friction coefficient, at $p_{max}=2.4$ GPa

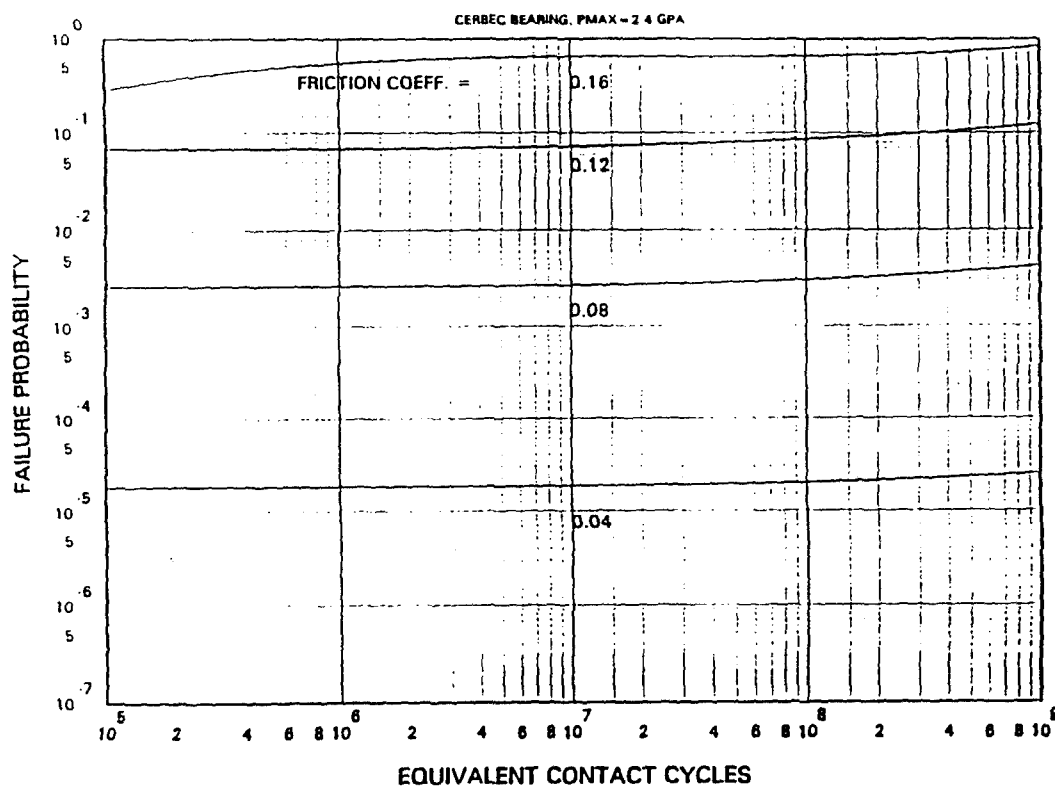


FIG.64 Failure probability of non track-forming NBD-200 (28) ball set with cycles and friction coefficients

$$2\gamma/(1-\gamma^2) A_p/A_t$$

where $\gamma = D/d_m$ is the ratio of ball diameter and pitch diameter, A_p is the ball surface area, $A_p = \pi D^2$, and A_t is the area of the rolling track in the track-forming condition. Appendix E shows that, for the pure thrust loaded Cerbec test bearings with non-track forming case, the equivalent bearing cycles (i.e., the number of bearing revolutions to generate a contact pass on an arbitrary surface element on a non-track forming ball) was 0.440 for the inner ring contact and 0.51 for the outer ring contact.

The plots show for friction coefficients less than 0.12, as in most liquid lubricated bearings, the failure probability of the ball set (with 28 balls) was negligibly small. This means that for both materials, the hybrid bearings are almost fail-safe at the stress level of 350 ksi, if the friction coefficient is kept low, i.e. <0.10 . This is consistent with the endurance test in the Cerbec's contract with no failures (at 1100 hours) in all 12 bearings tested.

6.5 Discussion of Results

At low or medium stress cycles, the failure probability was the same as that for fast fracture i.e., cracking at the contact perimeter at the first cycle of load. This probability decreased with decreasing maximum contact stress. After the stress cycling began, the failure probability was almost constant and then grew very slowly with cycles. However, after a large number of cycles, the rate of increase of failure probability increased with cycles.

For the pure thrust loaded hybrid ball bearing in the second example, the maximum contact stress was 2.4 GPa (350 ksi). The calculated failure probability for the ball set was very low, i.e., $<10^{-3}$ at the sliding friction coefficient $\mu \leq 0.10$. The analysis also shows that the failure probability of the balls having double tracks was slightly higher than that with single track, since the former involved greater stressed volume than the latter.

The method used for reliability prediction differed from the classical bearing load rating method of Lundberg and Palmgren [13]. In the latter, the failure probability of the balls or rollers was

not considered, and the critical stress in the formulation was the so-called alternating shear stress. In the present method, the failure probability of the balls was considered, and only the principal tensile stress in the contact stress field was taken into account. The similarity between the present method and [13] was that both methods assumed the material volume flaws as sources of failure.

The present analysis, based on the Hertzian contact pressure assumption, became less valid in the low Lambda regimes (i.e., thin film thickness and rough surface finish), since the contact load was carried by the micro-contact of asperities on the mating surfaces.

A previous study by Richerson et al. [44] demonstrated that friction had a strong effect on the surface tensile stress. Friction can be decreased by improvement in the surface finish and by the use of lubricant. Lower maximum contact stress can also reduce the maximum surface tensile stress.

7.0 CONCLUSIONS

Rotating Beam Fatigue Testing

1. The rotating beam fatigue test lives of the two test materials (i.e., TSN-03H and NBD-200) at constant bending stress showed wide scatter with Weibull slope less than unity.
2. The fatigue strength of the HPSN was much higher than that of the sintered silicon nitrides. The fatigue strength of the HPSN was comparable to that of a hardened bearing steel at Rc 58-59 [23].
3. Many failures in rotating beam testing were found to originate from material flaws, such as inclusions and pores. The existence of material flaws of large size (i.e., $>20\text{ }\mu\text{m}$), even in very small numbers, can greatly reduce the fatigue strength of the ceramic material. Therefore, material cleanliness should not be compromised in the advent of low cost manufacturing.
4. The rotating beam tests have shown to be a good tool for assessing the fatigue properties of ceramics, even though not all the failure origins in the fractured specimens could be identified.
5. Statistical and reliability techniques are important to achieve the material characterization for the two materials, which includes Weibull modulus, fatigue (stress-life) exponents, Weibull slope, and crack growth constant.

Hybrid Ceramic Ball Bearings

6. Hybrid bearing endurance tests at high Lambda values have produced several ball spalling failures, which have been found to not originate from the steel rings. Fractography of the spalled balls show small metallic elements (in three of the five cases) but no large material flaws (i.e., inclusions).
7. There is partial agreement in Weibull slope between the rotating beam and hybrid bearing tests. The Weibull slope of the failure probability of the NBD-200 balls based on the maximum likelihood estimate of the hybrid bearing test data is 0.24, which is close to that obtained from the rotating beam tests. However, the Weibull slope for TSN-03H balls based on bearing endurance tests is 3.1, which is an order of magnitude higher than the slope based on the rotating beam test data.

8. The predicted failure probability in ceramics under moving Hertzian load increases rapidly with maximum contact pressure and the sliding friction coefficient. Therefore, ceramic bearing and their cages should be carefully designed for low friction coefficient (via good lubrication) and moderately high contact stress in order to achieve low failure probability.

9. For hybrid ceramic ball bearings under a maximum contact pressure of 2.4 GPa (or 350 ksi), the predicted failure probability of the ball (or ball set) is extremely small, if the sliding friction coefficient ≤ 0.10 . This prediction is consistent with the hybrid bearing endurance testing by Norton/Cerbec in this ARPA Ceramic Bearing Technology Program.

8.0 RECOMMENDATIONS

The results of this project provide both valuable insight and concrete data on the interaction and fatigue performance of two key bearing-grade silicon nitride ceramics in the rotating beam fatigue test and hybrid ball bearing test. Statistical analysis as well as contact stress analysis have been applied to treat the test data as well as to predict the performance of the ceramic components. Nevertheless, some results, such as the bearing test data and the reliability prediction of rolling contact components, have served to create additional questions regarding the assumptions used in the analysis as well as the most realistic operating conditions. Building on the experience gained from this program, more studies and experiments are needed to further explore this technology on cyclic fatigue of advanced ceramics as well as to demonstrate the usefulness of the analytical procedures developed in this program. Therefore, the following recommendations are made:

- A new series of hybrid ball bearing endurance tests be performed at different (or multiple) loads to determine the load-life relationship for hybrid bearings using clean and contaminated oils.
- Develop the most economical (in terms of sample size) test procedure in rotating beam tests and hybrid bearing tests, using the statistical procedure developed in the present project.
- Explore the effect of compressive stress in the rolling contact material on its failure probability under given loading conditions.
- Extend the reliability prediction of rolling components developed in this project to rolling contacts with marginal lubrication.
- Include the steel rolling contact members in the life prediction calculation of hybrid ceramic bearings, taking into account lubrication and friction parameters.
- Rotating beam fatigue testing be performed at an elevated temperature to obtain material characterization of this HPSN at high temperature. This is necessary since many future applications of hybrid or full ceramic bearings in critical military components involve elevated temperature.

- Explore the optimum profiles of bearing rolling elements which will produce lowest surface tensile stress with and without friction traction.
- Perform rotating beam tests using steel and ceramic specimens with diamond indentations on the gage sections to explore the effect of debris contamination denting on bearing lives.

9.0 REFERENCES

1. Ebert, F., "Ceramics - A Rolling Bearing Material for More Demanding Aerospace Application", Proceeding of International Rolling Element Bearing Symposium '91, Orlando, FL, April 1991.
2. Katz, R. N. and Hannoosh, J. G., "Ceramic for High Performance Rolling Element Bearings: A Review and Assessment", International J. High Technology Ceramics, **1**, (1985), pp. 69-79.
3. Zaretsky, E.V., "Ceramic Bearings for Use in Gas Turbine Engines", Trans. ASME, Vol. 111, January 1989, pp. 146-157.
4. Morrison, F. R., McCool, J. I. and Yonushonis, T., "The Load-Life Relationship for M50 Steel Bearings with Silicon Nitride Ceramic Balls", Lubrication Engineering, Vol. 40, No. 3, pp. 153-159.
5. Lucek, J., "Rolling Wear of Silicon Nitride Bearing Materials", ASME Paper No. 90-GT-165, June 1990.
6. Baumgartner, H. R. and Cowley, P. E., "Silicon Nitride in Rolling Contact Bearings", Final Report, Contract N00019-74-C-0157, Norton Company, March-July 1975.
7. Katz, R. N., "Effects of Composition, Microstructure and Processing on Ceramic Rolling Element Bearing Performance", (1991), NIST Special Publication No. 824, Ceramic Bearing Technology, Ed. by S. Jahanmir, pp. 121-130.
8. Duffy, P. E., "Exploratory Testing and Analysis of Full Ceramic Ball Bearings", SAE Paper No. 911800.
9. Monnot, J., Hertier, B. and Cogne, J., "Relationship of Melting Practice, Inclusion Type and Size with Fatigue Resistance of Bearing Steels", ASTM-STP 987, Ed. by J. J. Hoo, pp. 149-165, (1988).
10. Ionnides, E. and Harris, T. A., "A New Fatigue Life Model for Rolling Bearings", ASME J. Tribology, July 1985, p. 367.
11. Ko, H. N., "Fatigue Strength of Sintered Si₃N₄ Under Rotary Bending", J. Material Science Letters **6** (1987) pp.175-177.
12. Masuda, M., Yamada, N., Soma, T. and Oda I., "Fatigue of Ceramics, (Part 2) - Cyclic Fatigue Properties of Sintered Si₃N₄ at Room Temperature", J. Ceramic Society of Japan, Vol. 97, 1989, pp. 509-514.

13. Lundberg, G. and Palmgren, A., "Dynamic Capacity of Rolling Bearings", Acta Polytechnica, 1947.
14. Mechanical Technology Inc. Technical Report No. MTI191TR20, Bearing Industry Technology Modernization Report, Final Report--Vol. 8, "Ceramic Material Characterization", Contract F33657-86-C-0096, January 1992.
15. Gardos, M. N., "Determination of the Tribological Fundamentals of Solid Lubricated Ceramics", Vol.1: Summary, Final Report, WRDC-TR-90-4096.
16. Hild, F. and Marquis, D., "Monotonic and Cyclic Rupture of a Silicon Nitride Ceramic", in ASTM Sp. Publ. -1202 Life Prediction Methodologies and Data for Ceramic Materials.
17. Liu, C. K. and Brinkman, C. R., "Cyclic Fatigue of Toughened Ceramics", Technical Report No. ORNL/TM-10838, Oct. 1987-Mar., 1988, pp. 294-300.
18. Liu, Shih-Yu and Chen, I. W., "Fatigue of Yttria-stabilized Zirconia, I. Fatigue Damage, Fracture Origin and Lifetime Prediction", J. Am. Ceram. Soc., 74 (6), 1991, pp. 1197-1205.
19. Military Handbook MIL-HDBK-790, "Fractography and Characterization of Fracture Origins in Advanced Structural Ceramics", July 1992, published by U.S. Army Material Technology Laboratory, Watertown, MA.
20. Richerson, D. W., "Modern Ceramic Engineering", Marcel Dekker, Inc. 1982, pp. 328-345.
21. Chen, Z., Mecholsky, J. J., Chiu, Y. and Pearson, P., "Fractography Study of Rolling Specimens of Silicon Nitride", presented at the American Ceramic Society Annual Meeting, Indianapolis, April, 1994.
22. ASM Metals Handbook, Vol. 8, 9th edition.
23. Chidester, A., Green, W. B. and Corbo, K., "High-Hardness, High-Density Powder Metal Bearing Applications", in ASTM STP-1195, Creative Use of Bearing Steels, pp. 106-120, 1993.
24. Abernethy, R. B. et al., "Weibull Analysis Handbook", November 1983, AFWAL-TR-83-2079, AD-A 143 100, pp. 184-189.
25. McCool, J. I., "Using Weibull Regression to Estimate the Load Life Relationship for Rolling Bearings", presented in the 1984 ASLE-ASME Joint Lubrication Conference at San Diego, Ca.

26. Batdorf, S. B. and Heinisch, H. L., "Weakest Link Theory Reformulated for Arbitrary Fracture Criterion", J. Am. Ceramic Soc, July-Aug. 1978, p. 355.
27. Batdorf, S. B. and Crose, J. G., "A Statistical Theory for the Fracture Subjected to Non-Uniform Polyaxial Stresses", J. Applied Mechanics, June 1974, p. 459-464.
28. Chao, L. Y. and Shetty, D. K., "Reliability Analysis of Structure Ceramics Subjected to Biaxial Flexure", J. Am Ceramic Soc., 74 (2),1991, pp. 333-44.
29. Kobayashi, H., "Evaluation of Fatigue", Stress Corrosion Crack Properties of Ceramics, published in HEISEI SAN HENDO KAGAKU KENKYUHI HOJOKIN, Mar. 92, pp. 51-57.
30. Sturmer, G., Schutz, A. and Wittig, S., "Lifetime Prediction for Ceramic Gas Turbine Components", ASME J. Engineering for Gas Turbine and Power, Vol. 115, Jan. 1993, pp 70-75.
31. Nemeth, N. N. and Gyekenyesi, J. P., "Probabilistic Design of Ceramic Components with the NASA/CARES Computer Program", Handbook of Glass and Ceramics, an SAE publication, 1992, pp. 700-708.
32. Jones, A. B., "A General Theory for Elastically Constrained Ball and Radial Roller Bearings Under Arbitrary Load and Speed Conditions", Trans. ASME, J. Basic Engrg., Vol. 82, Series D, No.2, June 1960.1.
33. NSK Publication: NSK Precision Ceramic Angular Contact Bearing, Bearing Catalog.
34. Ellingson, W., "NDI/NDE Techniques for Ceramics", CTIP 1993 Ceramic Bearing Technology Annual Meeting, Annapolis, Md., Meeting Notes.
35. Lawn, R. B., "Fracture of Brittle Solid", Second Edition, Cambridge Press, 1993.
36. Johnson, K. L., "Contact Mechanics", Cambridge University Press, 1983, p. 99.
37. Lure, A. I., "Three Dimensional Theory of Elasticity", 1961.
38. Lundberg, G. and Sjoval, H., "Stress and Deformation of Elastic Contacts", Pub. No.4, Chalmers University of Technology, Gothenburg, 1958.
39. Bryant, M. D. and Keer, L. M., "Rough Contact Between Elastically and Geometrically Identical Curved Bodies", Journal of Applied Mechanics., June 1982, Vol. 49, pp. 345-352.

40. Dalal, H., Chiu, Y. and Rabinowicz, E., "Evaluation of Hot Pressed Silicon Nitride as a Rolling Bearing Material", ASLE Trans., Vol.18, No.3, pp. 211-221. (1975).
41. Glover, D., "A Ball-Rod Rolling Contact Fatigue Tester, in Rolling Contact Fatigue Testing of Bearing Steels", ASTM STP 771, J.J.C. Hoo, Ed., 1982, pp. 107-124.1.
42. Lucek, J., Cerbec Inc., private communication.
43. Chiu, Y. P., Martin, J. A. and McCool, J. I., "Development of A Mathematical Model for Predicting Life of Rolling Bearings", Rome Air Development Center (AFSC) Technical Report No. RADC-TR-68-54, April 1968, Appendix 1.
44. Richerson, D. W., Carruthers, W. D. and Jindberg, L. J., "Contact Stress and Coefficient of Friction Effects on Ceramic Interfaces, Surfaces and Interfaces in Ceramics and Ceramic-Metal Systems", edited by J. Pask and A. Evans, Plenum Press, 1980, pp. 661-678.
45. Burk, C., ARPA Ceramic Bearing Technology Meetings Proceedings, May 26 & 27, Baltimore, Maryland, 1994.

APPENDIX A

TABULATION OF ROTATING BEAM TEST DATA

ROTATING BEAM FATIGUE TEST DATA

LEGEND:

COLUMN

- (1) Specimen ID number
 - (2) Test machine ID number
 - (3) Surface finish index number
 - (1. better than sample quality, 2. sample quality
 - 3. lower than sample quality 4. slight scratchy)
 - (4) Bending moment (in-lbs)
 - (5) Maximum stress (ksi)
 - (6) Date of test (start)
 - (7) Date of test (end)
 - (8) hour/minute of start time
 - (9) test cycles at end
 - (10) mode of test at end
-

(1)	(2)	(3)	(4)	(5)	(6)	(7)	(8)	(9)	(10)
A55	1	2	47	72	10.30	11.11	1145	104233200	S
A44	2	2	70	109	11.04	11.05	1540	7700000	S
A44	2	2	80	123	11.05	11.05	1000	2708100*	F
A31	2	4	80	123	11.06	11.06	1020	31900	F
A39	3	1	56	87	11.06	11.07	1620	1634900	F
A48	2	2	56	87	11.06	11.16	1605	103928500	S
A37	3	1	80	123	11.09	11.10	1420	1903300	F
A46	4	2	70	109	11.09	11.09	1445	1	FF
A34	4	4	70	109	11.09	11.09	1320	31600	F
A8@	4	1	70	109	11.10	11.10	1000	1	FF
A11@	3	1	80	123	11.10	11.10	1000	42300	F
A13	4	1	70	109	11.10	11.17	1115	75160900	S
A65	3	4	71	110	11.10	11.17	1540	67500500	S
A14	1	1	80	123	11.11	11.11	1600	1	FF
A22@	1	1	80	123	11.12	11.12	0940	1	FF
A18@	1	1	80	123	11.12	11.12	1100	396600	F
A4	1	4	75	116	11.13	11.13	1040	514800	F
A15	1	1	55	87	11.13	11.17	1335	37975400	S
A21	2	1	60	94	11.16	11.20	1100	36239000	S
A16	3	1	65	101	11.17	11.23	1355	55218600	S
A38	1	3	70	108	11.17	11.18	1430	3331300	F

ROTATING BEAM FATIGUE TEST DATA (CONT'D)

(1)	(2)	(3)	(4)	(5)	(6)	(7)	(8)	(9)	(10)
A6@	4	1	75	116	11.17	11.18	1515	3466800	F
A45	4	3	80	123	11.19	11.19	1030	1	FF
A42	4	3	55	87	11.19	11.23	1030	39562700	S
A52	1	1	60	94	11.19	11.23	1200	36163700	S
A58	2	2	65	101	11.20	11.24	1600	36170500	S
A53	4	2	70	108	11.23	11.30	1030	68964800	S
A54	1	2	75	116	11.23	11.24	1130	2914700	F
A57	1	3	80	123	11.18	11.19	1100	1	FF
A56	3	2	80	123	11.23	11.23	1245	207300	F
A61@	3	2	60	94	11.23	11.24	1500	3964200	F
A66	1	2	65	101	11.24	12.02	1000	36133200	S
A67	3	2	70	108	11.24	11.24	1055	249800	F
A63	3	2	75	116	11.14	11.24	1355	408900	F
A59	2	2	55	87	11.25	11.30	0900	47317200	S
A64	3	2	60	94	11.25	11.30	1030	6092500	F
A49	3	2	65	101	11.30	12.01	1100	401800	F
A47	4	2	75	116	11.30	12.01	1100	5840300	F
A10	2	2	60	94	11.30	21.04	1245	36318500	S
A9	3	2	65	101	11.30	21.04	1310	40093700	S
A17	4	2	75	116	12.01	12.01	1000	190200	F

ROTATING BEAM FATIGUE TEST DATA (CONT'D)

(1)	(2)	(3)	(4)	(5)	(6)	(7)	(8)	(9)	(10)
A12	3	2	65	101	12.14	12.14	1107	756300	F
A27	3	2	65	101	12.15	12.15	0915	1410400	F
A26	3	2	65	101	12.15	12.15	1440	221000	F
A29	3	2	65	101	12.15	12.16	1540	10144000	S
A29	3	2	70	108	12.16	12.17	1540	9833000 *	S
A29	3	2	80	123	12.10	12.10	1540	440500*	F
A51	2	2	65	101	1.05	1.06	1000	7709500	F
A43	3	2	70	108	1.05	1.05	1100	9800	F
A68	3	2	70	108	1.05	1.05	1125	460000	F
A70	3	2	60	94	01.06	01.08	1250	20780200	S
A70	3	2	70	108	01.08	01.10	1510	975500*	F
A60@	2	2	55	87	01.07	01.11	1040	34800000	S
A60	2	2	75	116	01.11	01.11	1120	9102300*	F
A62	4	2	65	101	01.12	01.12	1110	1	FF
A69@	4	2	65	101	01.12	01.14	1130	20254100	S
A69	4	2	80	123	01.14	01.14	1126	591800*	F
A50	3	2	65	101	01.20	01.22	1245	23450000	S
A50	3	2	75	116	01.22	01.25	1500	33373500*	S
A50	3	2	80	123	01.25	01.26	1545	8419900*	F
A28	4	2	65	101	01.20	01.22	1300	23788000	S
A28	4	2	75	116	01.22	01.25	1505	2091000*	F
A5@	2	2	65	101	01.20	01.22	1310	23399600	S
A5	2	2	75	116	01.22	01.25	1510	41207400*	S

ROTATING BEAM FATIGUE TEST DATA (CONT'D)

(1)	(2)	(3)	(4)	(5)	(6)	(7)	(8)	(9)	(10)
A5	2	2	80	123	01.25	01.26	1600	614500*	F
A3@	3	2	65	101	02.08	02.09	1535	639800	F
A7@	1	2	65	101	02.08	02.09	1540	349200	F
A20@	3	2	65	101	02.10	02.12	1335	20030200	S
A20	3	2	70	108	02.12	02.16	1320	26881000*	S
A20	3	2	80	123	02.16	02.16	0900	311900*	F
A19@	3	2	65	101	02.16	02.16	1230	365600	F
A23@	3	2	55	87	02.26	03.01	0800	7354800	F
A24	1	2	55	87	03.01	03.03	1116	20488100	S
A24	1	2	60	94	03.03	03.05	1116	19674100*	S
A24	1	2	75	116	03.05	03.08	0835	31690100*	S
A25	3	2	55	87	03.01	03.04	1255	24314200	S
A25	3	2	60	94	03.04	03.08	0820	32886100*	S
A25	3	2	75	116	03.08	03.10	0756	20029800*	S
A72	2	2	55	87	03.03	03.05	1112	220122200	S
A72	2	2	60	94	03.05	03.08	1600	224356000*	S
A72	2	2	75	116	03.08	03.08	0802	619300*	F

ROTATING BEAM FATIGUE TEST DATA (CONT'D)

(1)	(2)	(3)	(4)	(5)	(6)	(7)	(8)	(9)	(10)
B8	3	2	60	94	12.01	12.07	1445	65182600	S
B64	1	2	65	101	12.03	12.07	0930	39114800	S
B57	3	2	70	108	12.06	12.08	0930	40784500	S
B40	2	2	75	116	12.06	12.06	1330	1	FF
B35	1	1	80	123	12.07	12.08	1450	1639600	F
B62	2	2	55	87	12.06	12.10	1350	36656200	S
B27	4	1	75	116	12.07	12.08	1345	3225100	F
B60	1	2	75	116	12.08	12.08	1515	1.	FF
B71	3	2	70	108	12.11	12.11	1030	31500	F
B28@	3	2	75	116	12.11	12.11	1130	38000	F
B33	2	1	77	119	12.11	12.11	1230	1.	FF
B36	2	2	70	108	12.11	12.15	1345	36094200	S
B65	2	2	60	94	12.06	12.10	1230	17577000	S
B65	2	2	70	108	12.10	12.10	1010	1124400*	F
B53	3	2	65	101	12.08	12.10	1330	18030000	S
B53	3	2	75	116	12.10	12.10	1015	270100*	F
B63	4	2	70	108	12.06	12.10	1415	19456000	S
B63	4	2	75	116	12.10	12.14	1025	22688000	S

ROTATING BEAM FATIGUE TEST DATA (CONT'D)

(1)	(2)	(3)	(4)	(5)	(6)	(7)	(8)	(9)	(10)
B67@	1	2	55	87	12.08	12.10	1515	15510000	S
B67	1	2	70	108	12.10	12.14	1035	34179000*	S
B67	1	2	75	116	12.14	12.19	1031	43000000*	F
B30	2	2	75	116	12.15	12.17	1500	10262400	F
B34	2	2	80	123	12.15	12.18	1400	2000	F
B20	2	1	75	116	12.18	12.18	1445	314800	F
B4	2	2	77	119	12.21	12.21	1020	8200	F
B31	2	1	75	116	12.21	12.21	1020	9100	F
B6	3	3	75	116	01.04	01.04	1045	870300	F
B18	1	2	72	111	01.04	01.09	1150	44120600	S
B18	1	2	80	123	01.09	01.11		3053500	F
B15@	2	2	80	123	01.04	01.04	1452	11800	F
B69	2	2	75	116	01.04	01.04	1555	1406500	F
B70	4	3	77	119	01.05	01.05	1615	10100	F
B45	4	2	77	119	01.07	01.08	1245	1905800	F
B47	3	2	80	123	01.12	01.12	1300	17900	F
B61	1	2	65	101	01.14	01.19	1000	23000000	S
B61	1	2	75	116	01.19	01.25	1015	58840000*	S
B61	1	2	80	123	01.25	01.26	1530	1057400*	F
B39@	3	1	65	101	01.29	02.01	0915	30176300	S
B39	3	1	75	116	02.01	02.01	0915	2721100*	F

ROTATING BEAM FATIGUE TEST DATA (CONT'D)

(1)	(2)	(3)	(4)	(5)	(6)	(7)	(8)	(9)	(10)
B32	1	1	65	101	01.29	02.01	0940	30625800	S
B32	1	1	75	116	02.01	02.03	0915	30527100*	S
B51@	2	2	65	101	01.29	02.01	0947	26945000	S
B51	2	2	75	116	02.01	02.03	0918	18334100*	S
B51	2	2	80	123	02.03	02.06	0919	32344700*	F
B26@	4	2	65	101	01.29	02.01	0935	31523500	S
B26	4	2	75	116	02.01	02.03	0910	21483700*	S
B26	4	2	80	123	02.03	02.03	0910	51400*	F
B41	3	1	70	108	02.02	0202	1030	1	FF
B54@	4	1	70	108	02.03	02.03	1240	1086300	F
B3	3	2	65	101	02.01	02.01	1320	462000	F
B42	3	1	70	108	02.02	02.04	1045	20962000	S
B42	3	1	80	123	02.04	02.04	1345	30900*	F
B49@	4	1	70	108	02.05	02.08	1550	26532800	S
B49@	4	1	80	123	02.08	02.08	0900	1100*	F
B48@	3	1	70	108	02.05	02.05	1535	8900	F
B43@	2	1	65	101	02.08	02.08	1540	1	FF

ROTATING BEAM FATIGUE TEST DATA (CONT'D)

(1)	(2)	(3)	(4)	(5)	(6)	(7)	(8)	(9)	(10)
B56@	2	1	65	101	02.08	02.08	1550	1500	F
B66	2	1	65	101	02.08	02.11	1605	22314000	S
B66	2	1	70	108	02.11	02.16	1605	23697900*	F
B12	4	2	70	108	02.09	02.09	1350	8300	F
B13	4	2	65	101	02.09	02.11	1415	20115800	S
B13	4	2	70	108	02.11	02.16	1603	40680000*	S
B13	4	2	80	123	02.16	02.16	0915	958700*	F
B22	3	2	65	101	02.09	02.10	1425	4391900	F
B21	1	3	65	101	02.09	02.11	1445	20108300	S
B21	1	3	70	108	02.11	02.16	1632	46488700*	S
B21	1	3	80	123	02.16	02.17	0910	2890000*	F
B9	1	2	60	94	02.22	02.24	1100	20250100	S
B9	1	2	70	108	02.24	02.26	1150	19802100*	S
B9	1	2	80	123	02.26	03.01	0800	30318000*	S
B10	2	1	60	94	02.22	02.24	1120	20370200	S
B10	2	1	70	108	02.24	02.26	1030	19975000*	S
B10	2	1	80	123	02.26	03.01	0830	16100*	F
B29	3	3	60	94	02.22	02.24	1300	20220100	S
B29	3	3	70	108	02.24	02.26	1035	21369000*	S
B29	3	3	80	123	02.26	02.26	0835	397100*	F
B7	2	2	60	94	02.26	03.01	0950	24618200	S
B7	2	2	70	108	03.01	03.01	2065	3996500*	F

ROTATING BEAM FATIGUE TEST DATA (CONT'D)

(1)	(2)	(3)	(4)	(5)	(6)	(7)	(8)	(9)	(10)
B23@	2	3	55	87	03.08	03.10	1325	20125200	S
B23	2	3	60	94	03.10	03.12	1424	20092400*	S
B23	2	3	75	116	03.12	03.12	1538	60700*	F
B24@	3	3	55	87	03.10	03.12	1420	230040100	S
B24	3	3	60	94	03.12	03.15	1632	22535100*	S
B24	3	3	75	116	03.15	03.15	0924	18900*	F
B25	3	3	80	123	03.15	03.15	1550	74400	F
B44	1	3	80	123	03.16	03.16	1105	152200	F
B38	1	3	75	116	03.18	03.19	1434	8560300	F
B46@	3	3	75	116	03.18	03.18	1532	1	FF
B50	3	3	75	116	03.18	03.21	1556	28987600	F
B14&	1	3	55	87	03.08	03.08	1045	1	FF
B17	1	3	55	87	03.08	03.10	1122	20427300	S
B17	1	3	60	94	03.10	03.12	1008	20618100*	S
B17	1	3	75	116	03.12	03.12	0828	154000*	F
B37	1	2	70	108	12.18	12.23	0830	30000000	S
B37	1	2	80	123	12.23	12.23	0840	388600*	F

F : Fatigue fracture
FF: fast fracture in setup
S : suspension (runout)
* : test with specimen survived from test at lower stress levels.
@ : sent to University of Florida (AFOSR Program)
& : sent to Norton/Cerbec (ARPA Program)

APPENDIX B

MAXIMUM LIKELIHOOD ANALYSIS FOR MULTIPLE LOAD TESTS

APPENDIX B
MAXIMUM LIKELIHOOD METHOD
FOR WEIBULL ANALYSIS WITH PARAMETERS β AND n
FOR TESTS WITH MULTIPLE STEP LOADING

Let $F(x)$ be the probability that a unit will fail before it acquires x units of operating cycles.

$$F(x) = 1 - \exp \left[- \left(\sum_{j=1}^J x_j \sigma_j^n / x_0 \right)^\beta \right]$$

where

β = the Weibull slope

n = the stress - life exponent

x_0 = a scale parameter

j = load step index

J = number of maximum load step

The probability distribution function $f(x_i) = dF(x)/dx_{ij}$ is given by

$$f(x_i) = \beta \sigma_{ij}^n / x_0^\beta (x_{ij} \sigma_{ij}^n)^{\beta-1} \exp \left[- \left(\sum x_{ij} \sigma_{ij}^n / x_0 \right)^\beta \right]$$

where

i = specimen index number

σ_{ij} = the stress level of the i th specimen and j -th load step.

x_{ij} = number of stress cycles for the i -th specimen at the j -th load step.

When r samples run to failure and the remaining k units are unfailed (or suspended), the likelihood function for the censored samples (where not every unit has run to failure) is given by

$$L = \prod_{i=1}^r f(x_i) \prod_{j=1}^k [1 - F(T_j)]$$

where

r = number of units run to failure
 k = number of unfailed units
 $x_1, x_2, x_3, \dots, x_r$ = known failure cycles
 T_1, T_2, \dots, T_k = operating time for each unfailed unit.

The maximum likelihood method finds the values of β , n and x_0 , which maximize the likelihood function L . In practice, it is more convenient to maximize the quantity $\ell n(L)$.

Letting

$$\ell = \sum_{i=1}^n \ell n f(x_i) = r \ell n \beta + n \sum_{i=1}^r \ell n \sigma_{ij} - \beta r \ell n x_0 + (\beta-1) \sum_{i=1}^r \ell n Y_i - \sum_{i=1}^n (Y_i/x_0)^\beta$$

where

$$Y_i = \sum_{j=1}^J x_{ij} \sigma_{ij}^n$$

$$Z_i = \sum_{j=1}^J x_{ij} \sigma_{ij}^n \ell n \sigma_{ij}$$

By differentiating the logarithm of the likelihood function L with respect to β , n and x_0 and setting to zeros as follows:

$$\partial \ell / \partial \beta = r/\beta - r \ell n x_0 + \sum_{i=1}^r \ell n Y_i - \sum_{i=1}^n (Y_i/x_0)^\beta \ell n(Y_i/x_0) = 0$$

$$\partial \ell / \partial x_0 = -r\beta/x_0 + \beta x_0^{-\beta-1} \sum_{i=1}^n Y_i^\beta = 0$$

$$\partial \ell / \partial n = \sum_{i=1}^r \ell n \sigma_{ij} + (\beta-1) \sum_{i=1}^r (Z_i/Y_i) - \beta x_0^{-\beta} \sum_{i=1}^r Z_i Y_i^{\beta-1} = 0$$

The three unknowns, i.e., β , n and x_0 are to be solved from the above three equations using a nonlinear equation solver.

The unknown x_0 is to be solved from

$$x_0 = [\sum Y_i^\beta / r]^{1/\beta}$$

APPENDIX C
EFFECTIVE STRESS VOLUME OF RBF SPECIMENS

Appendix C

Formulas for Effective Stress Volume and Stressed Area for a Rotating Beam Specimen

The effective stressed volume $V_{\text{eff}} = \int (\sigma/\sigma_f)^m dV$

The effective stressed area $S_{\text{eff}} = \int (\sigma/\sigma_f)^m dS$

where dV and dS are respectively the elemental volume and surface area of the specimen at the neck down section.

σ is the stress in the axial direction of the specimen under bending and σ_f is the maximum tensile stress in the specimen.

$$dV = 2\pi r dr dz, \quad dS = 2\pi R dz / \cos\theta$$

where r, z are the coordinates in the cylindrical coordinate system with its origin at the center of the specimen. $R = R(z)$ is the outer radius of the specimen. θ is the angle between the z -axis and the tangent at surface on the r - z plane.

Note that

$$R = R_0 + R_c - (R_c^2 - z^2)^{1/2}$$

and using

$$z = R_c \sin\theta, \quad dz = R_c \cos\theta d\theta$$

where R_0 is the value of R at $z=0$, the center of the specimen and R_c is the radius of the profile.

The stresses are expressed by

$$\sigma = M r / I, \quad \sigma_f = M_0 R_0 / I_0$$

Using the approximation that $M \approx M_0$ and $I/I_0 = (R/R_0)^4$

$$\sigma/\sigma_f = R_0^3 r/R^4$$

Thus,

$$\begin{aligned}
 V_{\text{eff}} &= \int (\sigma/\sigma_f)^m dV = 2\pi r_{03m} \int \int R^{-4m} r^{m+1} dr dz = \\
 &= 2\pi R_{03m}/(m+2) \int dz/R^{3m-2} = 2\pi R_c/(m+2) \int \cos\theta R^2(R_0/R)^{3m} d\theta \\
 S_{\text{eff}} &= \int (\sigma/\sigma_f)^m dS = 2\pi R_{03m} \int R^{m+1}/R^{4m} dz/\cos\theta = \\
 &= 2\pi R_c \int R (R_0/R)^{3m} d\theta
 \end{aligned}$$

The above two integrals can be integrated for the range $-\theta_0$ to θ_0 using Gaussian quadrature technique.

APPENDIX D
FAFNIR BEARING TEST LABORATORY
HYBRID BEARING TESTING REPORT

FAFNIR BEARINGS DIVISION ENGINEERING TEST REPORT

Subject: **PERFORMANCE OF TWO LOTS OF MMV206K4 FS649A
HYBRID BEARINGS WITH DIFFERENT CERAMIC BALL
MANUFACTURERS**

Reference:

Report No: 1712 L268

Date: July 22, 1993

Requested By: Y.P. Chiu

Conducted By: K. Galitello/H. Daverio

Approved By: H. Daverio

Copies To	Critically Restricted	<i>Restricted</i>	Internal Use	General
<div style="border: 1px solid black; height: 500px; width: 100%;"></div>	<p><u>OBJECT:</u></p> <p>Perform testing for DARPA/U.S. Air Force under Contract #F33615-92-C-5910 to determine the performance of two lots of MMV206K4 FS649A hybrid bearings. The first lot assembled with CERBEC NBD-200 Silicon Nitride balls, and the second lot assembled with Toshiba TSN-03H Silicon Nitride balls.</p> <p><u>CONCLUSIONS:</u></p> <p>Testing of four CERBEC NBD-200 groups resulted in one group with a bearing failure at 13.6 hours due to a spalled ball. The remaining three groups were suspended with no failure at over 1,500 hours. No Weibull plot was performed due to only one failure in this lot.</p> <p>Testing of four Toshiba TSN-03H groups resulted in a failure in each group with 50.1 hours, 142.3 hours, 173.2 hours and 183.2 hours. A Weibull plot shows an L10 of 124.2 hours, which is 3.9 times the calculated life of 31.5 hours. (See Figure 65).</p> <p style="margin-top: 100px;">K. Galitello H. Daverio</p>			

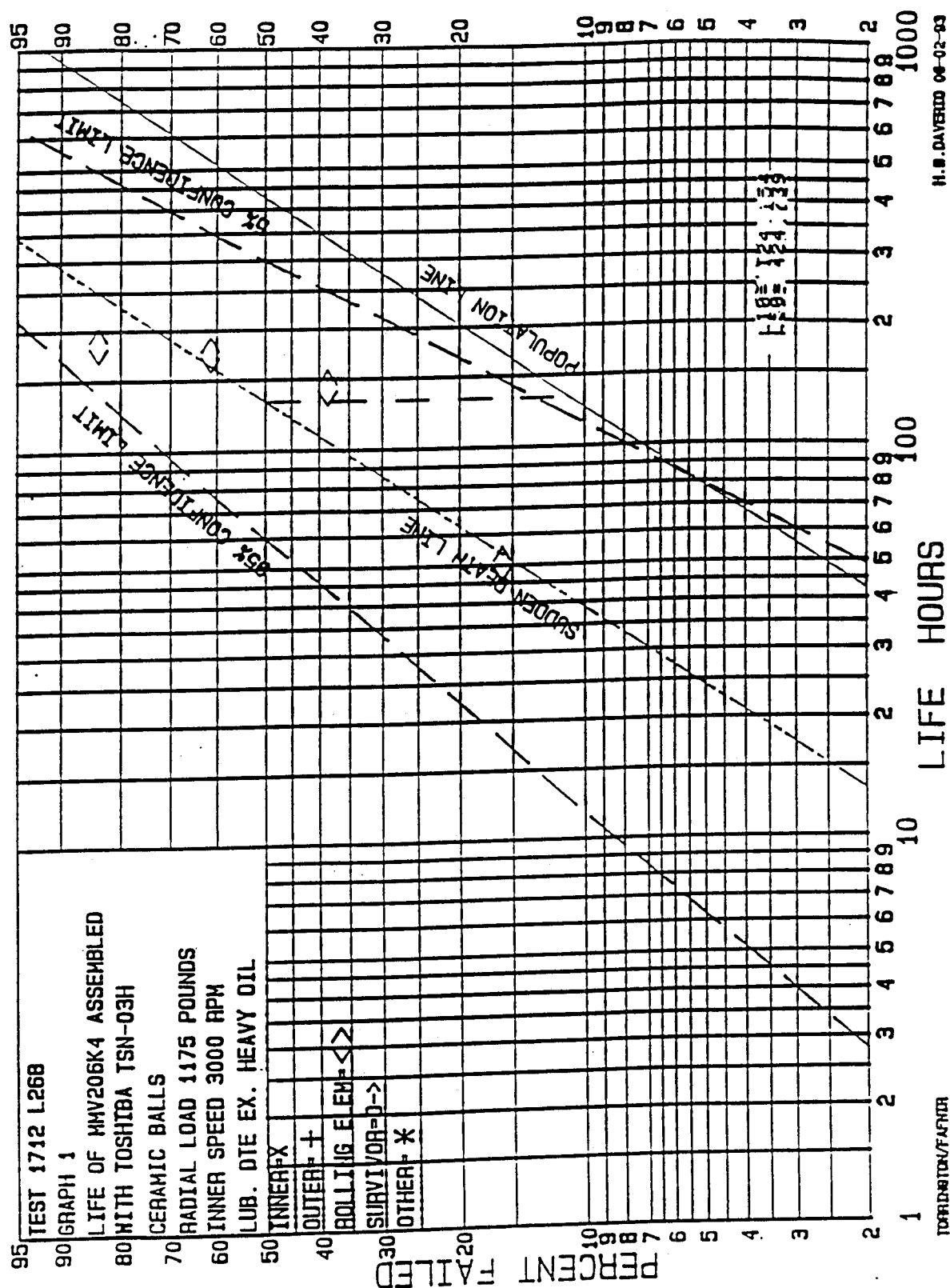


FIG. 65 Weibull Plot of Failure Probability of Hybrid

RESULTS:

Results of testing four groups of six bearings per group for each lot of MMV206K4 FS649A bearings assembled with CERBEC NBD-200 and MMV206K4 FS649A bearings assembled with Toshiba TSN-03H Silicon Nitride balls is shown in Tables 19 and 20.

All bearing failures were due to spalling of the ceramic balls. There were no failures in any of the bearing rings. One bearing in the Toshiba group experienced four spalled balls, which may have been due to the shutoff setting on the test rig vibration shutoff device (Robertshaw Model 366 Vibraswitch Malfunction Detector). All other bearing failures were due to one spalled ball in each bearing.

Ball Manufacturer	# Bearings Tested	# Bearings Failed
CERBEC	24	1
Toshiba	24	4

A Weibull Graph for the Toshiba lot is shown in Figure 65 (L10 = 124 hours), while a Weibull Graph was not plotted for the CERBEC lot due to only one bearing failure.

DETAILS:

Bearing type MMV206K4 FS649A inner and outer rings were received and inspected for inner and outer race manufacturing surface defects. Twenty-four bearings were assembled with CERBEC NBD-200 Silicon Nitride balls and 24 bearings assembled with Toshiba TSN-03H Silicon Nitride balls.

Bearing bore, O.D. and radial play were measured and recorded along with ball manufacturer, ball diameter, shaft diameter and housing bore for all test bearings. Results are shown in Tables 21 and 22.

Bearings, housings and shafts were ultrasonically cleaned then lubricated before testing. Bearings were pressed onto the test shaft with an average interference fit of 0.0003". Housings were slip fit onto the bearings with 0.0004" clearance. Oil caps were placed to secure the outer ring from rotation and provide lubrication to the bearings.

1712.TLR:kms

TABLE 19

Test Lives of Hybrid Bearing with NBD-200 Balls
 MMV206K4 FS649 Hybrid Bearing
 Speed: 3,000 rpm
 Radial Load: 1,175 lbs.
 Lube: 0.09 gal./min. of Mobil DTE Extra Heavy Oil
 Ball & Inner Race Contact Stress: 515.2 ksi
 Calculated L10 = 31.5 hours

Group	Bearing #	Hours Run	Post-run Condition
1	527-92	1,509.9	Suspended
	528-92	1,509.9	Suspended
	529-92	1,509.9	Suspended
	530-92	1,509.9	Suspended
	531-92	1,509.9	Suspended
	532-92	1,509.9	Suspended
2	533-92	17.9	Suspended
	534-92	17.9	Suspended
	535-92	13.6	Spalled Ball
	536-92	13.6	Suspended
	537-92	17.9	Suspended
	538-92	17.9	Suspended
3	539-92	1,511.7	Suspended
	540-92	1,511.7	Suspended
	541-92	1,511.7	Suspended
	542-92	1,511.7	Suspended
	543-92	1,511.7	Suspended
	544-92	1,511.7	Suspended
4	545-92	1,509.7	Suspended
	546-92	1,509.7	Suspended
	547-92	1,509.7	Suspended
	548-92	1,509.7	Suspended
	549-92	1,509.7	Suspended
	550-92	1,509.7	Suspended

TABLE 20

Test Lives of Hybrid Bearing with TSN-03H Balls
 MMV206K4 FS649 Hybrid Bearing
 Speed: 3,000 rpm
 Radial Load: 1,175 lbs.
 Lube: 0.09 gal./min. of Mobil DTE Extra Heavy Oil
 Ball & Inner Race Contact Stress: 515.2 ksi
 Calculated L10 = 31.5 hours

Group	Bearing #	Hours Run	Post-run Condition
1	258-93	173.2	Suspended
	259-93	173.2	Spalled Ball
	260-93	190.9	Suspended
	261-93	190.9	Suspended
	262-93	190.9	Suspended
	263-93	190.9	Suspended
2	264-93	189.2	Suspended
	265-93	189.2	Suspended
	266-93	183.2	4 Spalled Balls
	267-93	183.2	Suspended
	268-93	189.2	Suspended
	269-93	189.2	Suspended
3	270-93	71.6	Suspended
	271-93	71.6	Suspended
	272-93	71.6	Suspended
	273-93	71.6	Suspended
	274-93	50.1	Spalled Ball
	275-93	50.1	Suspended
4	276-93	142.3	Spalled Ball
	277-93	142.3	Suspended
	278-93	148.2	Suspended
	279-93	148.2	Suspended
	280-93	148.3	Suspended
	281-93	148.3	Suspended

TABLE 21

Dimensional Inspection Data of Hybrid Bearing with NBD-200 Balls
MMV206K4 FS649 Hybrid Bearings Assembled with CERBEC NBD-200 Balls

Speed: 3,000 rpm
Radial Load: 1,175 lbs.
Lube: 0.09 gal./min. of Mobil DTE Extra Heavy Oil
Ball & Inner Race Contact Stress: 515.2 ksi
Calculated L10 = 31.5 hours

Group	Bearing #	Bore (Inches)	O.D. (Inches)	Radial Play (Inches)	Ball Diameter (Inches)
1	527-92	1.1810	2.4406	0.0016	9 at 0.374961
	528-92	1.1810	2.4406	0.0009	9 at 0.374961
	529-92	1.1810	2.4406	0.0009	9 at 0.374961
	530-92	1.1810	2.4406	0.0016	9 at 0.374961
	531-92	1.1810	2.4406	0.0013	1 at 0.374961 8 at 0.374963
	532-92	1.1810	2.4407	0.0011	9 at 0.374963
2	533-92	1.1810	2.4407	0.0012	9 at 0.374963
	534-92	1.1810	2.4406	0.0012	9 at 0.374963
	535-92	1.1810	2.4407	0.0008	9 at 0.374963
	536-92	1.1810	2.4406	0.0009	9 at 0.374963
	537-92	1.1810	2.4406	0.0007	9 at 0.374963
	538-92	1.1810	2.4407	0.0007	9 at 0.374964
3	539-92	1.1810	2.4406	0.0014	9 at 0.374964
	540-92	1.1810	2.4406	0.0011	9 at 0.374964
	541-92	1.1810	2.4406	0.0009	9 at 0.374964
	542-92	1.1810	2.4406	0.0012	9 at 0.374964
	543-92	1.1810	2.4406	0.0010	4 at 0.374964 5 at 0.374967
	544-92	1.1810	2.4406	0.0011	9 at -.374967
4	545-92	1.1810	2.4406	0.0012	9 at -.374967
	546-92	1.1810	2.4406	0.0009	9 at -.374967
	547-92	1.1810	2.4406	0.0010	9 at -.374967
	548-92	1.1810	2.4406	0.0008	9 at -.374967
	549-92	1.1810	2.4406	0.0009	9 at -.374967
	550-92	1.1810	2.4407	0.0014	9 at -.374967

TABLE 22

Dimensional Inspection Data of Hybrid Bearings with TSN-03H Balls
MMV206K4 FS649 Hybrid Bearings Assembled with Toshiba TSN-03H Balls

Speed: 3,000 rpm
Radial Load: 1,175 lbs.
Lube: 0.09 gal./min. of Mobil DTE Extra Heavy Oil
Ball & Inner Race Contact Stress: 515.2 ksi
Calculated L10 = 31.5 hours

Group	Bearing #	Bore (Inches)	O.D. (Inches)	Radial Play (Inches)	Ball Diameter (Inches)
1	258-93	1.1810	2.4406	0.0011	9 at 0.375020
	259-93	1.1810	2.4406	0.0010	9 at 0.375020
	260-93	1.1810	2.4406	0.0015	9 at 0.375020
	261-93	1.1810	2.4406	0.0010	9 at 0.375020
	262-93	1.1810	2.4406	0.0008	9 at 0.375020
	263-93	1.1810	2.4407	0.0012	9 at 0.375020
2	264-93	1.1810	2.4407	0.0010	9 at 0.375020
	265-93	1.1810	2.4406	0.0015	9 at 0.375020
	266-93	1.1810	2.4406	0.0010	9 at 0.375020
	267-93	1.1810	2.4406	0.0011	9 at 0.375020
	268-93	1.1810	2.4406	0.0014	9 at 0.375020
	269-93	1.1810	2.4406	0.0010	9 at 0.375020
3	270-93	1.1810	2.4406	0.0009	9 at 0.375020
	271-93	1.1810	2.4406	0.0010	9 at 0.375020
	272-93	1.1810	2.4406	0.0015	9 at 0.375020
	273-93	1.1810	2.4406	0.0008	9 at 0.375020
	274-93	1.1810	2.4406	0.0010	9 at 0.375020
	275-93	1.1810	2.4406	0.0014	9 at 0.375020
4	276-93	1.1810	2.4406	0.0016	9 at 0.375020
	277-93	1.1810	2.4406	0.0009	9 at 0.375020
	278-93	1.1810	2.4406	0.0008	9 at 0.375020
	279-93	1.1810	2.4406	0.0010	9 at 0.375020
	280-93	1.1810	2.4406	0.0013	9 at 0.375020
	281-93	1.1810	2.4406	0.0009	9 at 0.375020

DETAILS (cont.):

Testing was done in three standard endurance machines (Figures 66 and 67), and bearings lubricated with 0.09 gallons/minute/bearing of Mobil DTE Extra Heavy oil at 110°F from the central lubrication system. Calculated Lambda is 7.09 microinches.

Bearings were tested under 1,175 lbs. radial load with a maximum ball and inner ring contact stress of 512.2 ksi (3.55 Gpa) and run at 3,000 rpm. Each type of MMV206K4 FS649A hybrid bearing, with CERBEC NBD-200 and Toshiba TSN-03H Silicon Nitride balls, consisted of four groups of six bearings per group. Each group was run until 1,500 hours or one bearing failure occurred within the group. Calculated L10 was 31.5 hours.

The test rig failure detection system consists of a Robertshaw Model 366 Vibraswitch Malfunction Detector set to shut the test rig off at vibration levels higher than normal rig operation. See attached Robertshaw specification sheet.

TEST #1712 L268

MMV206K4 FS649A
HYBRID TEST BALL BEARING

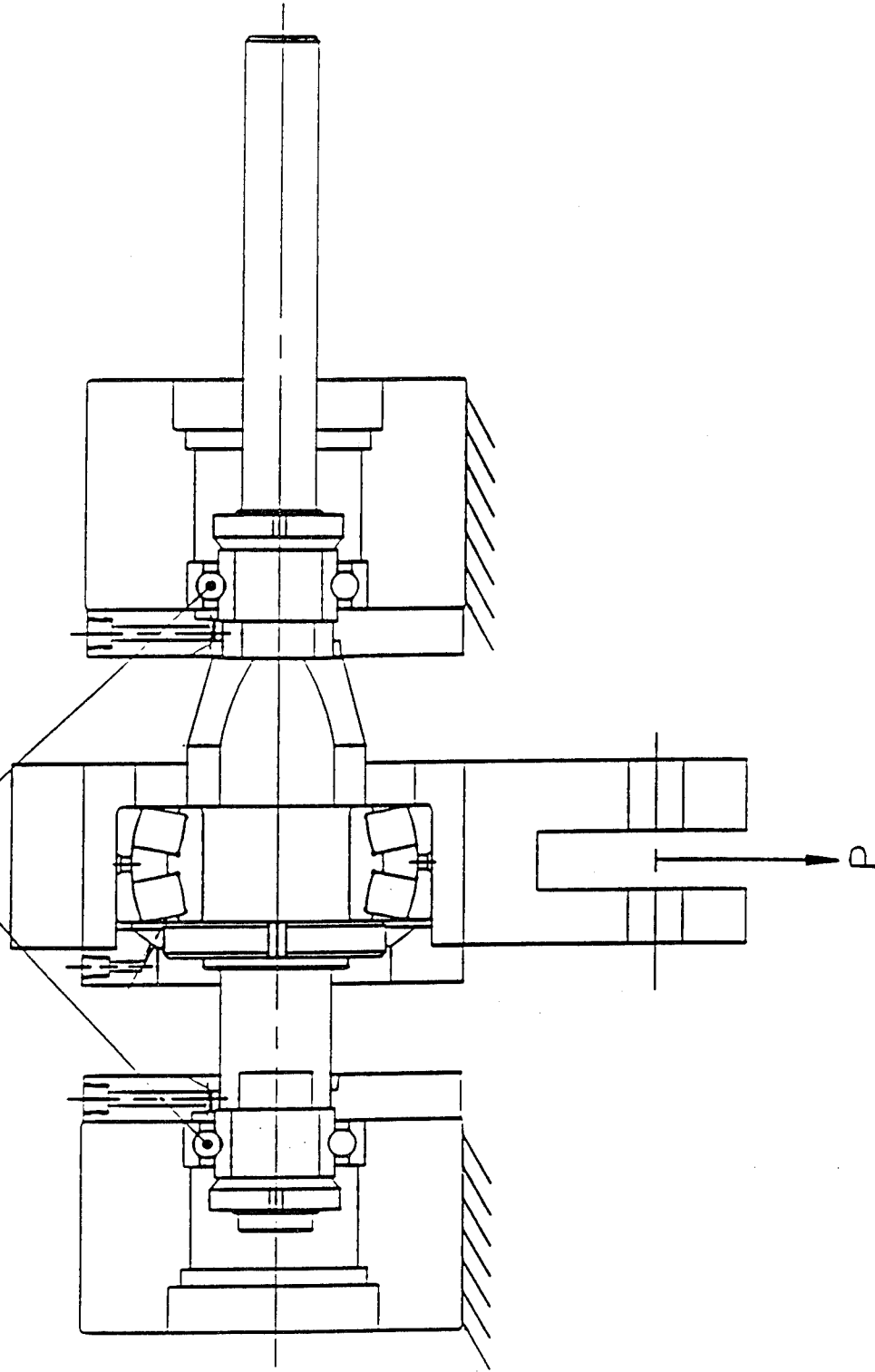
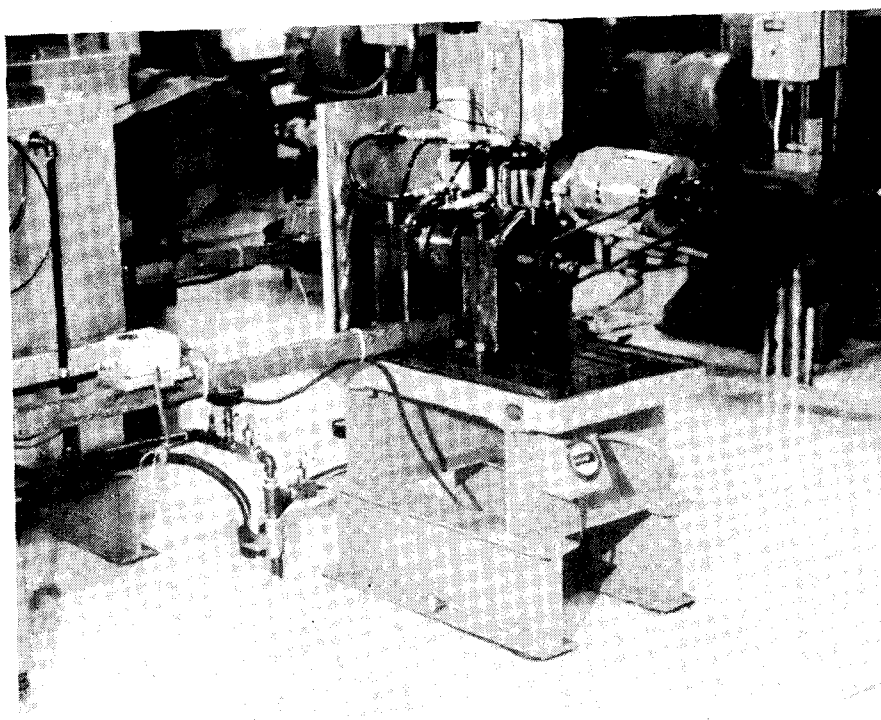
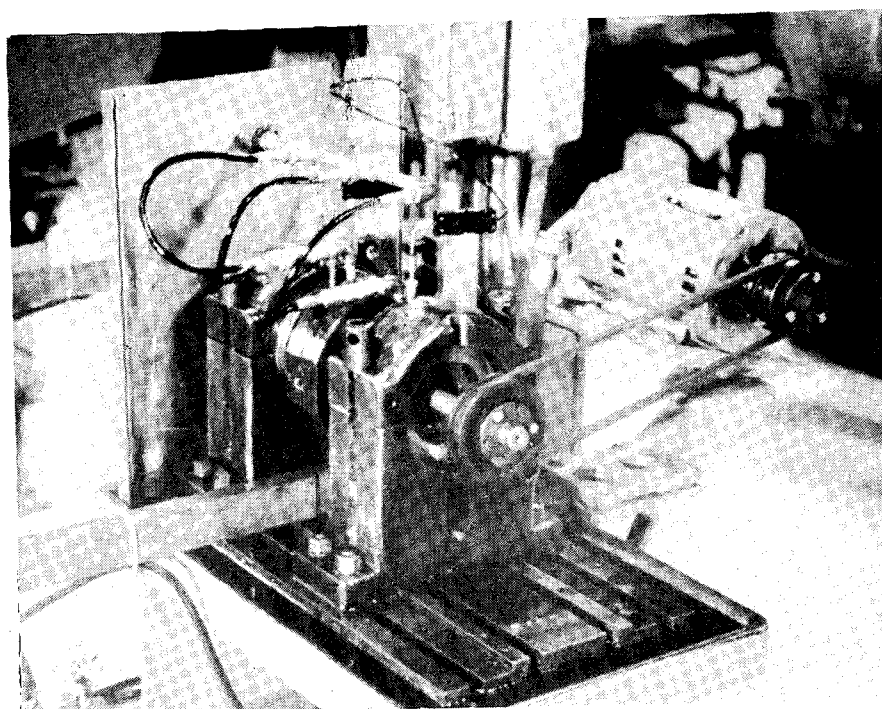


FIG.66 Hybrid Bearing Test Layout



Standard Endurance Test Machine



Standard Endurance Test Machine

FIG. 67 Photographs of Standard Endurance Test Machines

GENERAL DESCRIPTION

The Model 366 VIBRASWITCH is a vibration sensitive device that protects rotating and reciprocating machinery from extensive damage resulting from mechanical malfunction. When the vibration level of a VIBRASWITCH-protected machine exceeds normal by a preselected amount, an internal switch closes, actuating either an audible warning system or a shutdown circuit before costly damage occurs. Failing bearings, broken blades and similar malfunctions cause increased imbalance or high frequency vibration detectable with the VIBRASWITCH. It is designed for maintenance-free service in permanent installations where general purpose weather-resistant enclosures are required.

The VIBRASWITCH is an acceleration sensitive instrument that measures the total acceleratory shock present on the machine. Acceleration is a vibration characteristic of prime importance in cases of mechanical failure on reciprocating or rotating machinery. Acceleration is directly related to the shock forces (impact) acting on a machine — thus the VIBRASWITCH offers a valid measurement of the destructive forces acting on the machine.

Acceleratory measurements made by the VIBRASWITCH are the summation of all of the individual accelerations giving a total destructive force acting on the machine — the result is positive protection.

PRINCIPLE OF OPERATION

The Model 366 VIBRASWITCH employs a magnetic circuit opposed by inertial and adjustable spring forces in the actuating mechanism. Operation of the VIBRASWITCH may be understood by reference to Figure 1.

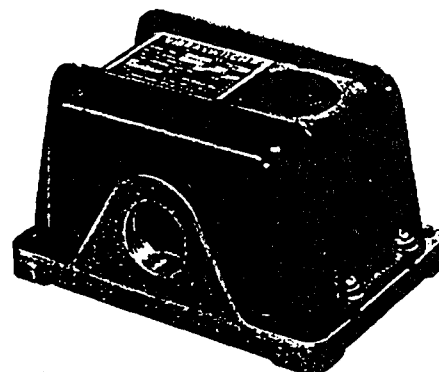
The armature is constrained so as to respond to only one direction of movement by a frictionless flexure pivot composed of two overlapping blocks and a leaf spring loaded in one direction to hold the blocks together. The armature rotates on the pivot being forced in one direction by the adjusting spring force and the other direction by the magnetic force.

When the entire assembly is subjected to vibration perpendicular to the base, the peak acceleration times the effective mass of the armature produces an inertial force, aided by the adjustable spring tending to pull the armature away from the stop pin and the restraining force of the magnet. When the peak acceleration exceeds the set-point level the armature leaves the stop pin, increasing the gap and decreasing the force with the armature continuing to move up until it reaches the latch magnet, actuating the switch during its upward travel.

The VIBRASWITCH may be reset by depressing the reset button or by applying power to the electrical reset coil. The effect of temperature in the mechanism is negligible as the elastic modulus of the adjusting spring and the magnetic flux through the air gap both decrease slightly with increasing temperature thereby compensating each other.

PRODUCT SPECIFICATION MODEL 366


VIBRASWITCH[®] MALFUNCTION DETECTOR Model 366

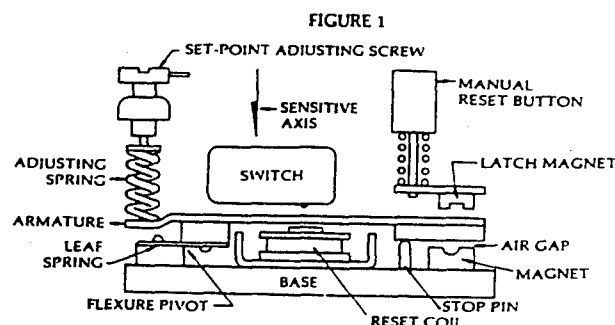


VIBRASWITCH MODEL 366



FEATURES AND BENEFITS

- Acceleration sensitive —
Measures total destructive shock, not displacement.
- No maintenance —
No moving parts except when set-point is exceeded.
- Continuous protection —
No attention required after installation.
- Long life —
Instrument is rugged and durable—no wearing parts.
- Reset —
Choice of remote electrical or manual at unit.
- Self powered —
Does not require any form of external power to operate.
-  Approved



Robertshaw Controls Company
TENNESSEE DIVISION

SPECIFICATIONS

Enclosure General purpose, meets weather resistant NEMA 4 specifications

Enclosure Materials

Cover High impact ABS thermoplastic
Base Type 360 (Cu Free) Aluminum
Set-Point Range 0-4.5g, adjustable 1g per turn
Accuracy $\pm 5\%$ of full range at frequencies up to 300 Hz

Contact Ratings

Designation "A": 5a at 120, 240 or 460 vac, non-inductive, 0.5a at 115 vdc, 2a at 48 vdc, 3a at or below 24 vdc.

Designation "D": 5 amps at 125-250 vac; 3 amps at 30 vdc.

Contact Arrangements SPDT, or DPDT

Temperature Limits Maximum +200°F;
Minimum -40°F

Reset Coil 120 VAC or DC

Weight:

Net 2 lbs.

Shipping 2.5 lbs.

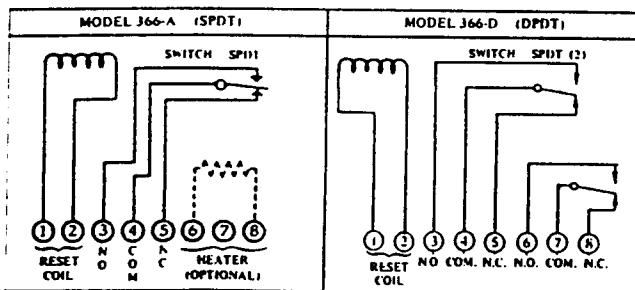
Accessory Equipment (optional)

Model 563A Vibration Monitor is available with "starting time delays" and "monitoring time delays" to prevent false shutdown or alarm conditions.

Related Product

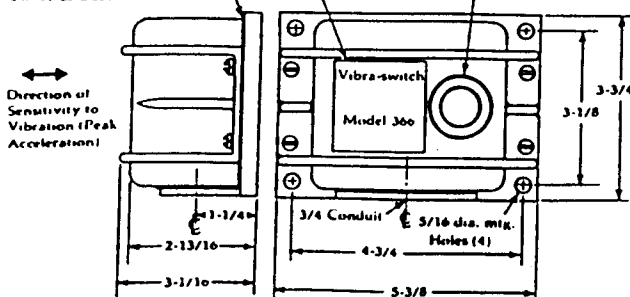
Vibraswitches with built-in start and monitoring delays are available. See PS 375A/376A.

CUSTOMER CONNECTIONS



DIMENSION DATA

Thermoplastic Rubber Gasket Provides a Tight Seal Between Cover & Base



ORDERING INFORMATION AND MODEL NUMBERS

*STANDARD MODEL 366 - A8 ^W271.3 12/88
366 - D8 ^W316.2

KEY MODEL NUMBER

Designation	Description
* 366	VIBRASWITCH® SA Approved ENCLOSURE 4 and 5 Equivalent: NEMA - 4 & NEMA - 12 Range 0-4.5G

TABLE 1 - SWITCH CONTACTS

Designation	Description
* A	SPDT Single pole, double throw load contacts.
D	DPDT (2 gang mounted SPDT load switches)

TABLE 2 - REMOTE RESET

Designation	Description
2	24 volt dc reset coil voltage.
4	48 volt dc reset coil voltage.
*8	120 volt ac or dc coil voltage

Note: Other reset coil voltages available on special order. Consult factory.

ACCESSORY ITEMS (MODELS 365 & 366)

Part Number	Description
	* See Notes Below
260-GG-453	Space heater for maintaining internal of unit moisture free — 120 volt models.
260-GG-359	Same — 48 vdc models.
260-GG-220	Same — 24 vdc models.

Note: #1 Use option "D" when required with Vibration Monitors
Note: #2 Addition of Space Heater to "D" option Consult Factory.

Robertshaw
CONTROLS COMPANY

U.S.A.

Robertshaw Controls Company
Tennessee Division
2318 Kingston Pike, S.W.
P.O. Box 400
Knoxville, Tennessee 37901-0400
TWX: 810-583-0143 Telephone: (615) 546-0550

Exports

Robertshaw International Sales Company
1701 Byrd Avenue
Richmond, Virginia 23230-3011
Telephone: (804) 281-0700

Canada:

Robertshaw Controls Canada, Inc.
5785 Kennedy Road
Mississauga, Ontario, Canada L4Z 2G3
Telephone: (416) 625-0805

O-3770 (10/87) Printed in U.S.A.

Appendix E

The Equivalent Bearing Cycles and Bearing Revolution for the Non-track Forming Case

In the case when the ball rotational axis is not stationary with respect to the bearing axis, no track will be formed on the ball. In this non-track forming case, the orientation of the ball rotational axis shifts gradually with time, such that all the surface elements of the ball will be rolled over. It can be assumed that, for a long period of time, each of the surface elements on the ball will be subject to an equal number of contact cycles of the outer ring and inner ring contacts.

Based on the above assumption, the number of ball cycles required to generate one contact pass on the surface element on the ball may be approximated as the ratio of ball surface area (A_p) and the area of the rolling track on the ball (A_t).

Thus for non-track forming balls, the number of bearing revolutions to generate a contact pass on the ball surface element is called the equivalent bearing cycles (denoted by N_e), which is given by

$$N_e = \Omega_o / \Omega_b (A_p / A_t) = 2\gamma / (1 - \gamma^2) \times A_p / A_t$$

where $A_p = \pi D^2$, the area of the ball surface and

$$A_t = 2 \pi a_{\max} D$$

where a_{\max} is the semi-major axis of the inner or outer ring contact ellipses.

Note that for a track-forming ball, the number of bearing revolutions to generate a contact pass on the track is given by Ω_o / Ω_b .

The ratio of the equivalent bearing cycles in a non-track-forming ball to the bearing revolution for a track-forming ball is

$$A_p / A_t = \frac{1}{2} D / a_{\max} .$$

For the pure thrust loaded Cerbec test bearing, the semi-major axes at the inner and outer ring contacts have been calculated (see Table 18). From Section 6.3.1, we have $\Omega_o / \Omega_b = 0.1675$.

The equivalent bearing cycles N_e are calculated below for the inner and outer ring contacts:

	a_{\max}	A_p/A_t	N_e
Inner ring contact	2.11mm	2.63	0.440
Outer ring contact	1.84mm	3.02	0.506